

Development of a wireless MEMS inertial system for health monitoring of structures

A Thesis
submitted to the faculty of the

Worcester Polytechnic Institute

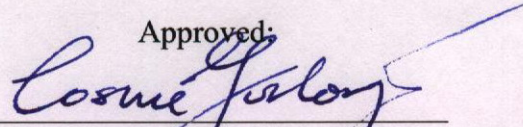
as a partial fulfillment of the requirements for the
Degree of Master of Science
in
Mechanical Engineering

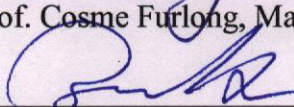
by

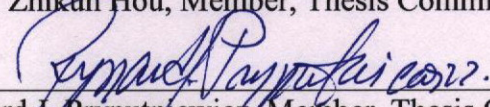
Wing-Hang (Ronald) Kok

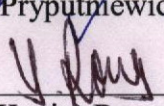
22 November 2004

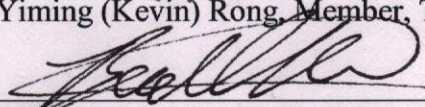
Approved:

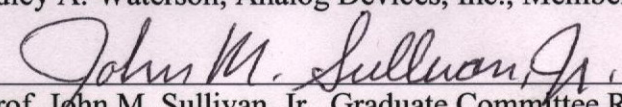

Prof. Cosme Furlong, Major Advisor


Prof. Zhikun Hou, Member, Thesis Committee


Prof. Ryszard J. Pryputniewicz, Member, Thesis Committee


Prof. Yiming (Kevin) Rong, Member, Thesis Committee


Mr. Bradley A. Waterson, Analog Devices, Inc., Member, Thesis Committee


Prof. John M. Sullivan, Jr., Graduate Committee Representative

Copyright © 2004

by

NEST – NanoEngineering, Science, and Technology
CHSLT – Center for Holographic Studies and Laser micro-mechaTronics
Mechanical Engineering Department
Worcester Polytechnic Institute
Worcester, MA 01609-2280

All rights reserved

SUMMARY

Health monitoring of structures by experimental modal analysis is typically performed with piezoelectric based transducers. These transducers are usually heavy, large in size, and require high power to operate, all of which reduce their versatility and applicability to small components and structures.

The advanced developments of microfabrication and microelectromechanical systems (MEMS) have lead to progressive designs of small footprint, low dynamic mass and actuation power, and high-resolution inertial sensors. Because of their small dimensions and masses, MEMS inertial sensors could potentially replace the piezoelectric transducers for experimental modal analysis of small components and structures.

To transfer data from MEMS inertial sensors to signal analyzers, traditional wiring methods may be utilized. Such methods provide reliable data transfer and are simple to integrate. However, in order to study complex structures, multiple inertial sensors, attached to different locations on a structure, are required. In such cases, using wires increases complexity and eliminates possibility of achieving long distance monitoring. Therefore, there is a need to implement wireless communications capabilities to MEMS sensors.

In this thesis, two different wireless communication systems have been developed to achieve wireless health monitoring of structures using MEMS inertial sensors. One of the systems is designed to transmit analog signals, while the other transmits digital signals.

The analog wireless system is characterized by a linear frequency response function in the range of 400 Hz to 16 kHz, which covers the frequency bandwidth of the MEMS inertial sensors. This system is used to perform modal analysis of a test structure by applying multiple sensors to the structure. To verify the results obtained with MEMS inertial sensors, noninvasive, laser optoelectronic holography (OEH) methodology is utilized to determine modal characteristics of the structure. The structure is also modeled with analytical and computational methods for correlation of and verification with the experimental measurements. Results indicate that attachment of MEMS inertial sensors, in spite of their small mass, has measurable effects on the modal characteristics of the structure being considered, verifying their applicability in health monitoring of structures.

The digital wireless system is used to perform high resolution tilt and rotation measurements of an object subjected to angular and linear accelerations. Since the system has been developed based on a microcontroller, programs have been developed to interface the output signals of the sensors to the microcontroller and RF components. The system is calibrated using the actual driving electronics of the MEMS sensors, and it has achieved an angular resolution of 1.8 mrad. The results show viability of the wireless MEMS inertial sensors in applications requiring accurate tilt and rotation measurements.

Additional results presented included application of a MEMS gyroscope and microcontroller to perform angular rate measurements. Since the MEMS gyroscope only generates analog output signals, an analog to digital conversion circuit was developed. Also, a program has been developed to perform analog to digital conversion with two decimal places of accuracy. The experimental results demonstrate feasibility of using the

microcontroller and the gyroscope to perform wireless angular rate measurements.

ACKNOWLEDGEMENTS

First of all, I would like to express my appreciation to my advisor, Prof. Furlong, and to Prof. Pryputniewicz, who offered me the opportunity to study and research in this exciting MEMS area. Also, I would like to thank for their substantial assistance, guidance, and support in the completion of this Thesis research and studies at WPI. In addition, I gratefully acknowledge the support by the NanoEngineering, Science, and Technology (NEST) Program at Worcester Polytechnic Institute, Mechanical Engineering Department, Center for Holographic Studies and Laser micro-mechanics Laboratory (CHSLT), for this Thesis research.

I wish to thank my colleagues at the WPI-ME/CHSLT for their help and friendship. I have really enjoyed the time working with them, and I have learned a lot from them also. I especially want to thank Mr. Peter Hefti, who gave me a lot of advices, ideas, and help in my work.

I particularly acknowledge my parents and my sister, for their endless encouragement, care, and support during the past 25 years. I special thank my fiancée, Jacqueline Tin, who supported and took care of me in the past couple of years.

TABLE OF CONTENTS

Copyright	2
Summary	3
Acknowledgements	6
Table of contents	7
List of figures	9
List of tables	15
Nomenclature	16
Objective	20
1. Introduction	21
1.1 Design considerations	23
2. Microelectromechanical system	26
2.1 Fabrication of MEMS	28
2.1.1 Bulk micromachining	28
2.1.2 Surface micromachining	29
2.1.3 LIGA process	31
2.2 MEMS inertial sensors	32
2.2.1 Piezoresistive inertial sensors	33
2.2.2 Piezoelectric inertial sensors	34
2.2.3 Capacitive inertial sensors	36
2.2.4 Resonant inertial sensors	39
2.3 System control methodologies	40
2.4 MEMS accelerometers	41
2.4.1 Analog Devices ADXL202 accelerometer	41
2.5 MEMS gyroscopes	49
2.5.1 Analog Devices ADXRS150 gyroscope	51
3. Characterization of MEMS accelerometer	56
3.1 Analytical considerations	57
3.2 Computation considerations	60
3.3 Experimental considerations	66
3.3.1 Experimental setup	66
3.3.1.1 Laser vibrometer	67
3.3.1.2 Low pass filter circuit	68

3.3.2 Experimental results	69
3.3.2.1 Determination of frequency response	69
4. Development of a wireless data acquisition system	73
4.1 Analog wireless data acquisition system	73
4.1.1 National Instruments data acquisition system	75
4.1.2 Experimental characterization of the analog wireless data acquisition system	78
4.2 Digital wireless data acquisition system	81
4.2.1 Connection of the microcontroller	83
4.2.2 Software interface	86
4.2.3 Construction of the program	87
5. Applications	89
5.1 Modal analysis of a cantilever	89
5.1.1 Analytical considerations	91
5.1.2 Computational considerations	105
5.1.3 Experimental characterization of the cantilever	107
5.2 Tilt and rotation measurements	112
5.2.1 Programming of the microcontroller	113
5.2.2 Graphical display of measurements	118
5.2.3 Calibration of the ADXL202 accelerometer with the microcontroller system	120
5.3 Angular rate measurements with MEMS gyroscopes	129
5.3.1 Analog to digital conversion	130
5.3.2 Programming of the microcontroller	131
5.3.3 Preliminary angular rate measurements	132
6. Conclusion and future works	135
7. References	139
Appendix A. Front panel of the developed LabVIEW VI for a four channels spectrum analyzer	146
Appendix B. Block diagram of the developed LabVIEW VI for a four channels spectrum analyzer	147
Appendix C. Source codes of the microcontroller with a wireless transmitter	148
Appendix D. Source codes of the microcontroller with a wireless microcontroller	151
Appendix E. Source code of the analog-to-digital conversion circuit	152

LIST OF FIGURES

Fig. 2.1.	Current and prospective applications of MEMS sensors in automobiles.	27
Fig. 2.2.	Bulk micromachining processes to fabricate a membrane.	29
Fig. 2.3.	Fabrication process of a surface micromachined component.	30
Fig. 2.4.	Fabrication process of a LIGA component.	31
Fig. 2.5.	Circuit diagram of a Wheatstone bridge.	33
Fig. 2.6.	Schematic of a piezoresistive inertial sensor: (a) top view showing configuration of piezoresistors and, (b) cross sectional view showing the proof mass and the spring mechanism.	34
Fig. 2.7.	Schematic depicting the piezoelectric effect: (a) electrical potential induced by the deformation of a piezoelectric material and, (b) deformation induced by application of an electrical potential.	35
Fig. 2.8.	Two configurations of piezoelectric inertial sensors: (a) cantilever and, (b) sandwich.	36
Fig. 2.9.	Parallel plates capacitor.	36
Fig. 2.10.	Schematic of a single axis capacitive MEMS inertial sensor.	37
Fig. 2.11.	Typical configuration of a MEMS resonator.	40
Fig. 2.12.	Different electronic packages of the dual-axes ADXL202 MEMS accelerometer fabricated by Analog Devices.	42
Fig. 2.13.	Die of the Analog Devices ADXL202 accelerometer. The microelectromechanical sensor, surrounded by CMOS electronics, is located at the center of the die.	43
Fig. 2.14.	Details of the microelectromechanical sensor of the ADXL202 accelerometer.	44
Fig. 2.15.	Schematic showing the principle of operation of a dual-axes accelerometer.	45

Fig. 2.16.	One set of folded springs of the ADXL202 accelerometer: (a) SEM micrograph showing details of the springs and, (b) schematic showing the corresponding degrees of freedom of each individual spring.	45
Fig. 2.17.	Stopper mechanism of the ADXL202 accelerometer. Stopper is attached to the folded springs and the proof mass.	46
Fig. 2.18.	SEM micrograph showing 3D view of one set of folded springs.	47
Fig. 2.19.	One set of capacitive combs: (a) SEM micrograph and, (b) schematic showing the fixed and the moving capacitive electrodes. The capacitive combs, as shown in (a), are sensitive to horizontal motions.	48
Fig. 2.20.	SEM micrograph showing 3D view of one set of electrostatic combs.	48
Fig. 2.21.	Illustration of the Coriolis effect.	49
Fig. 2.22.	Schematic showing general configuration of a MEMS gyroscope.	50
Fig. 2.23.	Different electronic packages of the ADXRS150EB MEMS gyroscope fabricated by Analog Devices.	52
Fig. 2.24.	Die of the Analog Devices ADXRS150 gyroscope. The microelectromechanical sensor, surrounded by CMOS electronics, is located at the center of the die.	53
Fig. 2.25.	Details of the microelectromechanical sensor of the ADXRS150 gyroscope.	53
Fig. 2.26.	Schematic showing the principle of operation of a MEMS gyroscope.	54
Fig. 2.27.	Micrograph showing the spring element and the velocity sensing finger of the microelectromechanical sensor of the ADXRS150 MEMS gyroscope.	54
Fig. 2.28.	SEM micrograph showing details of a set of electrostatic combs of the ADXRS150 gyroscope.	55
Fig. 2.29.	SEM micrograph showing 3D view of a set of the electrostatic combs of the ADXRS150 gyroscope.	55
Fig. 3.1.	Configuration of a single axis accelerometer.	56

Fig. 3.2.	Measuring deviations, I/I , as a function of frequency ratio for specific damping ratios.	60
Fig. 3.3.	Axisymmetric FEM model of the proof mass, folded springs, and moving combs of an ADXL202 accelerometer.	61
Fig. 3.4.	First mode of vibration calculated at 8.48 kHz.	62
Fig. 3.5.	Second mode of vibration calculated at 77.10 kHz.	62
Fig. 3.6.	Third mode of vibration calculated at 77.42 kHz.	62
Fig. 3.7.	Fourth mode of vibration calculated at 90.68 kHz.	63
Fig. 3.8.	Fifth mode of vibration calculated at 90.68 kHz.	63
Fig. 3.9.	FEM determined fundamental natural frequency versus thickness of the proof mass, E is 160 GPa and ρ is 2.33 g/cm ³ .	65
Fig. 3.10.	FEM determined fundamental natural frequency versus modulus of elasticity, E , of the proof mass, thickness is 3 μ m and ρ is 2.33 g/cm ³ .	65
Fig. 3.11.	Schematic diagram of the experimental setup used to characterize the frequency responses of MEMS accelerometers.	67
Fig. 3.12.	Block diagram of the low-pass filter circuit used to interface the ADXL202 accelerometer.	69
Fig. 3.13.	Power spectra measured with both, a MEMS accelerometer and a laser vibrometer. The power spectra correspond to the response of a harmonic motion characterized by the frequency of 2 kHz at 13.2 mg.	70
Fig. 3.14.	Ratio of the power spectra of the MEMS accelerometer and the laser vibrometer, based on the results in Fig. 3.13.	71
Fig. 3.15.	Power spectra measured with both, a MEMS accelerometer and a laser vibrometer. The power spectra correspond to the response of a random excitation containing frequencies in the [0 - 12.8] kHz range and accelerations in the [0 - 0.135] g range.	72
Fig. 4.1.	RF transmitter, receiver, and evaluation board used in the development of the analog wireless MEMS inertial system.	75

Fig. 4.2.	NI SCXI-1530 accelerometer amplifier module, assembled to the SCXI-1000 chassis, used in the development and characterization of the analog wireless MEMS inertial system.	76
Fig. 4.3.	Snapshot of the developed LabVIEW VI for a four channels spectrum analyzer.	77
Fig. 4.4.	Snapshot of the block diagram of the LabVIEW VI shown in Fig. 4.3.	78
Fig. 4.5.	Schematic diagram of the experimental setup used to characterize the analog wireless system.	79
Fig. 4.6.	Frequency response function of the analog wireless data acquisition system.	80
Fig. 4.7.	Coherence function of the analog wireless data acquisition system.	80
Fig. 4.8.	Microcontroller evaluation board utilized in the developments. The surface mount microcontroller package is located at the center of the board.	81
Fig. 4.9.	RF modules utilized: (a) transmitter (b) receiver.	82
Fig. 4.10.	Schematic showing connection of the microcontroller board to a computer.	83
Fig. 4.11.	Block diagram showing connections of the transmitter unit.	84
Fig. 4.12.	Block diagram showing connections of the receiver unit.	85
Fig. 4.13.	Transmitter unit consists of the microcontroller board, MEMS accelerometer, and the wireless RF module.	85
Fig. 4.14.	Receiver unit consist of the microcontroller board and the wireless RF module.	85
Fig. 4.15.	Interface of the BASIC Stamp Window Editor used to program the microcontroller.	86
Fig. 5.1.	Experimental setup used to perform modal analysis of a cantilever.	91
Fig. 5.2.	Beam subjected to a distributed load: (a) simply supported beam with distributed load $p(x,t)$ and, (b) free body diagram of a beam element.	92

Fig. 5.3.	First three bending modes of vibration of the test cantilever.	97
Fig. 5.4.	Cantilever with a mass, m_{mass} , attached at its free end and the corresponding deflection curve of the cantilever.	98
Fig. 5.5.	Cantilever with multiple masses, m_1 to m_n , attached to arbitrary locations along the cantilever, and the corresponding deflection curve the cantilever.	100
Fig. 5.6.	Fundamental natural frequency of the cantilever versus the location of one accelerometer attached along the longitudinal axis locations of the cantilever.	104
Fig. 5.7.	CAD model of the cantilever.	105
Fig. 5.8.	1st mode of vibration at 264.65 Hz. The cantilever deforms along the z axis.	106
Fig. 5.9.	2nd mode of vibration at 1008.4 Hz. The cantilever deforms along the y axis.	106
Fig. 5.10.	3rd mode of vibration at 1636.9 Hz. The cantilever deforms along the z axis.	106
Fig. 5.11.	4th mode of vibration at 2075.8 Hz. The cantilever twists about the x axis.	106
Fig. 5.12.	5th mode of vibration at 4515.0 Hz. The cantilever deforms along the z axis.	106
Fig. 5.13.	Optoelectronic holography (OEH) system used to perform modal analysis of the cantilever with attached MEMS accelerometers.	108
Fig. 5.14.	1st bending mode of the cantilever: (a) without MEMS accelerometer attached and, (b) with MEMS accelerometer.	110
Fig. 5.15.	2nd bending mode of the cantilever: (a) without MEMS accelerometer attached and, (b) with MEMS accelerometer.	110
Fig. 5.16.	Mode shapes of vibration of the cantilever measured using the analog wireless MEMS inertial system.	112

Fig. 5.17.	Digital output signal of a MEMS accelerator.	114
Fig. 5.18.	Debug terminal showing dual-axes acceleration measurements.	116
Fig. 5.19.	Flow diagram of the program developed to interface digital output signals of the MEMS accelerometer with the wireless microcontroller system: (a) transmitter unit, and (b) the receiver unit.	118
Fig. 5.20.	Interface of the StampPlot Pro program used to display graphical information from the developed digital wireless system.	120
Fig. 5.21.	Schematic diagram showing the coordinate system used in the calibration process of the MEMS accelerometer.	121
Fig. 5.22.	Experimental setup showing the wireless transmitter unit and the high-resolution rotational stage.	122
Fig. 5.23.	Uncalibrated dual-axes acceleration measurements as a function of a full 360° rotation.	123
Fig. 5.24.	Calibrated rotation measurements using the developed digital wireless data acquisition system and the dual-axes MEMS inertial sensor.	127
Fig. 5.25.	Polar representation of dual-axes acceleration measured with the developed wireless data acquisition system. $A(x)$ is acceleration along the x -axis, and $A(y)$ is acceleration along the y -axis.	128
Fig. 5.26.	Connection diagram of the MEMS gyroscope and the A/D converter to the microcontroller board. P0 to P2 are the corresponding I/O pins on the microcontroller board.	130
Fig. 5.27.	Flow diagram of the program developed to interface the microcontroller with an ADXRS150 MEMS gyroscope.	132
Fig. 5.28.	Experimental configuration utilized to perform angular rate measurements using the ADXRS150 MEMS gyroscope.	133
Fig. 5.29.	Preliminary angular rate measurements using the an ADXRS150 MEMS gyroscope and the microcontroller.	133

LIST OF TABLES

Table 2.1.	Pertinent characteristics of the MEMS accelerometers utilized in the developments.	42
Table 2.2.	Pertinent characteristics of the MEMS gyroscopes utilized in the developments.	51
Table 3.1.	FEM calculated modes of vibrations of the proof mass: E is 160GPa, ρ is 2.33 gr/cm ³ , and thickness is 3 μ m	63
Table 4.1.	Pertinent characteristics of the analog wireless data acquisition system used in the developments.	74
Table 4.2.	Pertinent characteristics of the microcontroller utilized in the developments.	82
Table 4.3.	Pertinent characteristics of the RF components in the developments.	82
Table 5.1.	The first three roots of Eq. 5.20 and the corresponding constants, σ_n , that define the mode shapes of a cantilever for its first three bending modes of vibration.	97
Table 5.2.	FEM calculated modes of vibrations of the cantilever.	107
Table 5.3.	Experimental determination of natural frequencies of the test cantilever using OEH methodologies.	110
Table 5.4.	Natural frequencies of the cantilever determined using analytical, computational, and experimental techniques.	111

NOMENCLATURE

a_{cor}	Coriolis acceleration
a_{acc}	acceleration applied to a single axis capacitive MEMS accelerometer
$brad$	binary radian
c	damping coefficient of a single axis accelerometer
d	gap between two capacitive plates
d_1	gap between the fixed and the moving finger-electrodes of a capacitive MEMS accelerometer, by d_{PM} increases
d_2	gap between the fixed and the moving finger-electrodes of a capacitive MEMS accelerometer, by d_{PM} decreases
dx	length of the segment of a simply support beam subjected to a distributed load
d_{PM}	displacement of the proof mass of a capacitive MEMS accelerometer due to an external acceleration
f_B	frequency shift introduced by a Bragg cell modulator
f_D	Doppler frequency shift
$f(t)$	function of time for solving the partial differential equation of a cantilever in bending
i	number of masses attached to a cantilever system
k	spring constant of a single axis accelerometer
k_s	spring constant of a single axis capacitive MEMS accelerometer
m	mass of the proof mass of an accelerometer
m_b	mass of a cantilever
m_{cor}	mass that experiences Coriolis force
m_{mass}	mass of the added mass on a cantilever, for single mass system
m_1	mass of the added mass on a cantilever, for multiple masses system
m_2	mass of the added mass on a cantilever, for multiple masses system
m_3	mass of the added mass on a cantilever, for multiple masses system
m_{PM}	mass of the proof mass of a capacitive MEMS accelerometer
\bar{m}_b	mass per unit length of a cantilever
n	number of a mode of vibration
p	number of tilt and rotation measurements
$p(x,t)$	distributed load along the cantilever
s	number of tilt and rotation measurements
t	time function of a cantilever in bending
t_{LV}	time function of the laser vibrometer
t_1	digital output signal of the ADXL202 accelerometer due to changes in the input gravitational forces
t_2	period of the carrier frequency of the digital output signal of the ADXL202 accelerometer
$u(x)$	shape function of a cantilever with a mass attached at its free end
v_m	radial velocity of a mass moving from the center to the edge on a rotating platform
v_{MR}	velocity of the reference mirror

x	displacement of a proof mass of an accelerometer, horizontal location along a cantilever
x_m	displacement of the proof mass of a typical accelerometer
x_{load}	location of the distributed load on the cantilever
x_{PM}	displacement of the proof mass of a single axis capacitive MEMS accelerometer
y	displacement of a reference frame, displacement of an object subject to harmonic motions, vertical displacement of a cantilever
y_m	displacement of the reference frame of a typical accelerometer
y_{max}	maximum deformation of a cantilever with multiple masses attached along its longitudinal axis
y_{mi}	deformation of a cantilever at the location of the applied mass, for multiple masses system
z_m	displacement of the proof mass with respect to the reference frame of a typical accelerometer
\dot{x}_m	velocity of the proof mass of a single axis accelerometer
\dot{y}_m	velocity of the reference frame of a single axis accelerometer
\dot{z}_m	velocity of the proof mass with respect to the reference frame of a single axis accelerometer
\ddot{x}_m	acceleration of the proof mass of a single axis accelerometer
\ddot{y}_m	acceleration of the reference frame of a single axis accelerometer
\ddot{z}_m	acceleration of the proof mass with respect to the reference frame of a single axis accelerometer
A	overlapping area between the fixed and the moving finger-electrodes of a capacitive MEMS accelerometer
A_p	overlapping area between two capacitive plates
$A(g)$	gravitational acceleration measured by the ADXL202 accelerometer
B_1	constant of integration obtained in the solution of the partial differential equation of a cantilever in bending
B_2	constant of integration obtained in the solution of partial differential equation of a cantilever in bending
B_3	constant of integration obtained in the solution of partial differential equation of a cantilever in bending
B_4	constant of integration obtained in the solution of partial differential equation of a cantilever in bending
C	capacitance within the electronic comb of a capacitive MEMS accelerometer
C_1	capacitance within the electronic comb of a capacitive MEMS accelerometer
C_2	capacitance within the electronic comb of a capacitive MEMS accelerometer
E	modulus of elasticity of the proof mass of a MEMS accelerometer
E_b	modulus of elasticity of a cantilever
F_{cor}	Coriolis force
F_{mass}	concentrated force caused by a mass attached to a cantilever

F_s	force of spring element of a capacitive MEMS accelerometer
H	amplitude of the proof mass with respect to the reference frame of a typical accelerometer in vibration
I_b	area moment of inertia of a cantilever
I_o	magnitude of the detected intensity of a laser vibrometer system
$I(t)$	detected intensity of a laser vibrometer system
J_1	constant for solving the calibration matrix of the ADXL202 accelerometer interfaced with the microcontroller
J_2	constant for solving the calibration matrix of the ADXL202 accelerometer interfaced with the microcontroller
J_3	constant for solving the calibration matrix of the ADXL202 accelerometer interfaced with the microcontroller
J_4	constant for solving the calibration matrix of the ADXL202 accelerometer interfaced with the microcontroller
J_5	constant for solving the calibration matrix of the ADXL202 accelerometer interfaced with the microcontroller
L_b	length of a test cantilever beam
$L(t)$	displacement of the reference mirror for a laser vibrometer system
MEMS	microelectromechanical systems
M_b	bending moment of a cantilever
M_1	matrix contains rotation angles of the tilt and rotation measurements
M_2	matrix contains ratio of duty cycles of the ADXL202 accelerometer during the tilt and rotation measurements
M_3	matrix containing the unknowns, η_2 and η_3 , of the tilt and rotation measurements
R	radius of curvature of a beam in bending
R_{in}	input angular rate to a MEMS gyroscope
R_1	resistor for the Wheatstone bridge
R_2	resistor for the Wheatstone bridge
R_3	resistor for the Wheatstone bridge
R_4	resistor for the Wheatstone bridge
T_{max}	maximum kinetic energy of a cantilever system with a mass attached to its free end
T_{beam}	kinetic energy of the distributed mass of the cantilever
T_{mass}	kinetic energy induced by a mass attached to the free end of the cantilever
VM	laser vibrometer
V_b	shear force of a cantilever beam in bending
V_{in}	input voltage of the Wheatstone bridge
V_{max}	maximum potential energy of a cantilever system with a mass attached to its free end
V_o	output voltage of the Wheatstone bridge
V_{out}	output voltage of a MEMS gyroscope
α	phase of the harmonic motions, for a cantilever with a mass attached at its free end

β	amplitude of the harmonic motion exerted to the reference frame of a typical accelerometer
$\delta(\sin\theta)$	uncertainty in rotation measurements
δt_1	uncertainty in input gravitational forces of the ADXL202 accelerometer during tilt and rotation measurements
δt_2	uncertainty in period of the carrier frequency of the ADXL202 accelerometer
ε	electrical permittivity
ε_o	permittivity of free space
ε_r	relative permittivity of the dielectric media between two capacitive plates
ϕ	phase of the harmonic motions of a typical accelerometer in vibration
γ	amplitude of harmonic motion exerted to a cantilever
κ	constant for solving the partial different equation of a cantilever in bending
λ	optical wavelength
η_1	ratio of the duty cycle of the ADXL202 accelerometer
η_2	reciprocal sensitivity of the ADXL202 accelerometer
η_3	defined constant equals to $\eta_1 \cdot \eta_2$
θ	rotation angle of the tilt and rotation measurements
σ_n	variable defined for solving the shape function of a cantilever for a specific mode, n , of vibration
ω	frequency of the motion of the reference frame of a typical accelerometer
ω_1	lower half-peak power bandwidth
ω_2	upper half-peak power bandwidth
ω_b	frequency of the harmonic motion of a cantilever
ω_n	natural frequency of the motion of the reference frame of a typical accelerometer
ω_{n_beam}	natural frequency of a cantilever
ω_r	reference frequency that is 3dB of the peak frequency
ζ	damping ratio
ΔC	capacitance difference
$\Delta\theta(t)$	optical phase difference of an OEH system
Γ	deviation function of a typical accelerometer
A	amplitude of deformation of the shape function for a cantilever with multiple masses attached
ΣT_{mass}	sum of the kinetic energy of individual masses attached to a cantilever
Ω	angular rate of a rotating platform
$\Psi(t)$	function of position for solving the partial differential equation of a cantilever in bending
$\dot{\Psi}(t)$	slope of a cantilever in bending
$\ddot{\Psi}(t)$	bending moment of a cantilever in bending
$\dddot{\Psi}(t)$	shear force of a cantilever in bending

OBJECTIVE

The objective of this thesis is to develop a miniaturized, highly accurate, wireless MEMS inertial system to perform health monitoring of structures, using commercially available MEMS inertial sensors and RF components, and to test it for different cases studies, including static and dynamic loadings.

1. INTRODUCTION

Health monitoring is the process of studying and assessing the integrity of structures, which is crucial for preventing failure and for achieving reliable designs. Health monitoring can be done by dynamic or static analysis, or a combination of both. For dynamic analysis, dynamic characteristics of the structures, including natural frequencies, modal shapes, and damping factors, are determined via modal analysis. In static analysis, deformations or changes in the orientation of structures, due to application of loads, or unexpected damages, are determined via comparisons with reference models (Van der Auweraer, 2001; Avitabile, 2001; Rao, 1995; Schwarz and Richardson, 1999).

In either static or dynamic health monitoring, the utilization of appropriate transducers is required to provide accurate measurement of structural responses in both frequency and time domains. Conventional devices utilized for health monitoring are based on piezoelectric transducers. These transducers are usually large in size, require high actuation power, and have narrow frequency bandwidths, which reduce their accuracy, versatility, and applicability to smaller structures.

The advanced developments of IC microfabrication and microelectromechanical systems (MEMS) have led to the progressive designs of small footprint, low dynamic mass and actuation power MEMS inertial sensors. Due to their high natural frequencies, these MEMS inertial sensors provide wide frequency bandwidths and high measuring accuracies. With such advantages, MEMS inertial sensors can potentially replace conventional piezoelectric transducers.

To transfer data from MEMS inertial sensors to signal analyzers, traditional wiring methods can be utilized. Such methods provide reliable data transfer and are simple to integrate. However, in order to study complex structures, multiple inertial sensors, attached to different locations on a structure, may be required. In such cases, using wires can increase the complexity of a measuring systems as well as its cost. Also, it can eliminate the possibility of achieving long distance monitoring. In addition, the measuring accuracy might decrease due to the electro-magnetic interferences along wires. Therefore, there is a need to implement wireless communications capabilities to MEMS sensors (Chung et al., 2003; Lynch, 2004; Lynch et al., 2000).

With the rapid developments of microelectronic and wireless technologies, designers and researchers now have the capabilities to develop and implement wireless health monitoring systems. However, most of the recent research efforts have been concentrated on the development of wireless systems for health monitoring of civil engineering structures, such as building and bridges (Chung et al., 2003; Kottapalli et al., 2003; Lynch, 2004; Lynch et al., 2000). Such structures are usually characterized by large masses and low resonance frequencies. Therefore, the health monitoring systems designed for civil engineering structures might not be applicable to mechanical structures.

In this thesis, an in-depth study of applying MEMS inertial sensors to perform health monitoring of mechanical structures is presented. Commercially available MEMS inertial sensors are utilized. Characteristics of the selected MEMS inertial sensors are studied using analytical, computation, and experimental methodologies. In addition,

development of instrumentation and methodologies for wireless health monitoring of structures using MEMS inertial sensors is discussed.

MEMS inertial sensors are integrated into two different wireless communication systems: 1) wireless system is designed to transmit analog signals, and 2) wireless system is designed to transmit digital signals. The analog wireless system is characterized by a linear frequency response function in the range of 400 Hz to 16 kHz, which covers the frequency bandwidth of the MEMS inertial sensors. In order to verify the performance and accuracy of the analog wireless system, experimental modal analysis of a mechanical structure is performed. The structure is also modeled with analytical and computational methods and compared with the experimental results.

The digital wireless system is utilized to perform high resolution tilt and rotation measurements of structures subjected to angular and linear acceleration. The calibrated digital wireless MEMS system can achieve angular resolutions of 1.8 mrad. In addition, the developed digital system can be utilized to perform angular rate measurements.

Results of the developments presented in this thesis confirm the potential of using MEMS inertial sensors to perform accurate and effective health monitoring for mechanical structures.

1.1. Design consideration

With today's sophisticated technical systems, there is a need for accurately monitoring their structural behaviors (Van der Auweraer, 2001; Elwenspoek and

Wiegerink, 2001). On the other hand, health monitoring systems need to be reliable and miniaturized in order to increase their versatility to different types of structures and environments. With these design parameters, conventional transducers might not be optimal because they are large in size, require large power actuation, and have narrow frequency bandwidths. In addition, such transducers have high manufacturing costs and, therefore, it is not economical to apply multiple transducers to perform health monitoring of complex structures. In order to satisfy such requirements, MEMS inertial sensors could be used because they are low cost, lightweight, require low power actuation, and have high resolution (Bernstein, 2003; Bergstrom and Li, 2002; Hsu, 2002).

The scope of this thesis is to design a wireless MEMS inertial system to perform effective and accurate health monitoring of mechanical structures. In order to fully utilize the advantages of MEMS technologies, and to achieve a successful design, several design considerations need to be fulfilled. Such considerations include: high measuring accuracy, small size and light weight, and reliable long distance wireless data transfer. Additional considerations include low power consumption and simple driving electronics.

Accuracy of the system is a function of the accuracy of the sensor and the wireless system. Furthermore, the accuracy of a MEMS inertial sensor is a function of its natural frequency, while higher natural frequency yields to higher accuracy of the sensor. The accuracy of a wireless communication link is a function of the quality of the electronics and the transceiver algorithms.

Since the selected MEMS sensors provide both analog and digital outputs, two wireless systems were developed and characterized. To ensure reliable long distance data

transfer, experiments were conducted to determine the reliability and the transmission range of the wireless system.

2. MICROELECTROMECHANICAL SYSTEMS

Microelectromechanical systems (MEMS), comprise of different microscale subsystems and structures, incorporate both mechanical and electrical capabilities into single, miniature devices. MEMS can be used to monitor physical phenomena, such as motion, temperature, chemical composition, etc., and to transduce the detected phenomenon into corresponding electrical signals for measurements and data acquisition (Gad-el-Hak, 2001; Hsu, 2002; Kovacs, 1998; Lyshevski, 2002, 2000).

MEMS available today include but are not limited to: accelerometers, gyroscopes, pressure sensors, temperature sensors, humidity sensors, chemical sensors and micromirrors, etc. Typical MEMS are fabricated using high volume fabrication techniques that were developed based on integrated circuits (ICs) manufacturing techniques. The advanced MEMS fabrication techniques not only ensure high quality devices, but also reduced manufacturing costs. In addition, MEMS are miniaturized in their sizes, require low power operations, and have high measuring accuracies. MEMS are widely utilized in industries such as automotive, aerospace, information technology, biotechnology, etc. (Gad-el-Hak, 2001; Hsu, 2002; Kovacs, 1998; Lyshevski, 2000).

Currently, the automotive industry is one of the largest markets for MEMS and microsystems (Bernstein, 2003; Bergstrom and Li, 2002; Hsu, 2002; Lyshevski, 2000). It is estimated that a total of 447 million sensors have been installed in automobiles in the year 2002, and this number is estimated to grow to 659 million by the year 2009 (Costlow, 2004). These statistics indicate that future automobiles will be heavily relying on developments in MEMS technology.

Utilization of MEMS in automobiles increases the safety, efficiency, and comfort for the riders. Typical applications of MEMS included: airbag deployment systems, navigation systems, antilock brake sensors, various engine and power train sensors, temperature/humidity sensors, security systems, anti-roll, anti-slid, etc. In order to realize higher safety standards, implementation of rollover, tire pressure, and other sophisticated vehicle sensory systems are required. Figure 2.1 shows current and prospective applications of MEMS sensors in automobiles (Hsu, 2002; Madou, 1997).

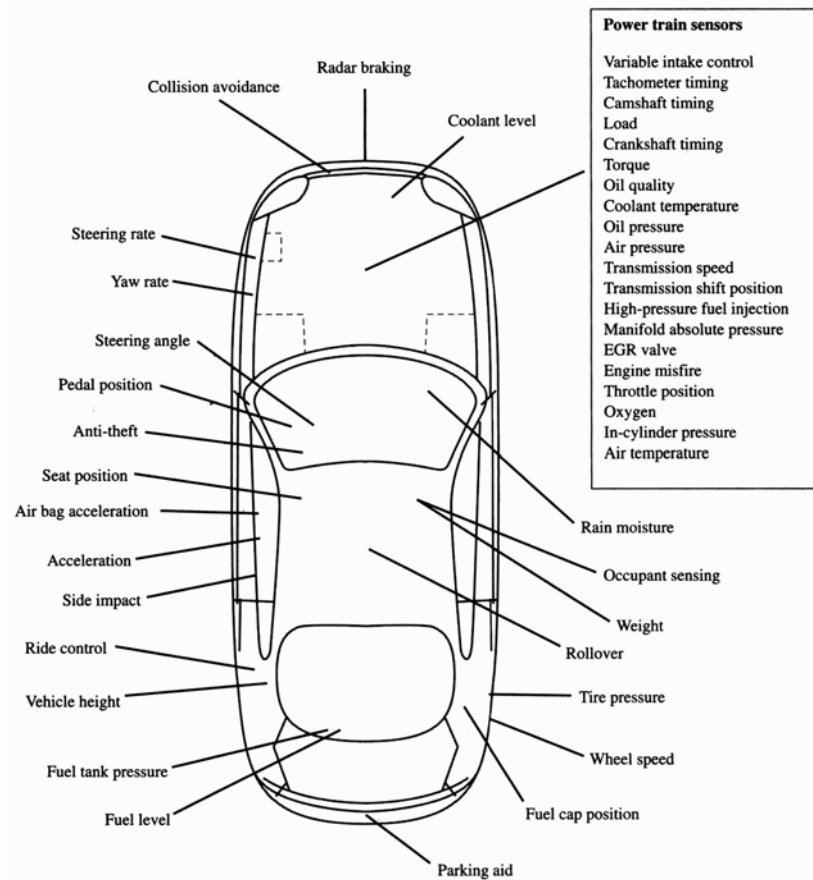


Fig. 2.1. Current and prospective applications of MEMS sensors in automobiles (Hsu, 2002).

2.1. Fabrication of MEMS

MEMS fabrication techniques rely on the infrastructure developed for the IC industries. Major fabrication tools utilized for MEMS manufacturing include photolithography, chemical vapor deposition (CVD), and etching techniques. Photolithography is utilized to produce high precision patterning to define the geometries of MEMS components. CVD is used to deposit materials to make three-dimensional thin layers and etching is utilized to remove selected materials (Gad-el-Hak, 2001; Hsu, 2002; Kovacs, 1998; Lyshevski, 2000; Madou 1997).

The most common techniques utilized today to fabricate MEMS are the bulk micromachining, the surface micromachining, and the LIGA process (Gad-el-Hak, 2001; Hsu, 2002; Kovacs, 1998; Lyshevski, 2000; Madou 1997; WPI, 2002).

2.1.1. Bulk micromachining

Bulk micromachining involves removal of selected materials to create three-dimensional structures. Depending on the material, functionality, design, and the quality of the finished microstructures, different etching techniques and etchants may be utilized. Both wet and dry etchings are common techniques for micromachining (Hsu, 2002; Madou, 1997). Wet etching involves chemicals to dissolve substrate materials and the utilization of appropriate etch stops to prevent over etching. Dry etching involves utilization of suitable reactive gases or vapors to remove substrate materials (Hsu, 2002; Madou, 1997). Figure 2.2 shows a representative step-by-step fabrication process, which

includes bulk micromachining, to make a thin membrane with embedded piezoresistive elements. The first nine steps are the photolithographic processes to form the piezoresistors, and the last step involves the use of an isotropic etching technique to define a cavity in the silicon substrate to form the membrane (Gad-el-Hak, 2001; Hsu, 2002; Kovacs, 1998; Lyshevski, 2000; Madou, 1997).

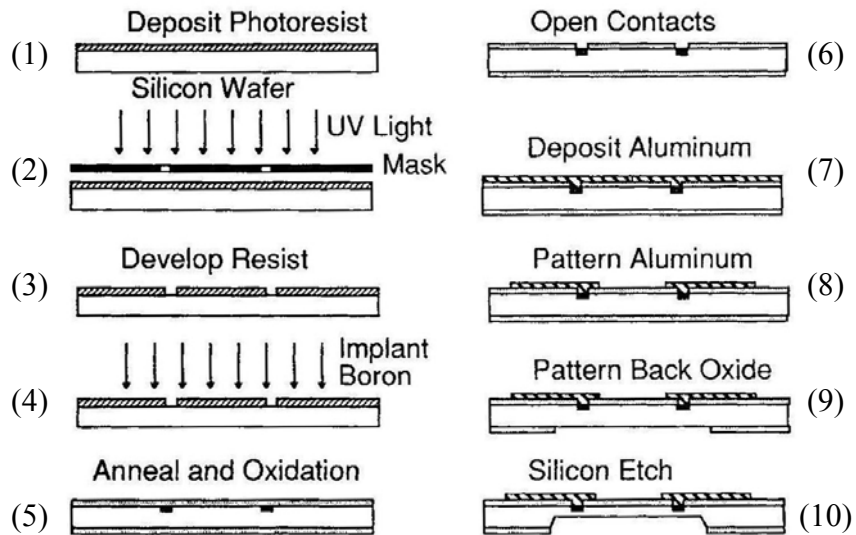


Fig.2.2. Bulk micromachining processes to fabricate a membrane (Madou, 1997).

2.1.2. Surface micromachining

Surface micromachining involves deposition and removal of thin films of materials to fabricate microstructures. In order to build three-dimensional structures using surface micromachining, multiple layers of materials are deposited on top of a silicon substrate. The fabrication processes also rely on deposition of sacrificial layers used to pattern and to create the depth and thickness of the desired MEMS structures.

One of the advantages of surface micromachining is that it allows the fabrication of complex three-dimensional microstructures (Hsu, 2002; Kovacs, 1998; Lyshevski, 2000, WPI, 2002).

Figure 2.3 summarizes the surface micromachining process. In process (1), a sacrificial layer, usually made of phosphosilicate glass (PSG), is deposited on the silicon substrate by low pressure chemical vapor deposition (LPCVD) technique. In process (2), a mask is used to photolithographically pattern and etch the sacrificial layer. In process (3), a layer of polysilicon is deposited over the patterned sacrificial layer. In process (4), a second mask is applied to pattern the polysilicon microstructure. Process (5) shows the final free standing microstructure, after the complete removal of the sacrificial layer (Gad-el-Hak, 2001; Hsu, 2002; Kovacs, 1998; Lyshevski, 2000; Madou, 1997, WPI, 2002).

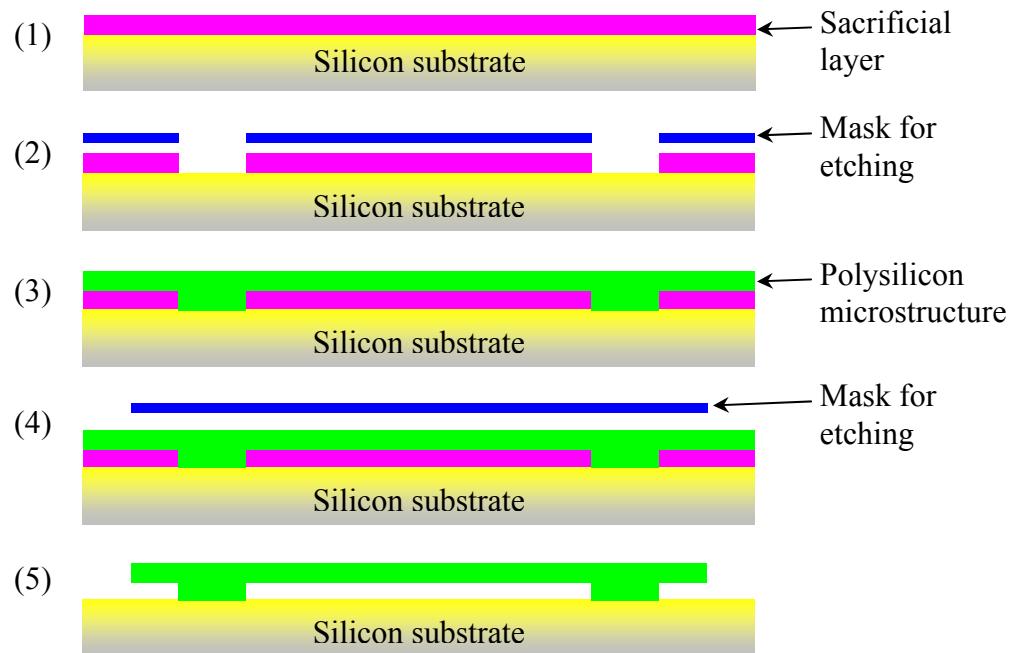


Fig. 2.3. Fabrication process of a surface micromachined component (Hsu, 2002; Kovacs, 1998; Lyshevski, 2000; Gad-el-Hak, 2001, WPI, 2002).

2.1.3. LIGA process

LIGA is the German acronym for “Lithographie, Galvanoformung, Abformung”, which stands for lithography, electroforming, and molding. The LIGA fabrication process is based on utilization of specific photoresistive materials, typically polymethylmethacrylate (PMMA), and x-rays to make high aspect ratio microstructures. Figure 2.4 illustrates fabrication process of a LIGA component. According to Fig. 2.4, in process (1), a mask is used to expose, with x-rays, a thick layer of PMMA photoresistive to pattern the geometry of the structure to be fabricated. The mask is usually made of gold, or a material that is opaque to x-rays. In process (2), the exposed photoresist is removed and in process (3), the patterned PMMA photoresist is electroplated with a metal layer. In process (4), the microstructure is obtained after removal of the redundant PMMA photoresist (Gad-el-Hak, 2001; Hsu, 2002; Kovacs, 1998; Lyshevski, 2000; Madou, 1997).

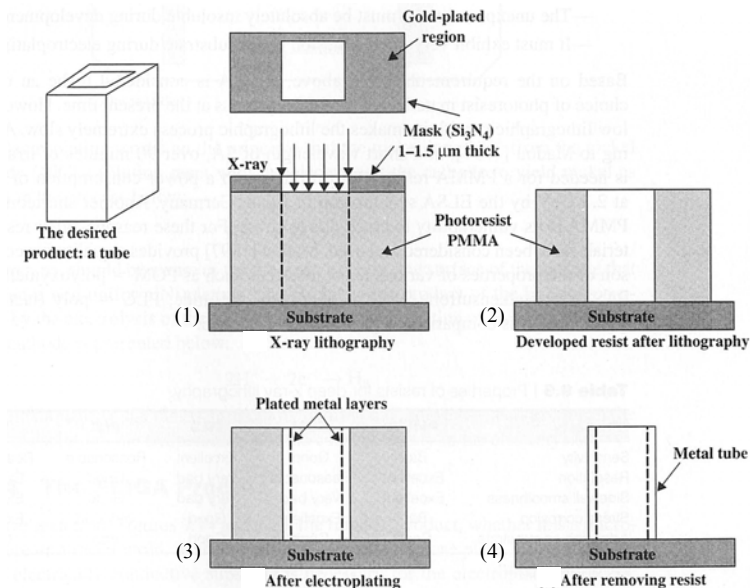


Fig. 2.4. Fabrication process of a LIGA component (Hsu, 2002).

2.2. MEMS inertial sensors

The developments of surface micromachining techniques allow batch-fabrication of high quality MEMS inertial sensors. These MEMS inertial sensors not only have small sizes and high measuring accuracy, but also have high sensitivity, wide operational temperature ranges, and high reliability (Kok et al., 2003a). Because of these advantages, MEMS inertial sensors are widely used in various industries for different applications (Bergstrom and Li, 2002; Bernstein, 2003; Caveo, 2003; Dao et al., 2002; Hsu, 2002; L-3 Communications, 2004; Segway, 2004; Weinberg, 2002). Moreover, with their great design flexibility, new applications of MEMS inertial sensors are continuously being developed. For instance, recent research demonstrates applications of MEMS inertial sensors, integrated with RF technology and microprocessors, to perform wireless health monitoring of structures (Chung et al., 2003; Lynch, 2004; Tanner et al., 2003).

Two types of MEMS inertial sensors are available: MEMS accelerometers utilized to measure linear motion and orientation, and MEMS gyroscopes utilized to measure angular speed.

MEMS inertial sensors transduce motions into electrical signals and there are different designs of sensing mechanisms available to accomplish such function. Typical sensing mechanisms utilized in MEMS inertial sensors include piezoresistive, piezoelectric, capacitive, resonant membranes, and thermal sensing technology (Elwenspoek and Wiegerink, 2001; Gad-el-Hak, 2001; Hsu, 2002; Kovacs, 1998; Lyshevski, 2000; MEMSIC 2002). Each of these signal transducers require different fabrication techniques and operate using different signal conditioning circuitry.

2.2.1. Piezoresistive inertial sensors

Piezoresistive inertial sensors, also referred to as strain gauge inertial sensors, operate using Wheatstone bridge circuits to transduce specific phenomena of interest into electrical signals. Figure 2.5 shows configuration of a Wheatstone bridge circuit, which consists of four piezoresistors. The characteristic of piezoresistors is that their electrical resistance changes when subjected to mechanical strains. Therefore, measurements are obtained by measuring the differences between input and output voltages by (Hsu, 2002; Johari, 2003)

$$V_o = V_{in} \left(\frac{R_1}{R_1 + R_4} - \frac{R_3}{R_2 + R_3} \right), \quad (2.1)$$

where V_o and V_{in} are the output and the input voltage of the Wheatstone bridge, and R_1 to R_4 are the resistors used to define the Wheatstone bridge, respectively.

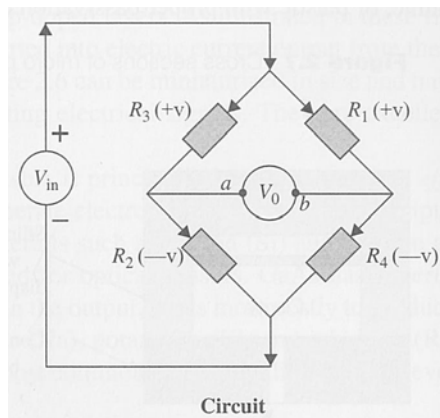


Fig. 2.5. Circuit diagram of a Wheatstone bridge (Hsu, 2002).

Using this mechanical and electrical principle, piezoresistive inertial sensors are constructed with a proof mass, suspended by spring elements, and integrated with a

silicon diaphragm that consists of piezoresistors in a Wheatstone bridge configuration. In the event of mechanical accelerations, deformations of the diaphragm caused by the motion of the proof mass, induce mechanical strains and, therefore, changes in the electrical resistance of the piezoresistors. Figure 2.6 shows schematics of the top and the cross sectional view of a piezoresistive inertial sensor.

Piezoresistive inertial sensors have the advantage of a simple configuration, which does not require specialized fabrication processes. The drawback of piezoresistive inertial sensors is that they are sensitive to changes in operating temperatures, which limits their application in the environments that are not thermally stable (Hashimoto, 1999; Hsu, 2002; Khazan, 1994; Kovacs, 1998; Yazdi et al., 1998).

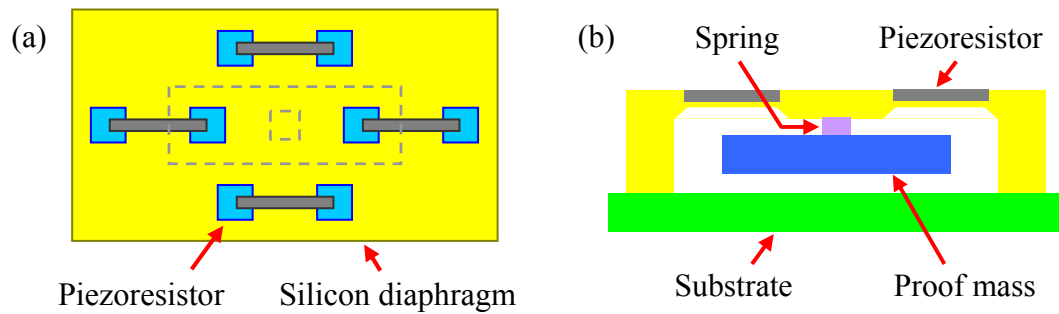


Fig. 2.6. Schematic of a piezoresistive inertial sensor: (a) top view showing configuration of piezoresistors to define a Wheatstone bridge configuration and, (b) cross sectional view showing the proof mass and the spring mechanism.

2.2.2. Piezoelectric inertial sensors

Piezoelectric inertial sensors operate based on the piezoelectric effect that occurs in specific materials. The characteristic of piezoelectric materials is that they generate an

electrical potential when subjected to mechanical strains, and vice versa. Figure 2.7 depicts the piezoelectric effect.

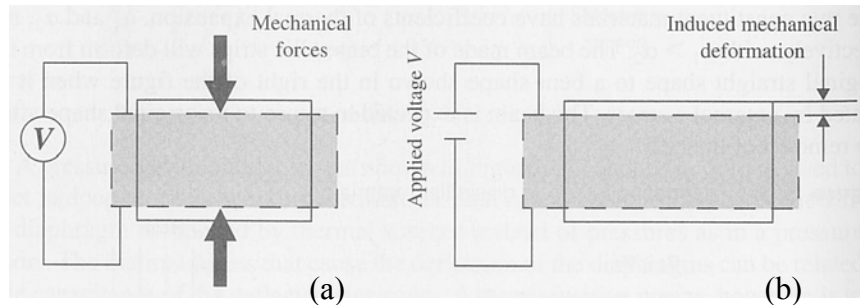


Fig. 2.7. Schematic depicting the piezoelectric effect: (a) electrical potential induced by the deformation of a piezoelectric material and, (b) deformation induced by application of an electrical potential (Hsu, 2002).

The most common configurations used in piezoelectric inertial sensors are cantilevers and sandwich configurations. These configurations are shown in Fig. 2.8. In the cantilever configuration, a piezoelectric material is sputtered on the surface of the cantilever. In the sandwich configuration, a piezoelectric component is placed under the proof mass, which in turn is attached to the frame of the device by spring elements. In both configurations, motions applied to the device induce deformations, which in turn deform the piezoelectric material and a proportional electrical potential is generated.

Piezoelectric inertial sensors require low power actuations and have a high mechanical stability. However, they can only respond to dynamic excitations, and they have no sensitivity to static loads (Hsu, 2002; Johnson, 1997; Kulwanoski and Schnellinger, 2004; Shear, 1999).

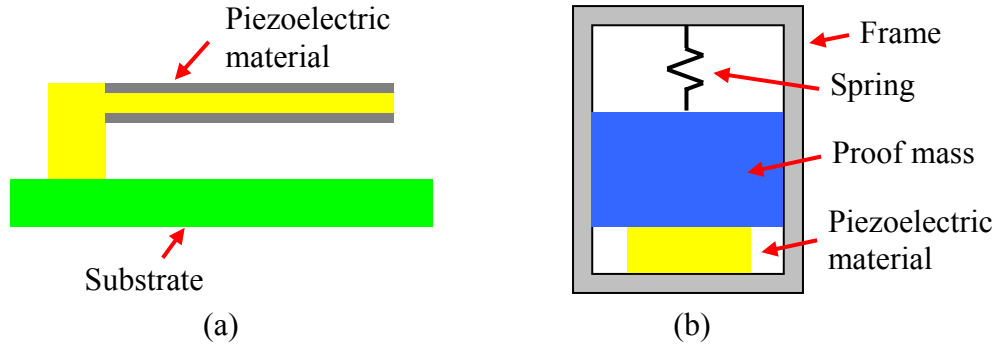


Fig. 2.8. Two configurations of piezoelectric inertial sensors: (a) cantilever and, (b) sandwich.

2.2.3. Capacitive inertial sensors

Capacitive inertial sensors operate based on the principle of measuring capacitance variations in electromechanical capacitors. Figure 2.9 shows a capacitor defined by two parallel plates. In this configuration, the capacitance, C , is determined as

$$C = \epsilon_r \epsilon_o \frac{A_p}{d} \quad , \quad (2.2)$$

where A_p is the overlapping surface area of the plates, d is the gap between the plates, and ϵ_o and ϵ_r are the permittivity of free space and the relative permittivity of the dielectric media between the plates, respectively (Hsu, 2002; Lyshevski, 2000).

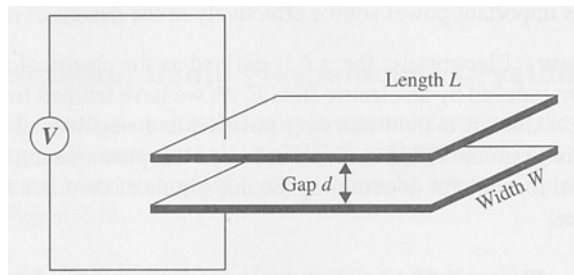


Fig. 2.9. Parallel plates capacitor (Hsu, 2002).

To achieve adequate sensitivity and accurate acceleration measurements, a single set of capacitive plates is insufficient (Hsu, 2002; Lyshevski, 2000). Therefore, multiple capacitive sensing electrodes are utilized. Figure 2.10 shows schematic of a single axis capacitive inertial sensor, which consists of a proof mass, spring element, and multiple capacitive electrodes. There are two types of capacitive electrodes: the fixed electrodes attached to the substrate and the moving electrodes attached to the proof mass. Each moving electrode is aligned between two fixed electrodes. Such configuration is often referred to as capacitive combs configuration (Hsu, 2002). In Fig. 2.10, A is the overlapping area between pairs of the capacitive electrodes, and d_1 and d_2 are the gaps between the fixed and the moving electrodes. These gap distances are on the order of a few micrometers (Elwenspoek and Wiegerink, 2001; Hsu, 2002; Kovacs, 1998; Lyshevski, 2000).

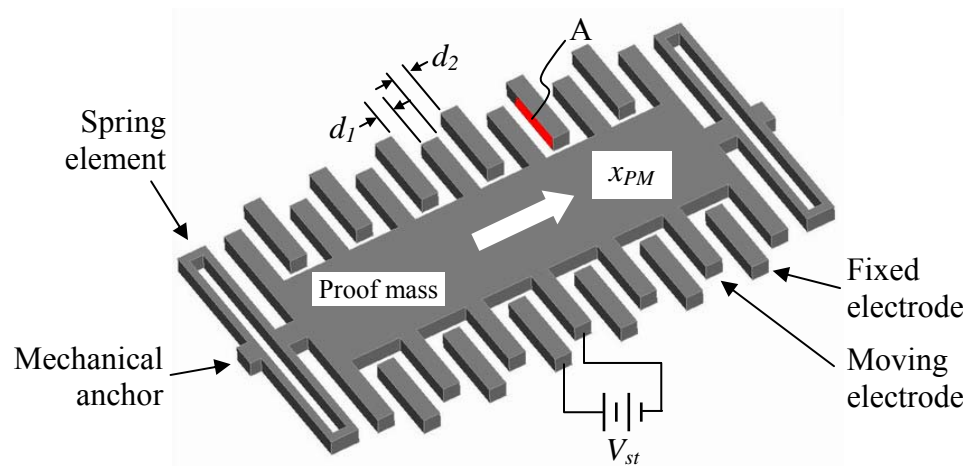


Fig. 2.10. Schematic of a single axis capacitive MEMS inertial sensor.

The principle of operation of capacitive inertial sensors is based on measurements of changes in capacitance between the capacitive combs. Without any motions, the proof

mass is centered at its initial position, and the capacitances of the left side and right side of the moving electrodes are equal. When motions are applied, the proof mass displaces in the opposite direction to the applied motion, and induces capacitance variations. For small displacements of the proof mass, d_{PM} , Eq. 2.2 can be written as (Lyshevski, 2000)

$$C_1 = \frac{\varepsilon_r \varepsilon_o A}{d_1 + d_{PM}} \quad \text{and} \quad C_2 = \frac{\varepsilon_r \varepsilon_o A}{d_2 - d_{PM}} \quad . \quad (2.3)$$

By setting

$$\varepsilon = \varepsilon_r \varepsilon_o \quad , \quad (2.4)$$

the capacitance difference, ΔC , is determined as

$$\Delta C = C_1 - C_2 = \frac{2\varepsilon A d_{PM}}{d_{PM}^2 - d_1^2} \quad \text{or} \quad \Delta C d_{PM}^2 - 2\varepsilon A d_{PM} - \Delta C d_1^2 = 0 \quad . \quad (2.5)$$

Since the proof mass has a small displacement, the terms $\Delta C d_{PM}^2$ can be neglected. Therefore, correlation between displacement of the proof mass and the change in capacitance can be written as

$$d_{PM} \approx -\frac{d_1^2}{2\varepsilon A} \Delta C \quad . \quad (2.6)$$

In addition, Hook's law states that the restoring force of a spring, F_s , is proportional to its displacement. Assuming that the spring element is an ideal spring, and by applying Newton's second law of motion, acceleration, a_{acc} , of the proof mass can be calculated by

$$F_s = k_s d_{PM} = m_{PM} a_{acc} \quad \text{or} \quad a_{acc} = \frac{k_s}{m_{PM}} d_{PM} \quad , \quad (2.7)$$

where k_s is the spring constant, and m_{PM} is the mass of the proof mass. By substituting Eq. 2.6 into 2.7, accelerations can be determined by measuring changes in capacitance as

$$a_{acc} = -\frac{k_s d_1^2}{2m_{PM} \epsilon A} \Delta C \quad . \quad (2.8)$$

Capacitive inertial sensors have the advantages of: (1) good stability across a wide temperature range, (2) can be fabricated using a variety of micromachining techniques, such as bulk and surface micromachining, (3) have a low power consumption, and (4) can be fabricated with different materials. Therefore, capacitive inertial sensors have become one of the most widely utilized signal transducers in MEMS (Bergstrom and Li, 2002; Bernstein, 2003).

2.2.4. Resonant inertial sensors

Resonant inertial sensors operate based on the principle of measuring the axial force exerted onto a resonant member. Such inertial sensors operate using two modes: one mode is used to excite the resonant members, and the other mode is used to measure induced motions. Typical configurations of resonant inertial sensors consist of a resonating mass attached to multiple spring elements, Fig. 2.11. The resonating mass is driven in one direction at a predefined frequency while the sensing axis is defined orthogonal to the driving direction (Hsu, 2002; Jeong et al., 2004; Yazdi et al., 1998).

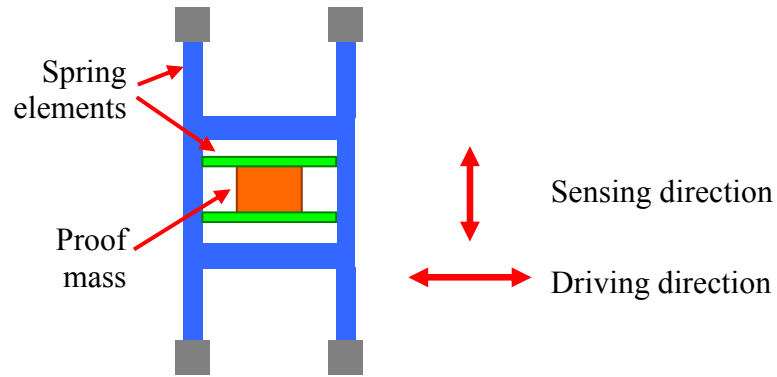


Fig. 2.11. Typical configuration of a MEMS resonator.

Resonant inertial sensors have the advantages of having high sensitivities and high resolutions. However, they require sophisticated signal conditioning circuitry to control the frequency and the magnitude of the resonating member (Bergstrom and Li, 2002; Hsu, 2002).

2.3. System control methodologies

System control can be accomplished by open-loop and closed-loop methodologies. Open-loop control involves measuring changes in electrical signals due to the displacement of the sensing mechanism. The sensing mechanism utilized in open-loop control systems remains at static positions when no excitations are applied. Based on their theories of operation, piezoresistive, piezoelectric, and capacitive devices fall in the category of open-loop control systems. In contrast, closed-loop control systems require force feedback from the moving sensing mechanisms. The sensing mechanisms of closed-loop control systems are excited at known frequencies and amplitudes. When

motions are applied, the sensing mechanisms displace and require force balancing to maintain their original orientations. The resonant inertial sensors operate in closed-loop control methodologies (Bergstrom and Li, 2002; Kovacs, 1998).

2.4. MEMS accelerometers

In this thesis, capacitive MEMS accelerometers are utilized in the developments. Capacitive MEMS accelerometers provide high measuring accuracy and they are sensitive to gravitational accelerations, which enable high-resolution measurements of tilt and rotations (Elwenspoek and Wiegerink, 2001; Hsu, 2002; Rao, 1995).

2.4.1. Analog Devices ADXL202 accelerometer

In this thesis, the Analog Devices ADXL202 dual-axes accelerometer has been utilized. This MEMS accelerometer is used in a wide range of consumer, industrial, military, and automotive applications (Analog Devices, 2001; Hsu, 2002; Kovacs, 1998).

The ADXL202 accelerometer has a measuring range of ± 2 g ($g = 9.81 \text{ m/s}^2$). It provides both analog and digital output signals, with sensitivities of 312 mV/g and 12.5 %/g, respectively. It requires 3 V to 5.25 V for operation and is capable of operating in a wide range of temperatures. Table 2.1 summarizes characteristics of the ADXL202 accelerometer (Analog Devices, 2001; Analog Devices, 2004).

Table 2.1. Pertinent characteristics of the MEMS accelerometers utilized in the developments (Analog Devices, 2001).

Measuring range	Resonance frequency	Sensitivity (Analog outputs)	Sensitivity (Digital output)
$\pm 2g$	10 kHz	312 mV/g	12.5 %/g
0g duty cycle	Operating voltage	Weight	Operating temp.
50%	3.0 to 5.25 V	160 mgr	-40 to 85 °C

Two different ceramic packages are available for the ADXL202 accelerometer, one is a $5 \times 5 \times 2 \text{ mm}^3$ eight pin leadless chip carrier (LCC) package and the other is a $9.9 \times 7.4 \times 3 \text{ mm}^3$ fourteen pin dual-in-line (DIP) package. The LCC package has small size and light weight, and the DIP package provides easy integration to surface mount systems. The accelerometer also has an evaluation board version with all the driving electronics built in, which allows quick and simple integration to develop prototype systems (Analog Devices, 2001; Analog Devices, 2004). Figure 2.12 shows different packages of the ADXL202 accelerometer.

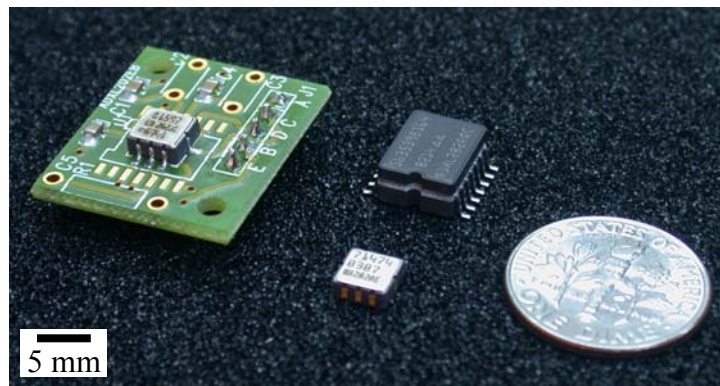


Fig. 2.12. Different electronic packages of the dual-axes ADXL202 MEMS accelerometer fabricated by Analog Devices (Analog Devices, 2001).

Figure 2.13 shows the die of the ADXL202 accelerometer. The micromechanical sensor is located at the center of the die, which is surrounded by the driving electronics and the signal conditioning circuitry. Figure 2.14 shows details of the microelectromechanical sensor, which consists of a polysilicon micromechanical proof mass, four pairs of spring elements, and four sets of capacitive combs. The proof mass has a dimension of $600 \times 600 \times 3 \mu\text{m}^3$, and it has a weight of approximately $0.1 \mu\text{gr}$. According to the manufacturer, the proof mass is suspended $1.6 \mu\text{m}$ from the substrate (Analog Devices, 2001; Analog Devices, 2004; Furlong and Pryputniewicz, 2002; Kok et al., 2003a, 2003b).

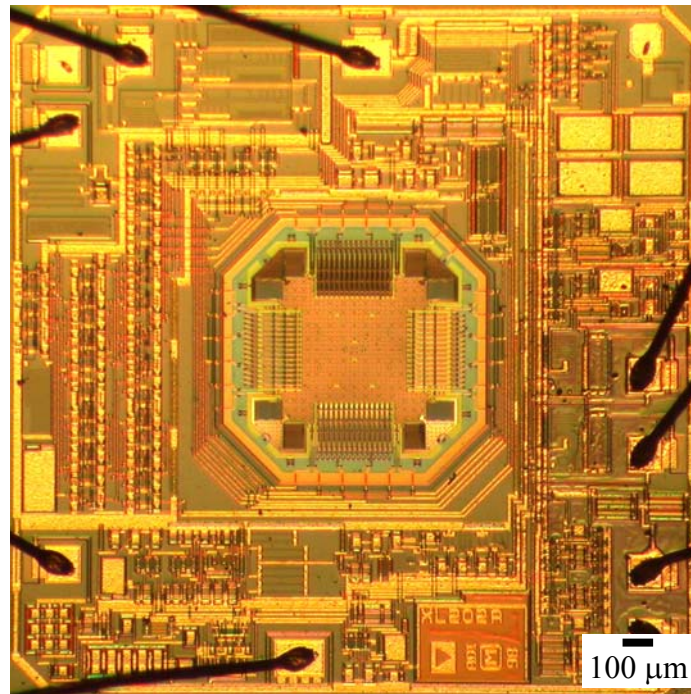


Fig. 2.13. Die of the Analog Devices ADXL202 accelerometer. The microelectromechanical sensor, surrounded by CMOS electronics, is located at the center of the die.

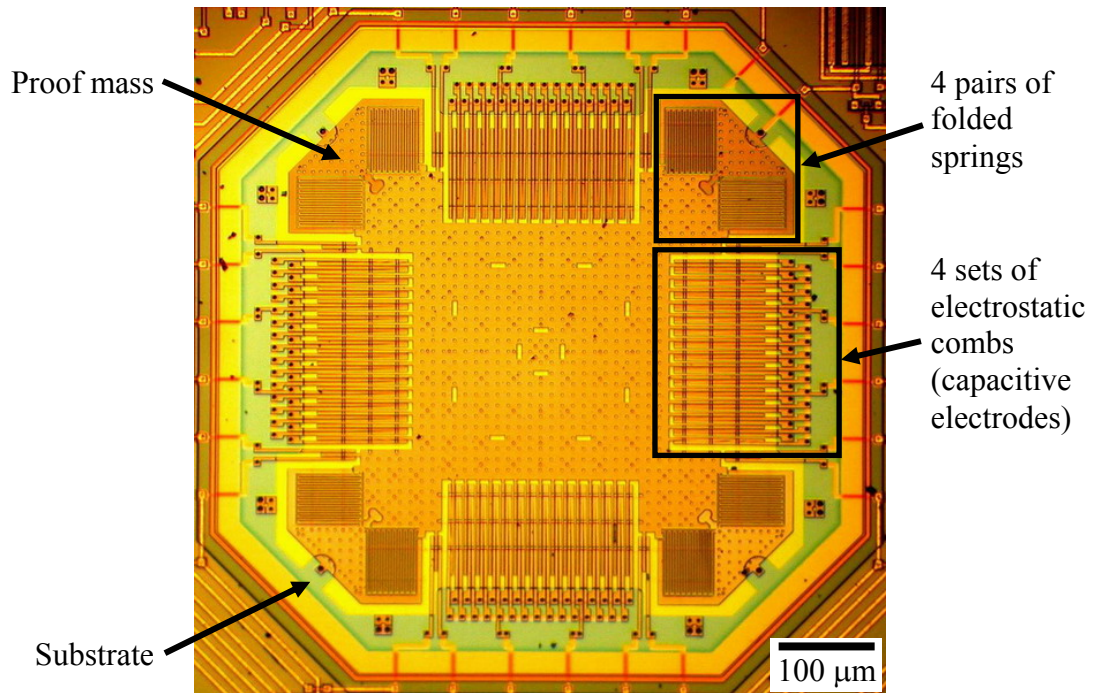


Fig. 2.14. Details of the microelectromechanical sensor of the ADXL202 accelerometer.

Figure 2.15 shows a schematic of the MEMS sensor, which illustrates principle of operation of the dual-axes accelerometer. The tethers, or spring elements, are utilized to constrain movements of the proof mass. According to Fig. 2.15, the vertical capacitive electrodes are used to sense motions in the x -axis, and the horizontal capacitive electrodes are used to sense motions in the y -axis.

The proof mass is attached to a reference frame by four sets of spring elements, located at the four corners of the proof mass. Each set of spring elements consists of two multi-folded springs. The folded springs are orientated in such a way that they are perpendicular to each other in order to allow motions of the proof mass in the horizontal and vertical directions, respectively, providing dual-axes sensitivity. Figure 2.16 shows a

scanning electron microscope (SEM) micrograph of one set of folded-springs and the corresponding degrees of freedom of each individual spring.

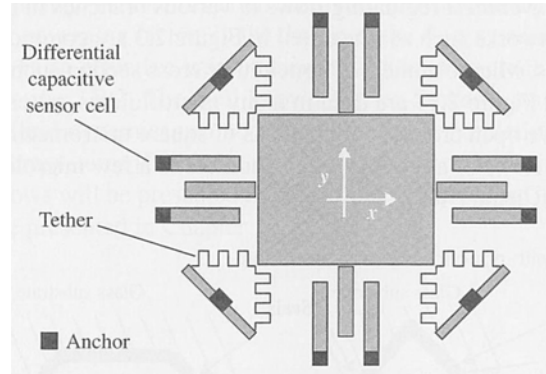


Fig. 2.15. Schematic showing the principle of operation of a dual-axis accelerometer (Hsu, 2002).

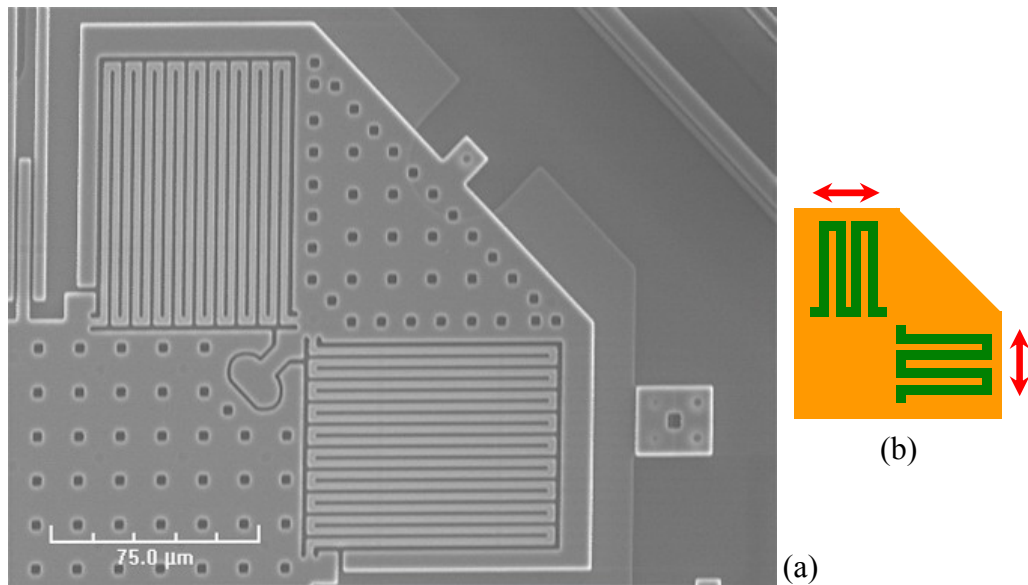


Fig. 2.16. One set of folded springs of the ADXL202 accelerometer: (a) SEM micrograph showing details of the springs and, (b) schematic showing the corresponding degrees of freedom of each multi-fold spring.

Figure 2.17 shows the stopper that connects the spring elements and the proof mass. Its unique design prevents over travel in any one direction and helps to prevent contact of the capacitive plates. Figure 2.18 depicts SEM micrograph showing 3D view of one set of folded springs. From to the SEM pictures, the thickness of the micromechanical sensors is measured at approximately 3 μm .

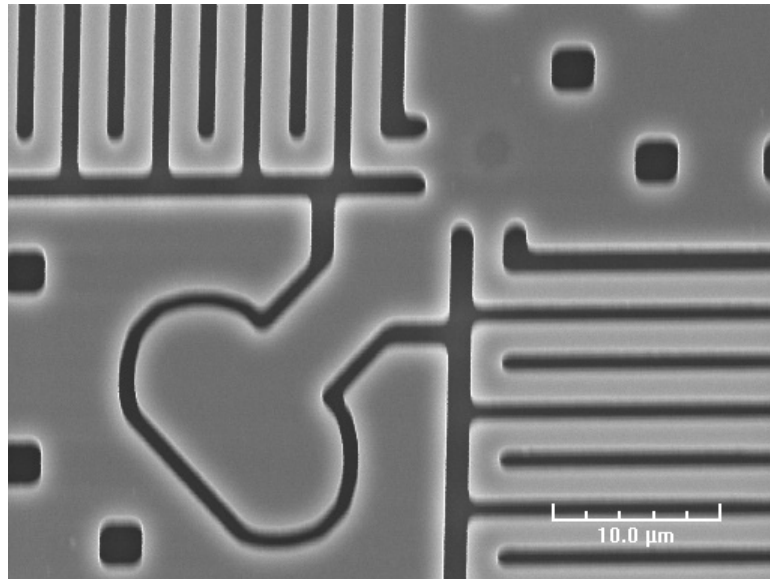


Fig. 2.17. Stopper mechanism of the ADX1202 accelerometer. Stopper is attached to the folded springs and the proof mass.

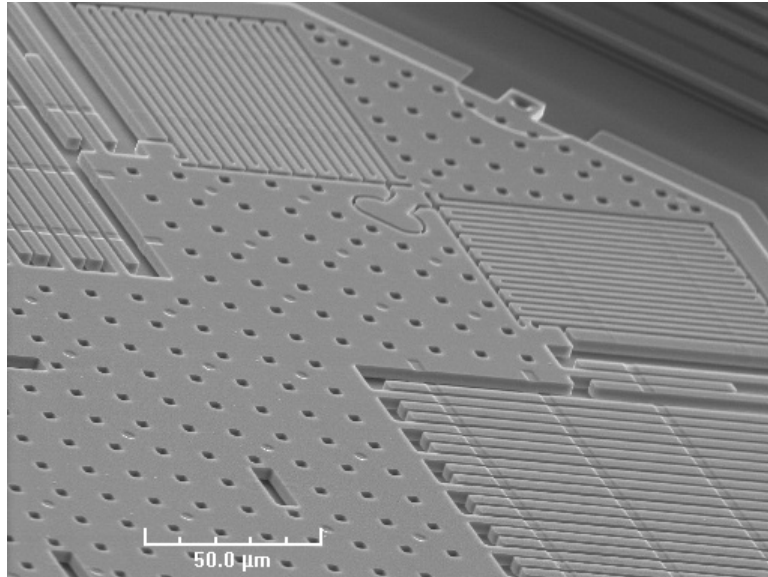


Fig. 2.18. SEM micrograph showing 3D view of one set of folded springs.

Four sets of capacitive combs are utilized to obtain dual-axes measurements. The capacitive combs are defined by moving electrodes on the proof mass and by fixed electrodes on the substrate. By measuring the differences in capacitance within the combs, acceleration measurements, as well as tilt and rotation measurements, can be achieved (Analog Devices, 2001; Furlong and Pryputniewicz, 2002; Kok et al., 2003a, 2003b). Figure 2.19 shows SEM micrograph of the capacitive combs and schematic of the fixed and the moving capacitive electrodes. Figure 2.20 depicts SEM micrograph showing 3D view of the capacitive combs. The width of the finger electrode is approximately $2.5 \mu\text{m}$, and the gap is approximately $1.3 \mu\text{m}$.

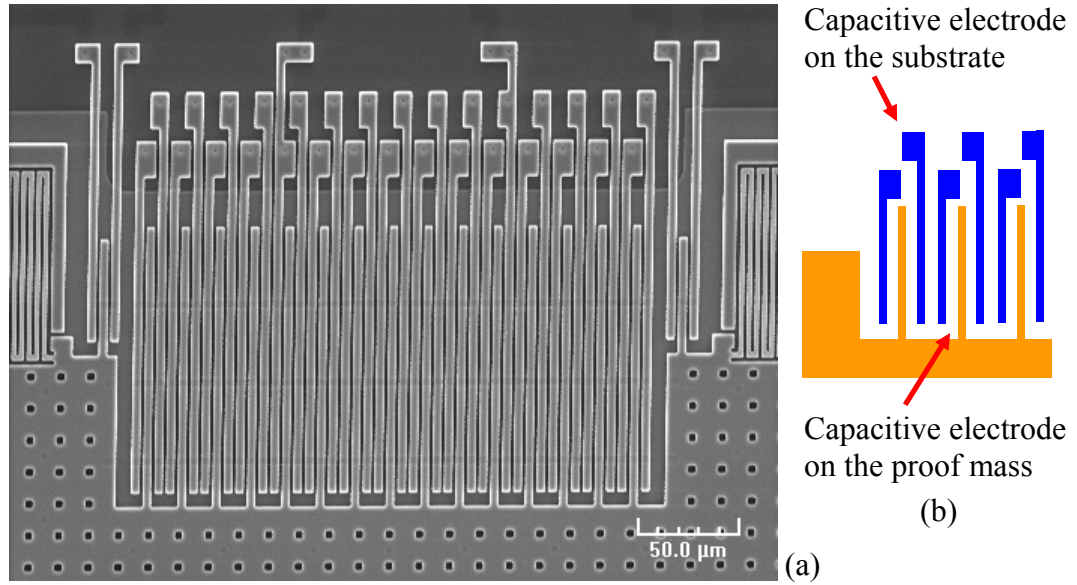


Fig. 2.19. One set of capacitive combs: (a) SEM micrograph and, (b) schematic showing the fixed and the moving capacitive electrodes. The capacitive combs, as shown in (a), are sensitive to horizontal motions.

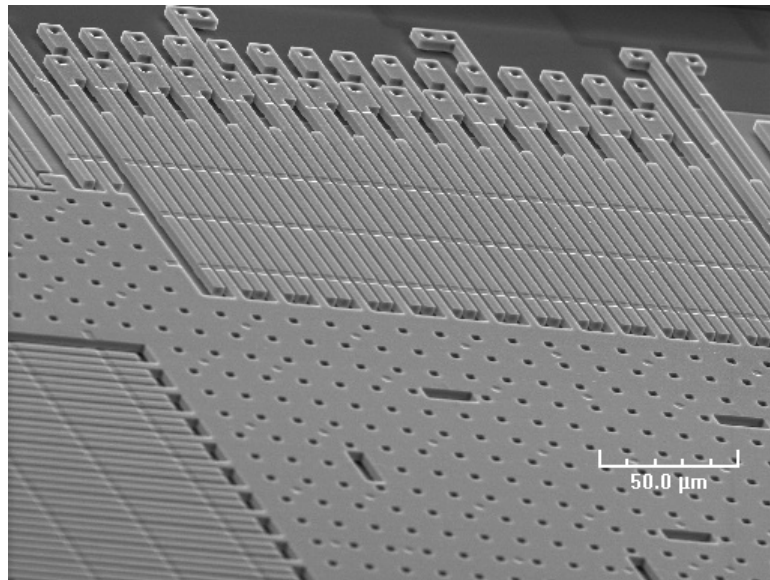


Fig. 2.20. SEM micrograph showing 3D view of one set of electrostatic combs.

2.5. MEMS gyroscopes

A MEMS gyroscope is an instrument used to measure angular rates of rotation through detection of Coriolis accelerations. The principle of Coriolis effect, illustrated in Figure 2.21, states that tangential speed of a mass on a rotating disk increases when the mass moves from the center of rotation to the edge of the rotating platform. In addition, the force exerted on the mass is opposite and orthogonal to the direction of rotation (Bergstrom and Li, 2002; Elwenspoek and Wiegerink, 2001; Geen and Krakauer, 2003; Kovacs, 1998).

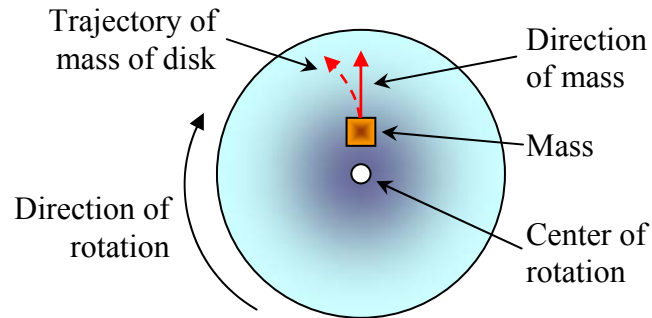


Fig. 2.21. Illustration of the Coriolis effect.

Coriolis acceleration, a_{cor} , is calculated as (Bergstrom and Li, 2002; Elwenspoek and Wiegerink, 2001; Geen and Krakauer, 2003; Kovacs, 1998)

$$a_{cor} = 2\Omega v_m \quad , \quad (2.9)$$

where Ω is the angular rate of rotation of the platform and v_m is the radial velocity of the mass on the platform. The Coriolis force, F_{cor} , experienced by the mass, m_{cor} , is calculated as

$$F_{cor} = 2m_{cor}\Omega v_m \quad . \quad (2.10)$$

Almost all of the MEMS gyroscopes use resonant members to sense Coriolis acceleration. MEMS gyroscopes are constructed with two systems: the resonant system to drive the sensing mechanism, and the capacitive system to measure the rotations (Jeong et al., 2004; Yazdi et al., 1998).

Figure 2.22 shows configuration of a typical MEMS gyroscope. Major components of MEMS gyroscopes include: proof mass, spring elements, capacitive combs, and inner frame. The proof mass, also referred to as the resonating mass, is attached to an inner frame by sets of spring elements and it is driven to oscillate in one direction. The inner frame is attached to the substrate by another set of spring elements, which are perpendicular to the spring elements of the resonating mass. Such configuration provides two degrees of freedom that allows the gyroscope to sense Coriolis accelerations (Allen and Jenkins, 2003).

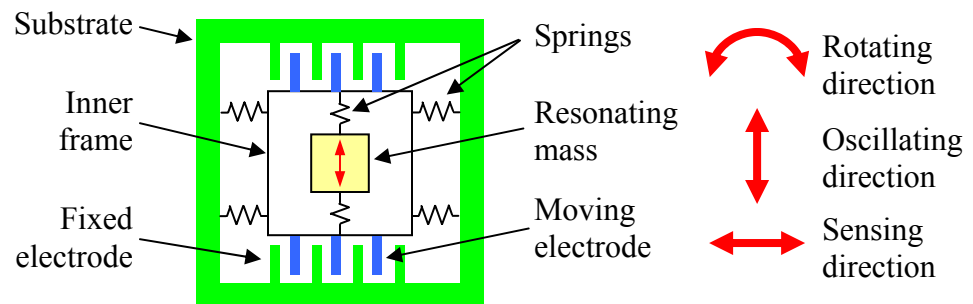


Fig. 2.22. Schematic showing general configuration of a MEMS gyroscope.

In the event of rotations, the orthogonal force exerted on the resonating mass induces displacement of the inner frame. To measure rates of rotation, capacitive

electrodes are defined on both the inner frame and the substrate to form sets of capacitive combs. By measuring changes in capacitance within the combs, the angular rate can be determined (Analog Devices, 2003a, 2003b, 2003c; Bergstrom and Li, 2002; Elwenspoek and Wiegerink, 2001; Geen and Krakauer, 2003).

2.5.1. Analog Devices ADXRS150 gyroscope

The Analog Devices ADXRS150 gyroscope was also utilized in the developments of this Thesis. This gyroscope is capable of measuring angular rates of $\pm 150^\circ/\text{s}$ and it requires a 5 V source for operation. The gyroscope has a null voltage output of 2.5 V, and it provides linear analog outputs that vary from 0.25V to 4.75V, depending on the input rate and the direction of rotation. Table 2.2 summarizes pertinent characteristics of the ADXRS150 gyroscope (Analog Devices, 2004; Analog Devices, 2003a, 2003b, 2003c) and Fig. 2.23 shows different electronic packages.

Table 2.2. Pertinent characteristics of the MEMS gyroscopes utilized in the developments (Analog Devices 2003b, 2003c).

Measuring range	Sensitivity	Initial Null
$\pm 150^\circ/\text{s}$	12.5mV/ $^\circ/\text{s}$	2.5 V
Output signal rate	Resonance frequency	Operating voltage
0.25V to 4.75V	14 kHz	4.75 to 5.25 V

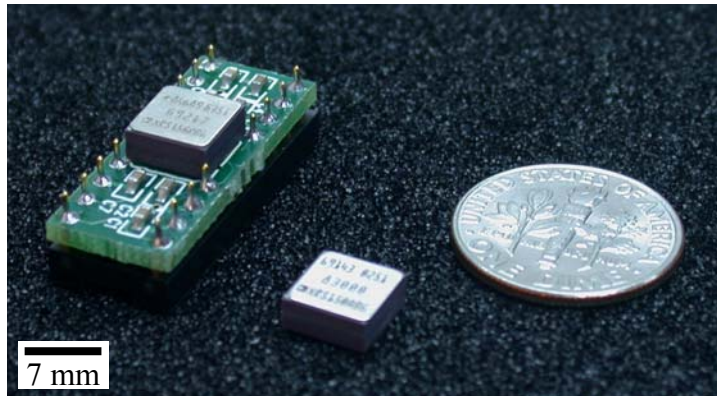


Fig. 2.23. Evaluation board and packages of the ADXRS150 MEMS gyroscope fabricated by Analog Devices (Analog Devices, 2003b).

Figure 2.24 shows the die of the ADXRS150 gyroscope. The microelectromechanical sensor is located at the center of the die, and it is surrounded by the signal conditioning circuitry. Figure 2.25 shows details of the MEMS sensor, which consists of two polysilicon resonating masses, the inner frame, the capacitive combs, and the driving electrodes that are used to excite the mass. Figure 2.26 shows a schematic diagram of one of the two resonating masses. According to Fig. 2.26, the resonating masses oscillate along the x -axis, and the inner frame is free to move along the y -axis. Therefore, the device is sensitive to rotations, in both clockwise and counterclockwise directions.

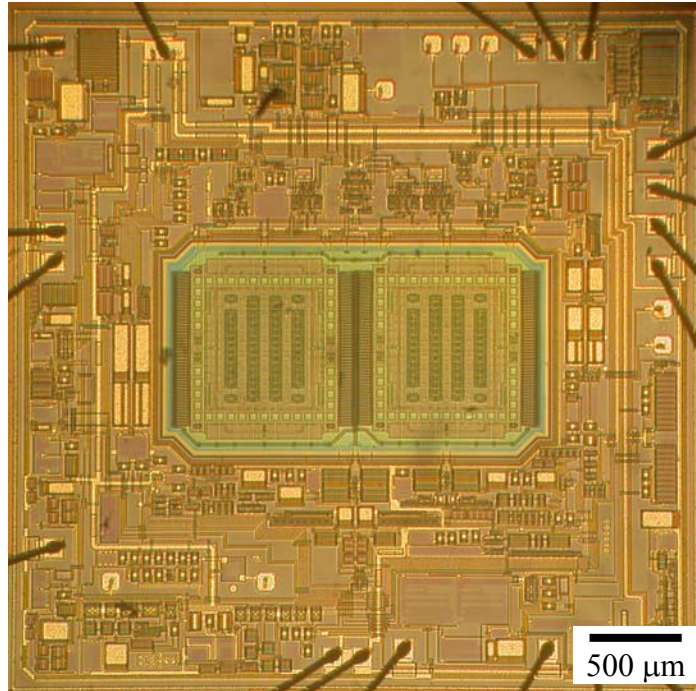


Fig. 2.24. Die of the Analog Devices ADXRS150 gyroscope. The microelectromechanical sensor, surrounded by CMOS electronics, is located at the center of the die.

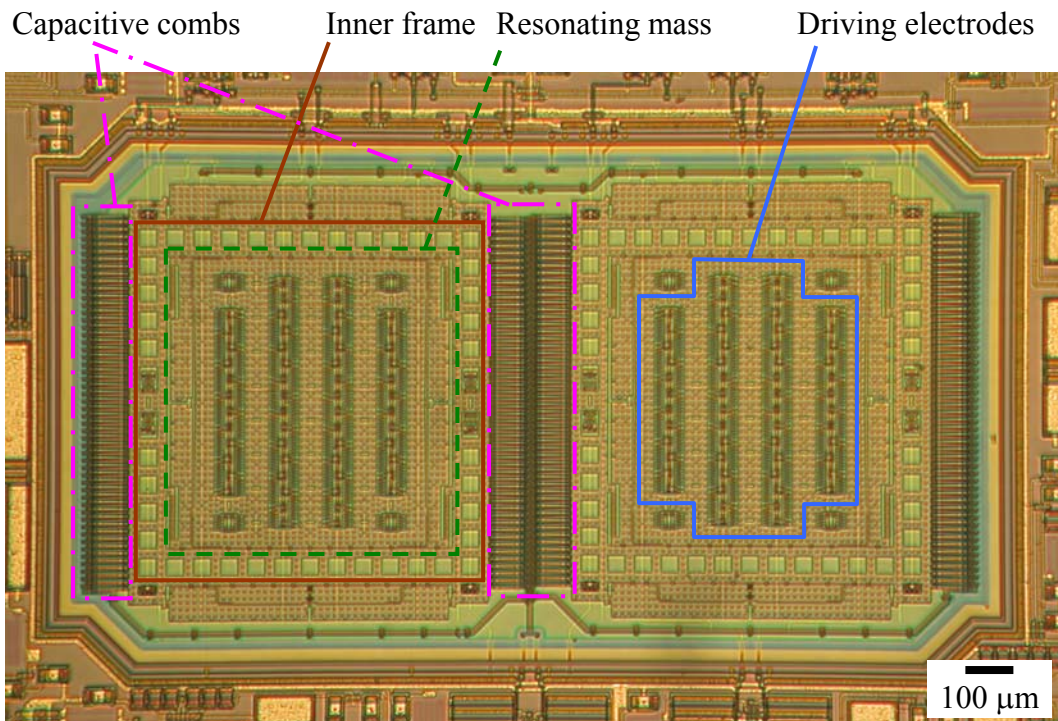


Fig. 2.25. Details of the microelectromechanical sensor of the ADXRS150 gyroscope.

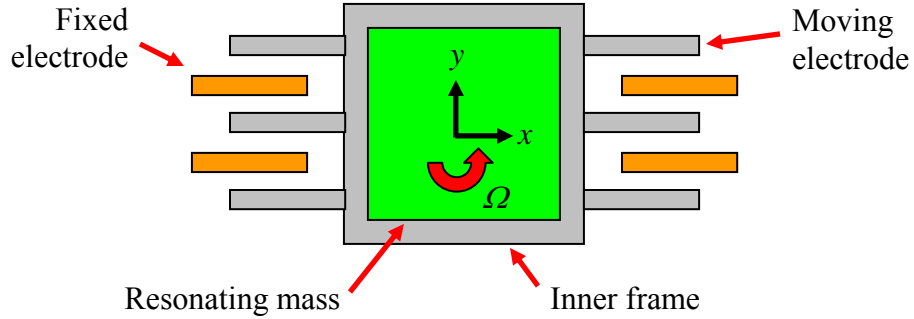


Fig. 2.26. Schematic showing the principle of operation of a MEMS gyroscope.

Figure 2.27 shows details of the spring element of the resonating mass, the velocity sensing electrodes, section of the capacitive combs, and section of the driving electrodes of the microelectromechanical sensor. Four spring elements and four velocity sensing fingers are utilized at each corner of each resonating mass. Figures 2.28 and 2.29 show SEM micrographs of sections of the capacitive combs.

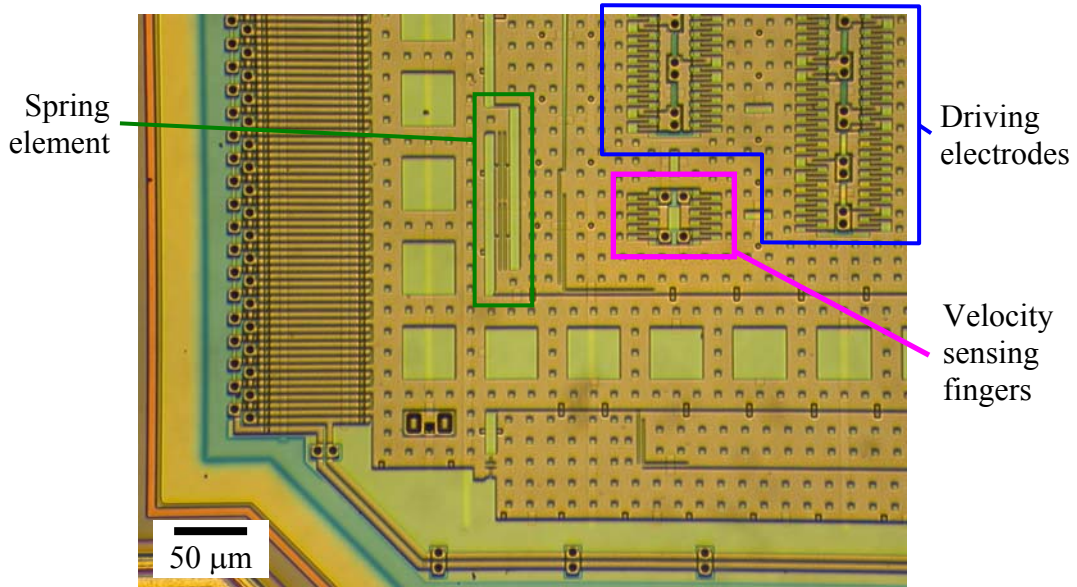


Fig. 2.27. Micrograph showing the spring element and the velocity sensing finger of the microelectromechanical sensor of the ADXRS150 MEMS gyroscope.

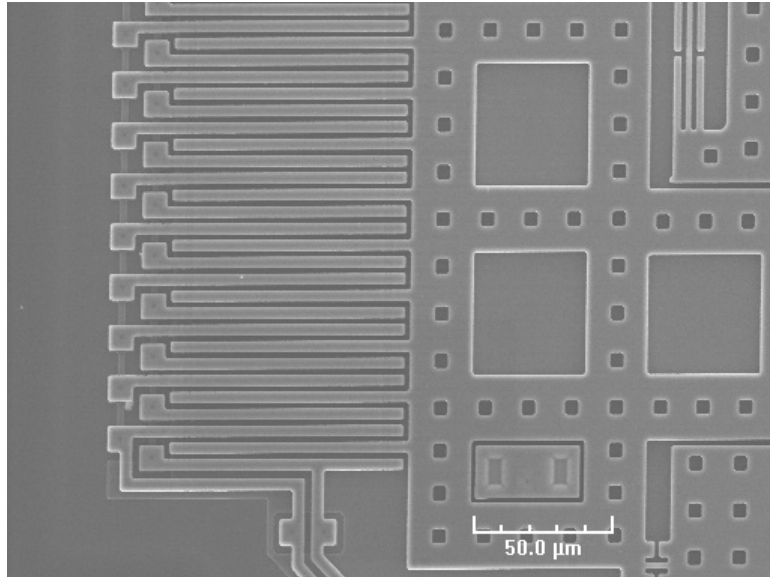


Fig. 2.28. SEM micrograph showing details of a set of electrostatic combs of the ADXRS150 gyroscope.

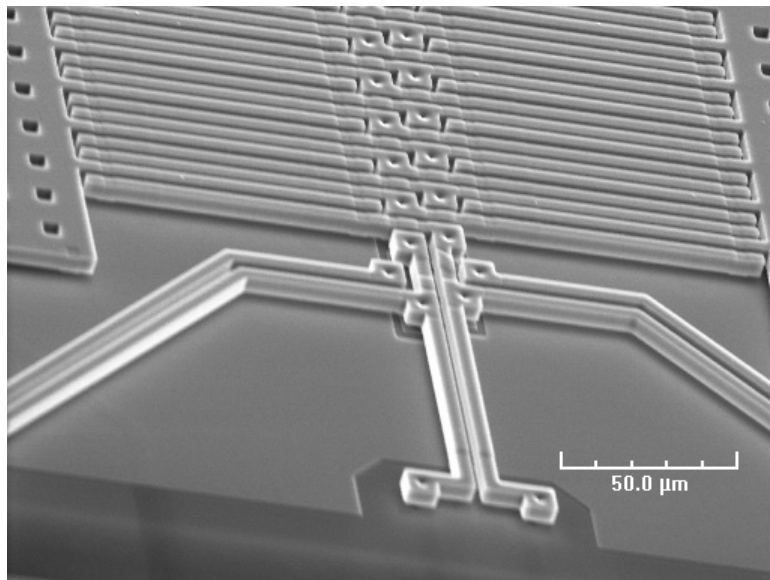


Fig. 2.29. SEM micrograph showing 3D view of section of the electrostatic combs of the ADXRS150 gyroscope.

3. CHARACTERIZATION OF MEMS ACCELEROMETERS

MEMS accelerometers convert mechanical motions into electrical signals. They are operated by two systems, the mechanical sensor to measure the motions, and the electrical circuitry to convert measurements into output signals. Figure 3.1 shows a mechanical configuration of a single axis accelerometer, which consists of a proof mass, m , spring element, k , and damper, c . In order to measure motions, the accelerometer is attached to an object of interest in such a way that its sensitivity axis, x , is in the direction of motion of the object. Inertial measurements are performed by measuring the displacement of the proof mass relative to the base of the accelerometer (Kok et al., 2003a, 2003b; Thomson and Dahleh, 1998; Rao, 1995).

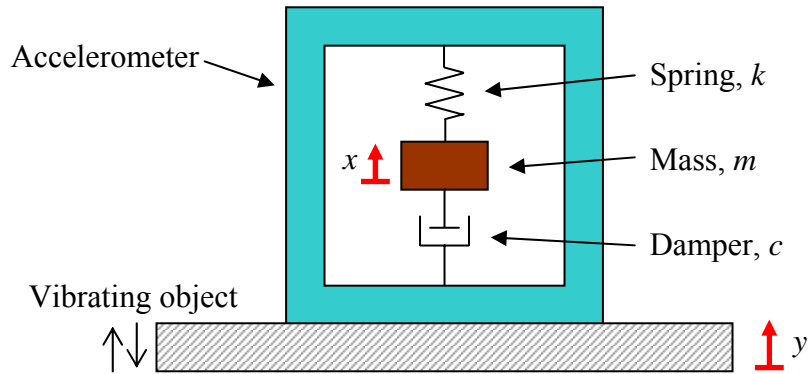


Fig. 3.1. Configuration of a single axis accelerometer.

The measuring accuracy, measuring sensitivity, and the frequency bandwidth of the accelerometer are controlled by the quality and characteristics of the mechanical sensor. In this thesis, characterization of the accelerometers is based on utilization of analytical, computational, and experimental methodologies. Analytical methods are used

to evaluate measuring accuracy of the MEMS accelerometer while computational methods, based on the finite element method (FEM), are used to determine the natural frequencies and modes of vibration of the proof mass. Experimental methods are utilized to verify the measuring accuracy and to characterize the natural frequencies of the accelerometer (Kok et al., 2003a, 2003b; Thomson and Dahleh, 1998; Rao, 1995).

3.1. Analytical considerations

For the accelerometer described in Fig. 3.1, the equation of motion of the mass, m , can be written as (Kok et al., 2003a, 2003b; Thomson and Dahleh, 1998; Rao, 1995)

$$m(\ddot{x} - \ddot{y}) + c(\dot{x} - \dot{y}) + k(x - y) = 0 \quad , \quad (3.1)$$

where x and y are the displacements of the mass and the vibrating object, respectively.

The relative displacement of the mass with respect to the vibrating object, z , can be written as

$$z = x - y \quad . \quad (3.2)$$

Assuming the vibrating object is subjected to harmonic motion as

$$y(t) = \beta \sin(\omega t) \quad , \quad (3.3)$$

with β and ω are the amplitude and frequency of motion of the vibration object.

Substitute the harmonic motion of Eq. 3.3 into Eq. 3.1 yields

$$m\ddot{z} + c\dot{z} + kz = -m\ddot{y} \quad . \quad (3.4)$$

Therefore, the governing equation of motion of the systems becomes

$$m\ddot{z} + c\dot{z} + kz = m\omega^2 \beta \sin(\omega t) \quad . \quad (3.5)$$

Solution of Eq. 3.5 indicates that the steady-state component of motion is

$$z(t) = H \sin(\omega t - \phi) \quad , \quad (3.6)$$

where

$$H = \frac{\beta \left(\frac{\omega}{\omega_n} \right)^2}{\sqrt{\left[1 - \left(\frac{\omega}{\omega_n} \right)^2 \right]^2 + \left[2\zeta \left(\frac{\omega}{\omega_n} \right) \right]^2}} \quad , \quad (3.7)$$

is the amplitude of oscillation, and

$$\phi = \tan^{-1} \left[\frac{2\zeta \left(\frac{\omega}{\omega_n} \right)}{1 - \left(\frac{\omega}{\omega_n} \right)^2} \right] \quad , \quad (3.8)$$

is the phase of the displacement function, Eqs 3.6. In Eqs 3.7 and 3.8, ω_n is the natural frequency, and $\zeta = c / 2m\omega_n$, is the damping ratio. Analysis of Eq. 3.7 indicates that the quantity

$$\Gamma = \left\{ \left[1 - \left(\frac{\omega}{\omega_n} \right)^2 \right]^2 + 2\zeta \left(\frac{\omega}{\omega_n} \right) \right\}^{1/2} \quad , \quad (3.9)$$

approaches unity when

$$\frac{\omega}{\omega_n} \rightarrow 0 \quad , \quad (3.10)$$

so that

$$H = \frac{1}{\omega_n^2} \omega^2 \beta \quad , \quad (3.11)$$

indicating that z , as defined in Eq. 3.6, is proportional to the acceleration $\omega^2\beta$ of the reference frame with a proportionality factor of $1/\omega_n^2$. Therefore, Eqs 3.6 to 3.11 indicate that by measuring the motions of the proof mass it is possible to measure accelerations applied to the reference frame (Kok et al., 2003a, 2003b; Thomson and Dahleh, 1998; Rao, 1995).

Equation 3.11 is only valid when condition of Eq. 3.10 is fulfilled. However, according to Eqs 3.6 and 3.7, measured accelerations include the effects of the function, Γ , shown in Eq. 3.9. Therefore, indicating the existence of measuring deviations. Figure 3.2 shows $1/\Gamma$ as a function of frequency ratio for various damping ratios. According to Fig. 3.2, the effects of deviations, for highly accurate measurements, can be minimized by: (a) utilizing an accelerometer with a high natural frequency, (b) limiting the measuring range to a fraction of the natural frequency of the accelerometer, and (c) controlling the damping ratio. Due to their large stiffness to mass ratios, MEMS accelerometers are characterized by high natural frequencies, therefore, providing high measuring accuracy in wide frequency ranges while providing minimum distortions in the measurements.

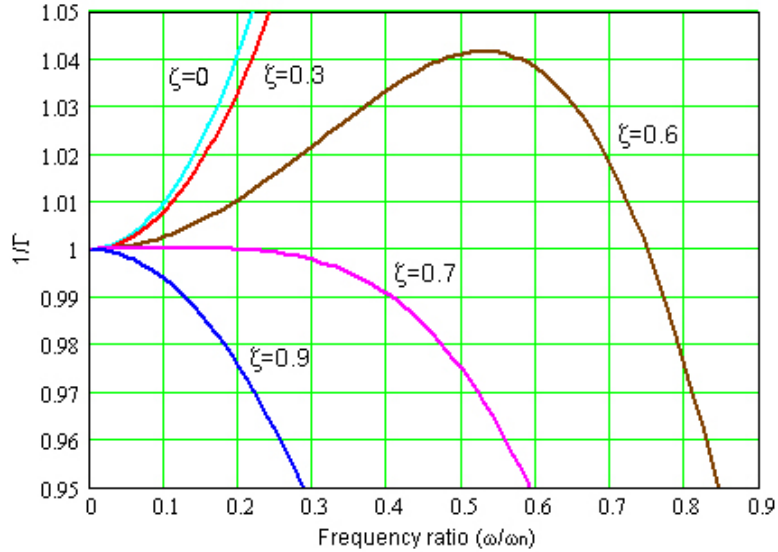


Fig. 3.2. Measuring deviations, $1/\Gamma$, as a function of frequency ratio for specific damping ratios.

3.2. Computational considerations

Analytical solutions indicate that high natural frequency of MEMS accelerometers allow high measuring accuracy in wide frequency ranges. Therefore, accurate characterization of the fundamental natural frequencies of MEMS accelerometers helps determining their operational frequency range and accuracy. In order to perform such characterization, computational analysis based on the finite element method (FEM) was applied.

An axisymmetric model of the proof mass was developed as a part of the investigations in this Thesis. Figure 3.3 shows the computation model of the proof mass and the corresponding boundary conditions. Polycrystalline silicon with material properties characterized by the modulus of elasticity, E , of 160 GPa and mass density, ρ ,

of 2.33 gr/cm^3 were utilized. Thickness of the proof mass, according to manufacturer's specifications, is $3 \text{ }\mu\text{m}$ (Analog Devices, 2001; Analog Devices, 2004; Furlong and Pryputniewicz, 2002; Kok et al. 2003a, 2003b; Pro/Engineer, 2001; Toogood, 1998, 2000).

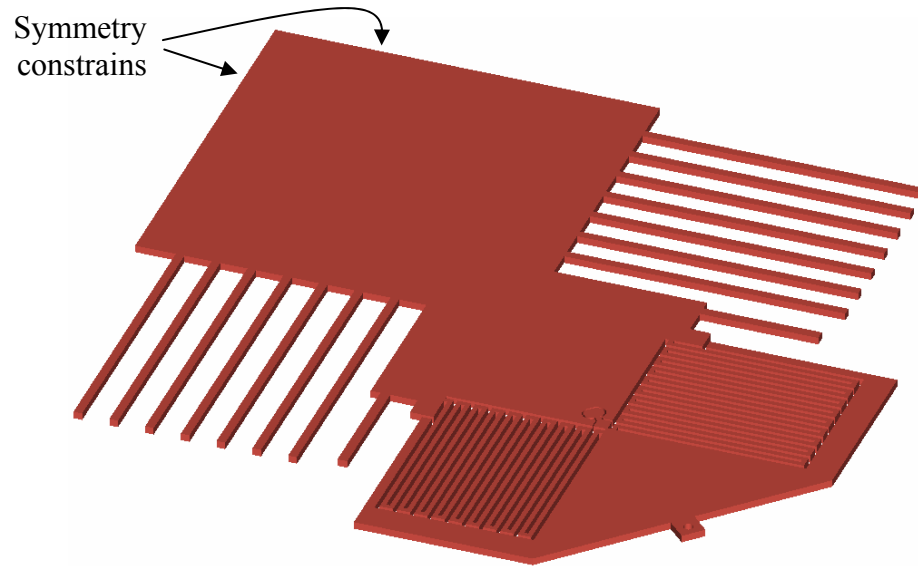


Fig. 3.3. Axisymmetric FEM model of the proof mass, folded springs, and moving combs of an ADXL202 accelerometer (Kok et al. 2003a, 2003b).

Solving an eigenvalue problem, corresponding to undamped free-vibrations, allows determination of modal characteristics of the proof mass. Figures 3.4 to 3.8 display FEM calculated mode shapes corresponding to the first five modes of vibration and Table 3.1 summarizes the FEM results and the corresponding frequencies (Kok et al. 2003a; Toogood, 2000).

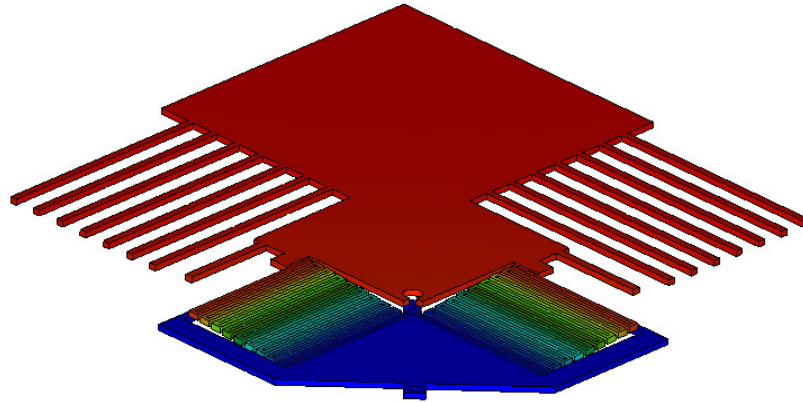


Fig. 3.4. First mode of vibration calculated at 8.48 kHz.

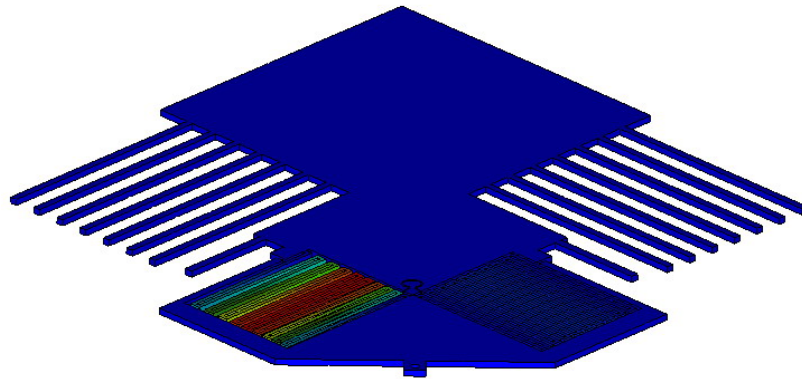


Fig. 3.5. Second mode of vibration calculated at 77.10 kHz.

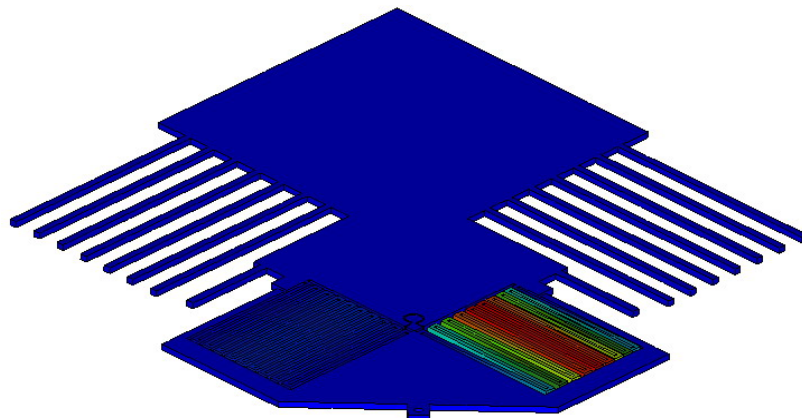


Fig. 3.6. Third mode of vibration calculated at 77.42 kHz.

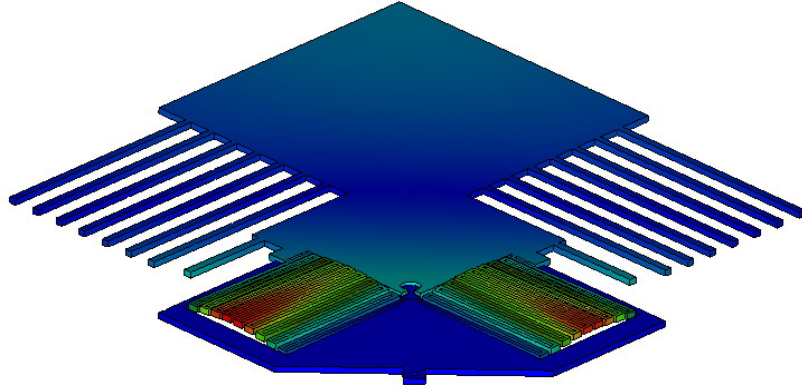


Fig. 3.7. Fourth mode of vibration calculated at 86.02 kHz.

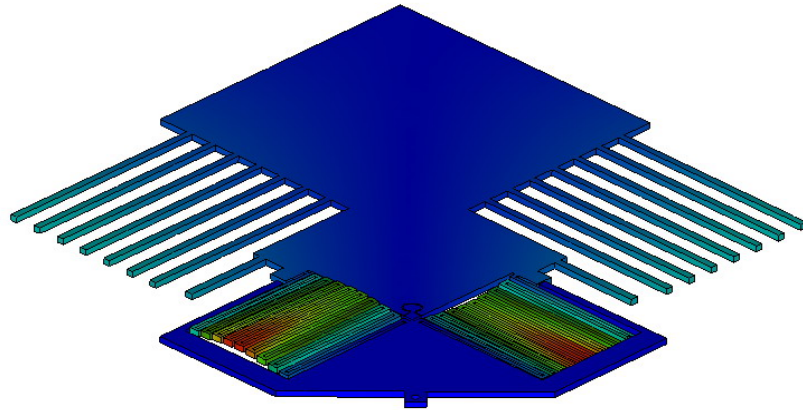


Fig. 3.8. Fifth mode of vibration calculated at 90.68 kHz.

Table 3.1. FEM calculated modes of vibrations of the proof mass: E is 160GPa, ρ is 2.33 gr/cm³, and thickness is 3 μ m.

Mode number	Frequency, kHz	Modes of vibration
1	8.48	1st bending
2	77.10	In-plane (x -axis)
3	77.42	In-plane (y -axis)
4	86.02	2nd bending
5	90.68	Torsion

Additional FEM analyses to perform parametric investigations on the fundamental natural frequency of the proof mass as a function of the modulus of elasticity and its thickness were conducted. The first analysis involved determination of the natural frequency versus the thickness of the proof mass. A fixed value of E of 160 GPa was utilized and the thickness was varied 20% from its nominal dimension of 3 μm (from 2.4 to 3.6 μm).

The second analysis involved determination of the natural frequency versus modulus of elasticity of the proof mass. Thickness of 3 μm was utilized and the modulus of elasticity was varied from 120 – 220 GPa, which covered typical modulus of elasticity of polycrystalline silicon. The mass density of 2.33 g/cm^3 was utilized in both of the parametric investigations.

Figures 3.9 and 3.10 summarize the results of the parametric analyses. Figure 3.9 shows that the natural frequency of the proof mass varies from 8.00 kHz to 10.25 kHz for thickness variations between 2.4 to 3.6 μm . Figure 3.10 shows that the natural frequency of the proof mass varies from 7.34 kHz to 9.94 kHz for E varying from 120 to 220 GPa. Results of both analyses demonstrate linear relationships between changing these properties versus the natural frequency of the proof mass.

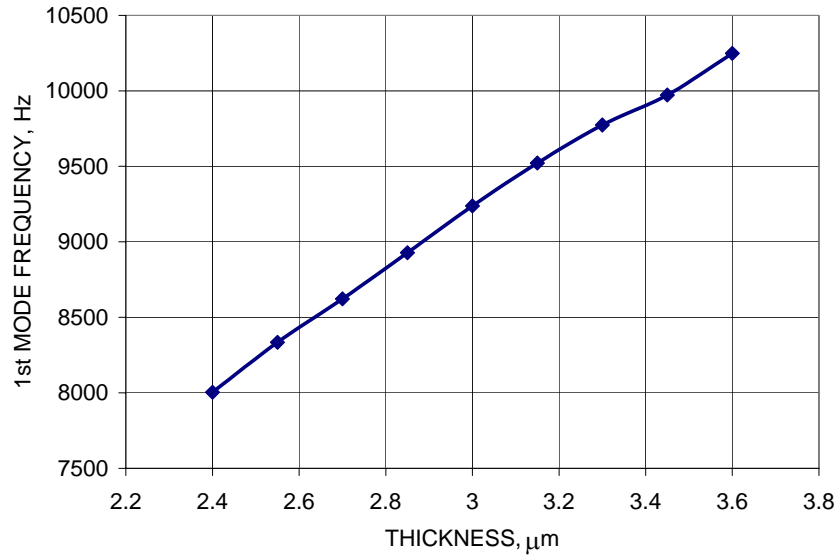


Fig. 3.9. FEM determined fundamental natural frequency versus thickness of the proof mass, E is 160 GPa and ρ is 2.33 g/cm^3 .

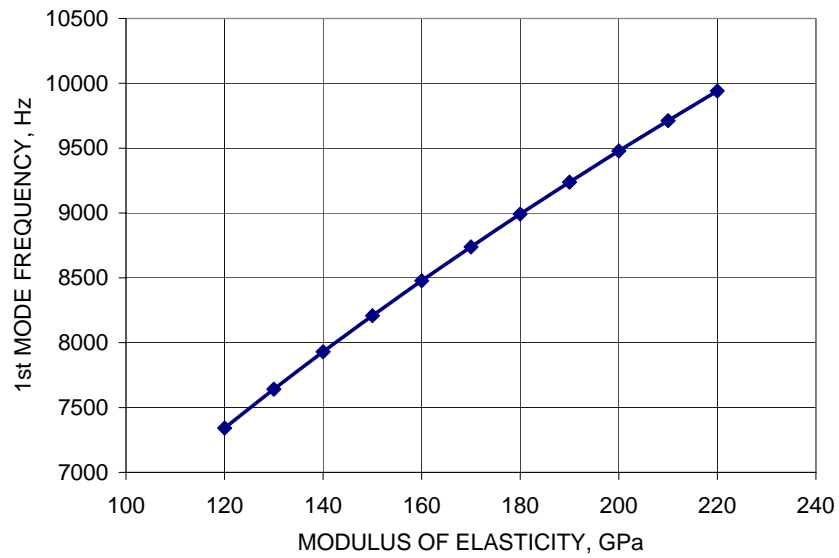


Fig. 3.10. FEM determined fundamental natural frequency versus modulus of elasticity, E , of the proof mass, thickness is 3 μm and ρ is 2.33 g/cm^3 .

3.3. Experimental considerations

Experimental investigations were performed to study the dynamic characteristics of the MEMS accelerometers, including determination of their frequency response and damping ratios. Experiments consisted of exciting the MEMS accelerometers with a piezoelectric shaker and measuring their output frequency response functions with a dynamic signal analyzer. Laser vibrometer measurements were also performed for verification of the measurements. Specific circuitry for signal conditioning of the output responses of the MEMS accelerometers was developed.

3.3.1. Experimental setup

Figure 3.11 shows major components of the experimental setup that was developed based on utilization of a laser vibrometer system. In the configuration shown in Fig. 3.11, a dynamic signal analyzer (SA) is utilized to generate excitation signals to drive a piezoelectric shaker (PZT) through the amplifier (AMP). SA is also utilized for analyzing the output signals generated by the MEMS accelerometer under test (MEMS) and the output of the laser vibrometer (VM). VM consists of an optical head (OH), fiber optic interferometer (FI), and a vibrometer controller (VC) (Polytec PI, 1994). The MEMS accelerometer is mounted on a mirror (MR), which is mounted onto the PZT. MR is used as a reference surface for the OH. The MEMS accelerometer is driven by a variable power source (PS) (Kok et al., 2003a, 2003b; Polytec PI, 1994).

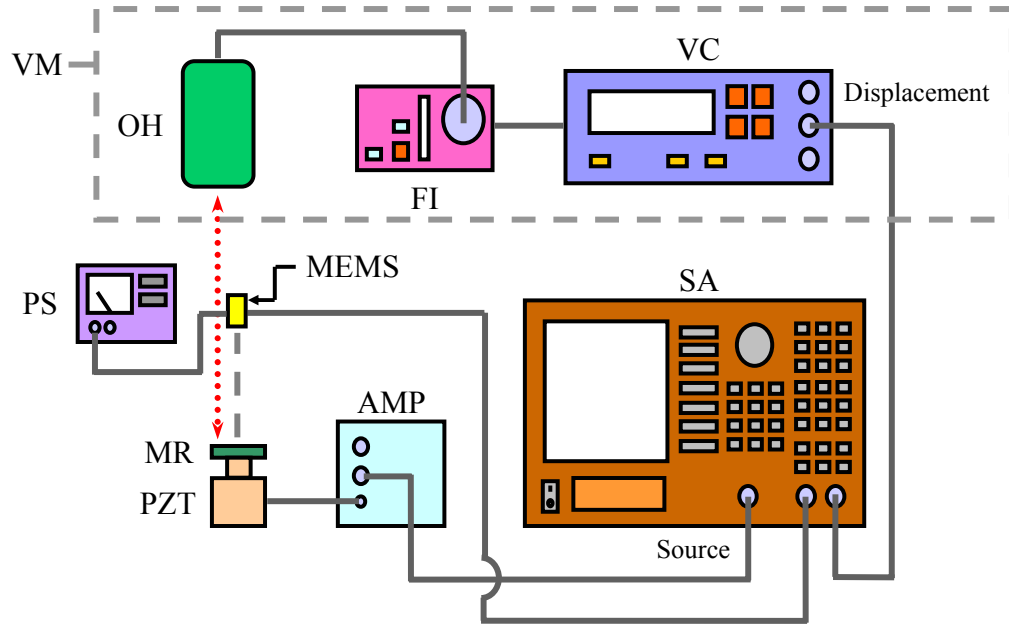


Fig. 3.11. Schematic diagram of the experimental setup used to characterize the frequency responses of MEMS accelerometers.

3.3.1.1. Laser vibrometer

A Laser vibrometer is a noninvasive and noncontact optoelectronic system for measuring dynamic characteristics of objects. The laser vibrometer system used in this thesis is based on a Mach-Zehnder interferometer (Polytec PI, 1994). This system allows measurements of displacements much smaller than the wavelength of light by exploiting the sinusoidal relationship between the output of an interferometer and the difference in optical path length traveled by its beams. By allowing the motion of the surface of interest to modulate the path length traveled by the laser beam, the interferometer can be used to detect vibrational signals with subnanometer measuring resolution (Furlong and Pryputniewicz, 1995; Polytec PI, 1994). Quantitative determination of motions using a

laser vibrometer is achieved by extracting the time dependent optical phase difference, $\Delta\theta(t)$, introduced by the MR, from the detected intensity, $I(t)$, and is given by (Furlong, 1999)

$$I(t) = \frac{1}{2} I_o \{1 + \cos[2\pi f_B + \Delta\theta(t)]\} \quad (3.12)$$

where I_o is the magnitude of the detected intensity and f_B is a known frequency shift introduced by a Bragg cell modulator mounted in one of the beams of the interferometer. The time dependent optical phase difference, $\Delta\theta(t)$, is given by

$$\Delta\theta(t) = \frac{2\pi}{\lambda} \cdot 2L(t) \quad (3.13)$$

where $L(t)$ is the distance traveled by the MR, and is related to its velocity, v_{MR} , and to the induced Doppler frequency shift, f_D , and is given by

$$\Delta\theta(t) = \frac{2\pi}{\lambda} \cdot 2L(t) = \frac{2\pi}{\lambda} \cdot 2v_{MR} \cdot t = 2\pi \cdot f_D \cdot t \quad (3.14)$$

Equations 3.13 and 3.14 indicate that displacements and velocities of an object, as a function of time, can be obtained with laser vibrometer measurements.

3.3.1.2. Low pass filter circuit

The MEMS accelerometer that was used requires decoupling of its output signal from the implicit signal noise generated by the power supply. Figure 3.12 shows the block diagram of the low-pass filter circuit utilized for decoupling and for reducing high-frequency noise from the analog and digital output signals of the MEMS accelerometer.

Decoupling is accomplished by placing a $0.1 \mu\text{F}$ capacitor between the power source and the ground terminal (COM). Also, a $1 \text{ M}\Omega$ resistor is required for setting the duty cycle of the digital output modulated signal. In addition, a $0.001 \mu\text{F}$ capacitor is utilized to define a frequency bandwidth of 5 kHz (Analog Devices, 2001; Analog Devices, 2004).

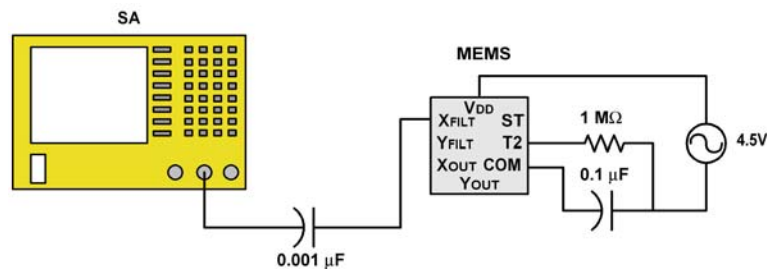


Fig. 3.12. Block diagram of the low-pass filter circuit used to interface the ADXL202 accelerometer.

3.3.2. Experimental results

MEMS accelerometers were excited by simple harmonic, random noise, and sweep sinusoidal functions. Different frequency spans, varying from 10 Hz to 12.9 kHz , were considered to investigate the measuring range and applicability of the MEMS accelerometers. A voltage of 4.5 V was utilized to drive the MEMS accelerometers in all of the experiments (Kok et al. 2003a, 2003b).

3.3.2.1. Determination of frequency response

Experiments were conducted to verify the functionality of the MEMS accelerometers and to observe their response to input excitations. Initial experiments

consisted of exciting the MEMS accelerometer with simple harmonic motions using forcing functions characterized by an amplitude of 25 mV, which corresponds to a displacement amplitude of 0.820 nm, and frequencies ranging from 1 kHz to 12 kHz using 0.5 kHz intervals. The MEMS accelerometers were excited along both of their sensitivity axes. Power spectra from both, the MEMS accelerometers and the laser vibrometer were recorded and compared. Figure 3.13 shows representative results obtained with a MEMS accelerometer and the laser vibrometer corresponding to a forcing function characterized by 2 kHz and 13.2 mg ($g = 9.81 \text{ m/s}^2$).

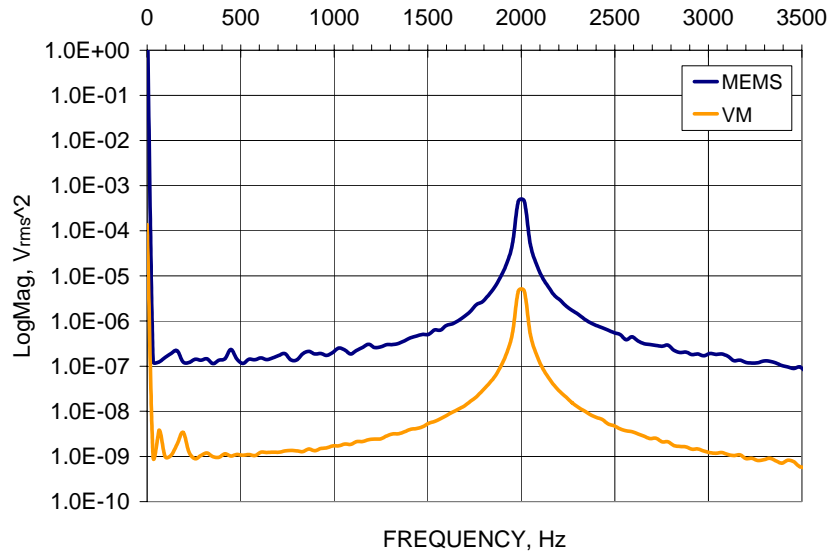


Fig. 3.13. Power spectra measured with both, a MEMS accelerometer and a laser vibrometer (VM). The power spectra correspond to the response of a harmonic characterized by the frequency of 2 kHz at

Using the results obtained in Fig. 3.13, Fig. 3.14 shows ratio of the MEMS and the vibrometer measurements. Results indicate excellent agreement between the two

measurements, which demonstrates that the MEMS accelerometers have high measuring accuracy while having high sensitivity to low amplitude excitations. The offset observed in Fig. 3.13 is due to different electronic gains implicit in the instrumentation used.

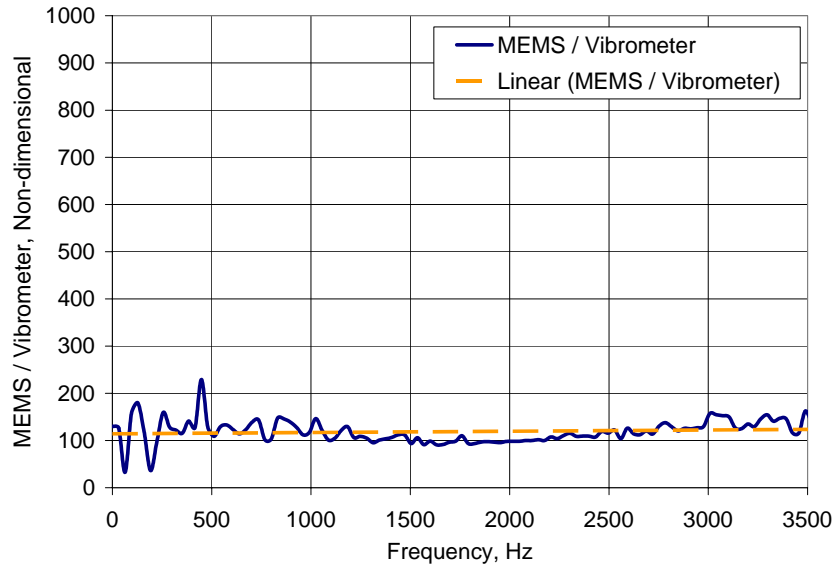


Fig. 3.14. Ratio of the power spectra of the MEMS accelerometer and the laser vibrometer, based on the results in Fig. 3.13.

Real structures are not usually subjected to harmonic excitations, but rather to excitation functions containing a wide spectrum of frequencies and amplitudes. In order to verify the frequency response of MEMS accelerometers to a generic loading situation, experiments were performed by exciting the MEMS accelerometers with random noise containing all frequencies of within specific frequency spans. Figure 3.15 shows representative power spectra obtained with a MEMS accelerometer and a laser vibrometer, corresponding to a random noise forcing function containing frequencies in the [0 - 12.8] kHz range and accelerations in the [0 - 0.135] g ($g = 9.81 \text{ m/s}^2$) range.

Results indicate excellent agreement between the two measurements. The offset observed in Fig. 3.15 is due to different electronic gains implicit in the instrumentation used. The power spectra shown in Fig. 3.15 indicate fundamental harmonics occurring at 8.26, 8.93, and 10.24 kHz. It is suspected that one of these frequencies corresponds to the fundamental natural frequency of the proof mass of the MEMS accelerometer, as determined by the FEM predictions described in Section 3.2.

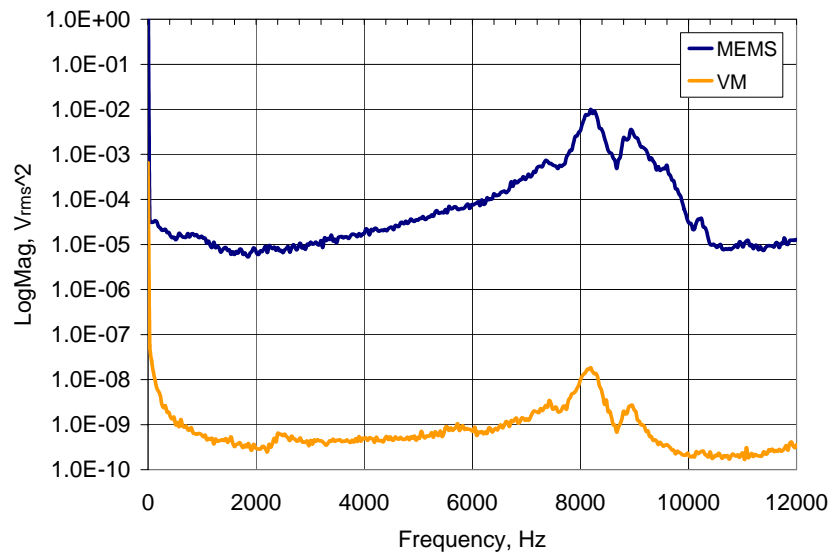


Fig. 3.15. Power spectra measured with both, a MEMS accelerometer and a laser vibrometer. The power spectra correspond to the response of a random excitation containing frequencies in the [0 - 12.8] kHz range and accelerations in the [0 - 0.135] g range.

4. DEVELOPMENT OF WIRELESS DATA ACQUISITION SYSTEMS

In order to transfer signals from MEMS sensors to a signal analyzer, traditional wiring methods can be utilized. Such methods provide reliable data transfer and are simple to integrate for short distance monitoring. However, to perform modal analysis of complex structures, multiple sensors are required to be attached to different locations on the structure. In such cases, wiring and integration of multiple MEMS sensors might become complicated and monitoring of structures across long distances becomes limited. Therefore, there is a need for incorporating wireless capabilities into MEMS sensors (Lynch, 2004; Kok et al., 2003a, 2003b, 2003c).

Two wireless data acquisition systems were developed and their performances were characterized. Both wireless systems operate using RF technology. The first system is designed to transmit the analog output signals, while the second system is designed to transmit digital output signals of MEMS inertial sensors.

4.1. Analog wireless data acquisition system

A prototype analog wireless system was developed to transmit the analog output signals of MEMS inertial sensors. Major criteria for selecting the RF components include small size, light weight, high data transfer rates, and frequency bandwidth compatible with the frequency response function (FRF) of the MEMS accelerometer. To verify the reliability of transmission of data, the prototype system uses a single transmitter and a single receiver.

Commercially available RF components were utilized in the development of the system. The selected RF transmitter and receiver operate with an adjustable carrier frequency of 902 – 908 MHz. They have a data rate of 50 kbps and a flat frequency response function between 50 Hz – 25 kHz. Both transmitter and receiver are powered by a 9 Vdc source. The transmitter has dimensions of $1.25 \times 0.75 \times 0.26$ in³ and the receiver has dimensions of $1.89 \times 0.85 \times 0.35$ in³. Major characteristics of the analog wireless components are summarized in Table 4.1 (LINX, 1999a, 1999b, 2001, 2003).

Table 4.1. Pertinent characteristics of the analog wireless data acquisition system used in the developments (LINX, 1999a, 1999b).

Data rate	Frequency response	Operating frequency
50 kbps	50 Hz - 25 kHz	902 - 908 MHz
Input voltage (transmitter)	Operating voltage (Vcc)	Operating range
-0.3 V - Vcc	2.7 to 16 V	300 m

An RF evaluation kit was utilized to develop the analog wireless system. This kit integrates the driving electronics for the transmitter and the receiver. The on-board switches allow selection of carrier frequency to avoid interference with other wireless devices. Also, the antenna is built-in on the board to ensure reliable data communications (LINX, 1999a, 1999b, 2001). Figure 4.1 shows the analog transmitter and receiver systems.

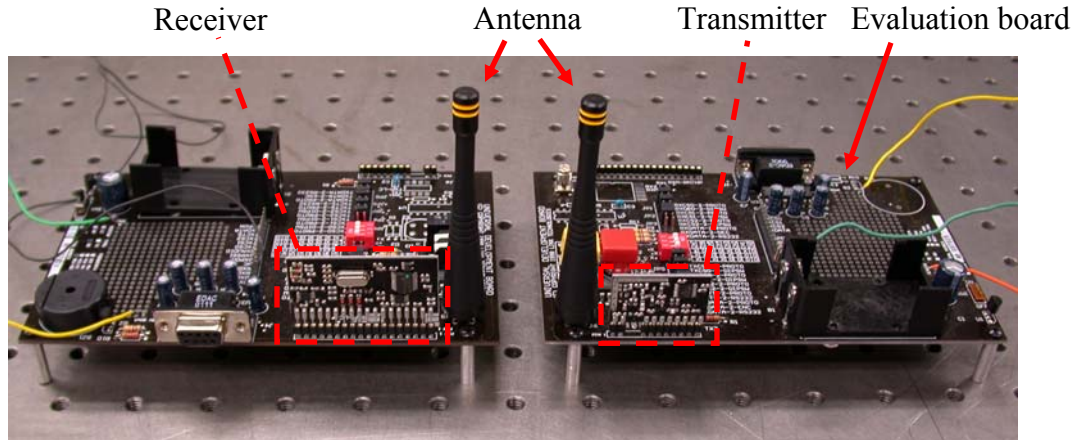


Fig. 4.1. RF transmitter, receiver, and evaluation board used in the development of the analog wireless MEMS inertial system (LINX, 1999a, 1999b).

4.1.1. National Instruments data acquisition system

Virtual instrumentation from National Instruments (NI) was utilized to perform analog signal conditioning and data acquisition, (NI, 2003a). Advantages of using the NI modules include the ability to perform simultaneous signal conditioning of multiple sensors, high flexibility of setup, capabilities to control multiple devices, and small footprints compared to typical signal analyzers.

The hardware utilized includes a SCXI-1530 with a four channels accelerometer amplifier module, a SCXI-1000 chassis, and a PCI-6052E DAQ device (NI 1999a, 2000, 2003b). The SCXI-1530 module is capable to perform simultaneous sampling or multiplexing of analog signals from four channels. It can also generate output signals in a range of ± 10 V (NI, 2000).

The SCXI-1000 is a low noise chassis used to house, power, and control the SCXI modules. The chassis can incorporate up to four SCXI modules and it includes the

control electronics to interface input and output signals from the SCXI modules. The SCXI-1000 is connected to a compatible DAQ card to perform data acquisition (NI, 2003b). Specifically, the PCI-6052E DAQ board was utilized to communicate with the SCXI chassis (NI, 1999a). The DAQ board has sixteen analog inputs and two analog outputs at 333 kS/s with a 16-bit digital resolution. It has an input range of 0.05 V – 10 V, and an output range of ± 10 V, respectively (NI, 1999a). Figure 4.2 shows the NI SCXI modules that were utilized.

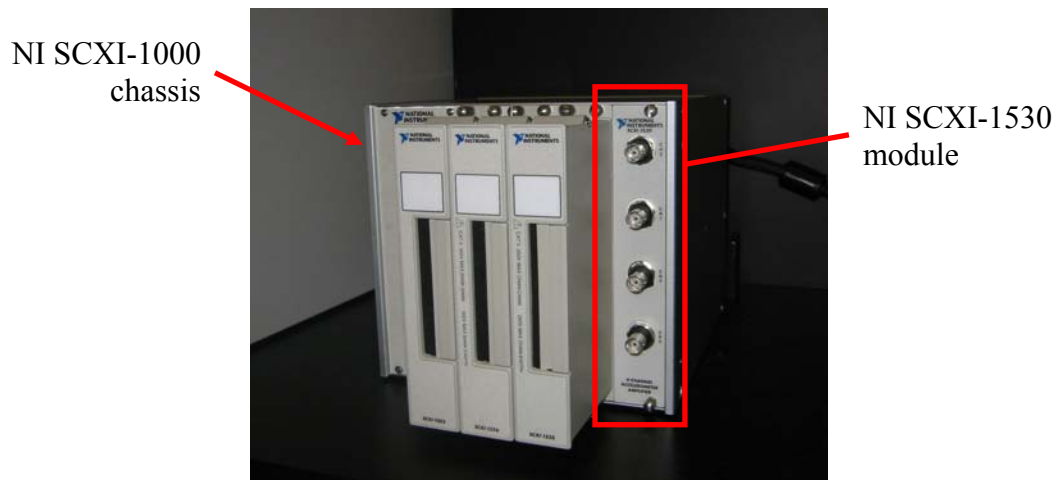


Fig. 4.2. NI SCXI-1530 accelerometer amplifier module, assembled to the SCXI-1000 chassis, used in the development and characterization of the analog wireless MEMS inertial system.

National Instruments LabVIEW is a graphical program environment used to program and control the NI hardware. LabVIEW programs are called virtual instruments (VIs). VIs are composed of two panels, the front panel and the block diagram. The front panel serves as the graphical user interface containing the user inputs and displays of the

output. The block diagram is the interface where the graphical source code is developed. By wiring the corresponding terminals to functions during application development, it is possible to perform the required tasks (NI, 1999b; Bitter et al., 2000). Figures 4.3 and 4.4 show the interface of the front panel and the block diagram, respectively, of the VI developed to perform spectrum analysis with four simultaneous analog inputs. The developed VI is capable to export and save data into an Excel spread sheet for both, time and frequency domains. Appendices A and B contain the front panel and the block diagram of the developed VI.

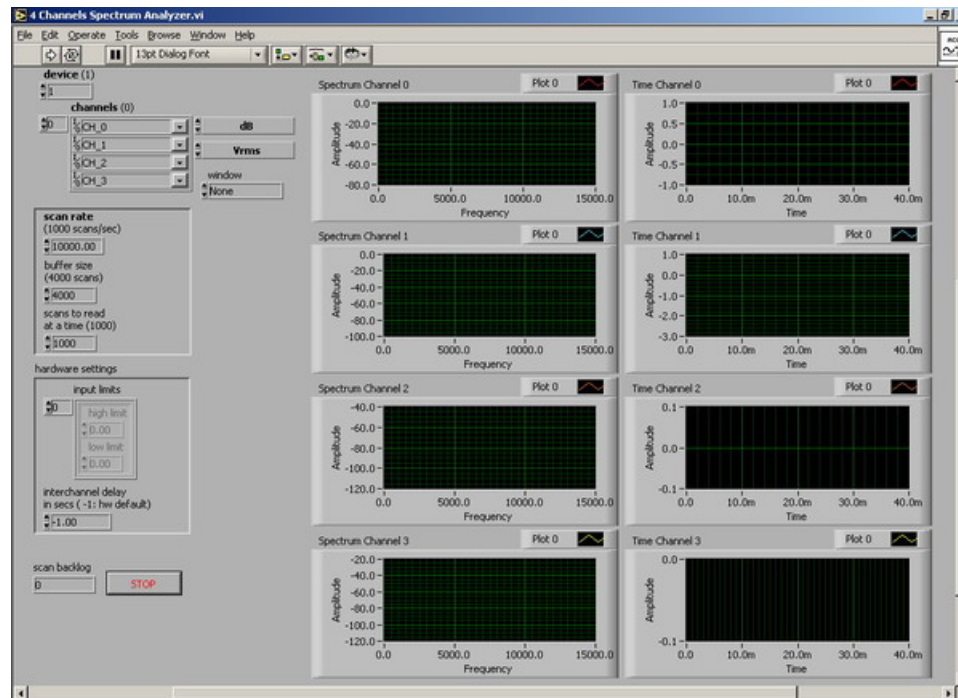


Fig. 4.3. Snapshot of the developed LabVIEW VI for a four channels spectrum analyzer.

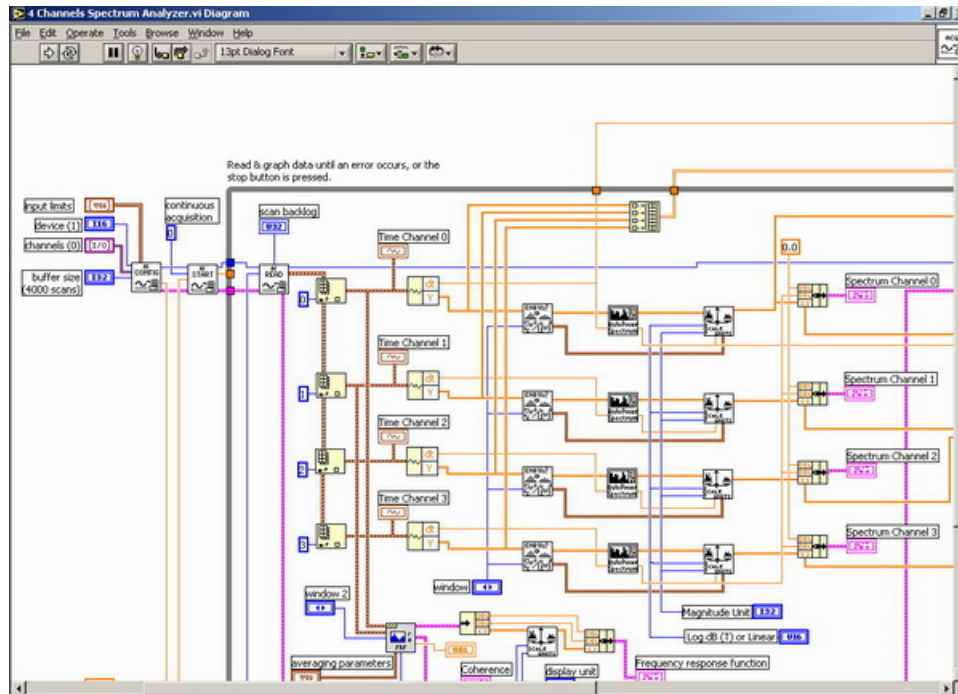


Fig. 4.4 Snapshot of the block diagram of the LabVIEW VI shown in Fig. 4.3.

4.1.2. Experimental characterization of the analog wireless data acquisition system

An experimental setup was developed to characterize the analog wireless data acquisition system. Experiments were performed for two purposes: (1) to verify functionality of the system and, (2) to characterize the frequency response function of the analog wireless system.

The experimental setup consists of a signal generator, the analog wireless system, and the NI data acquisition system. The function generator was used to provide a reliable signal to be transmitted wirelessly. Output of the signal generator was split into two outputs: one output was connected to the input of the transmitter for wireless

transmission, and the second output was connected to the SCXI-1530. Such a configuration allows comparison and verification of the signals. The output of the wireless receiver, in turn, was connected to the second channel of the SCXI-1530 module. Figure 4.5 shows a schematic of the experimental setup that was implemented to characterize the analog wireless system.

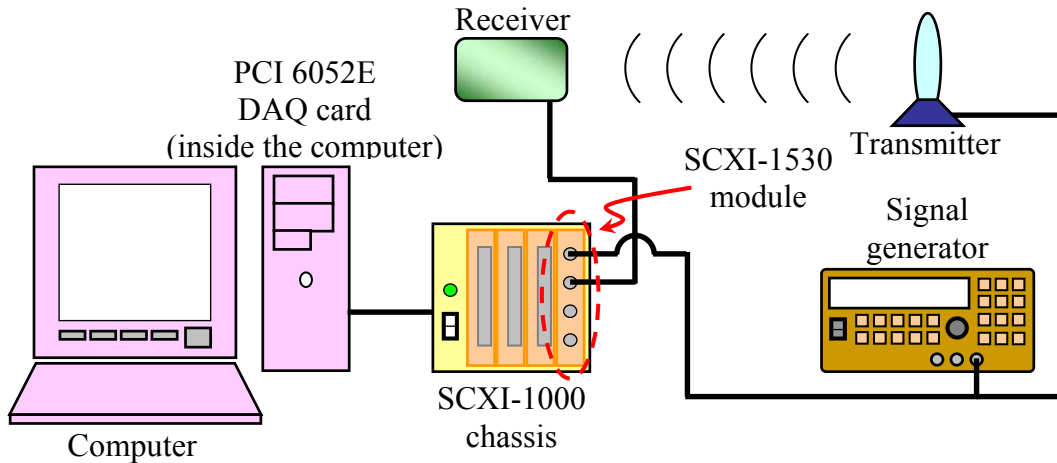


Fig. 4.5. Schematic diagram of the experimental setup used to characterize the analog wireless system.

In order to characterize the frequency response of the wireless data acquisition system, FRF and coherence functions of the wireless system were determined. By using the function generator, both simple harmonic and random functions were utilized. In addition, different frequency spans and amplitudes were used in the experiments. Representative results are shown in Figs 4.6 and 4.7, which demonstrate that the wireless data acquisition system has a linear frequency response from 400 Hz to 16 kHz. These results indicate that the prototype wireless data acquisition system is suitable for use with

the MEMS accelerometers because the FRF of the wireless system encloses the FRF range of the accelerometer (Kok et al., 2003c).

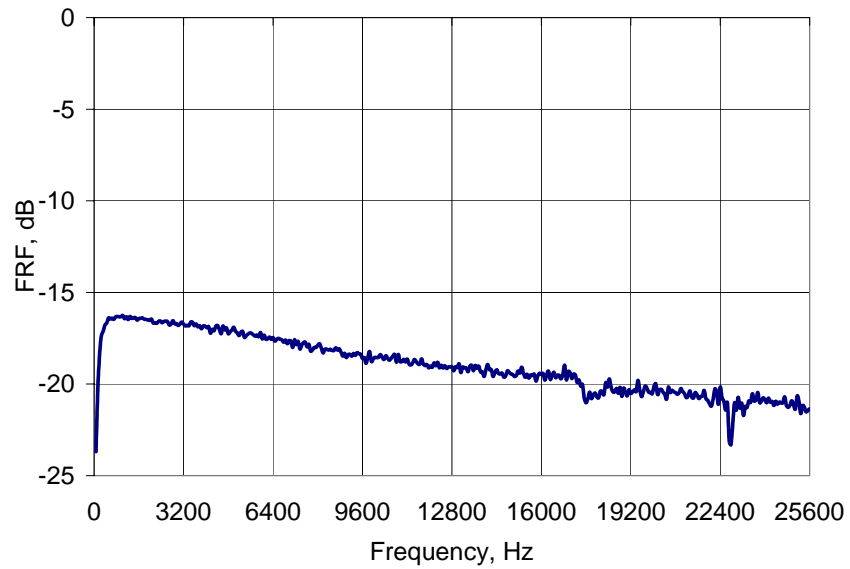


Fig. 4.6. Frequency response function of the analog wireless data acquisition system.

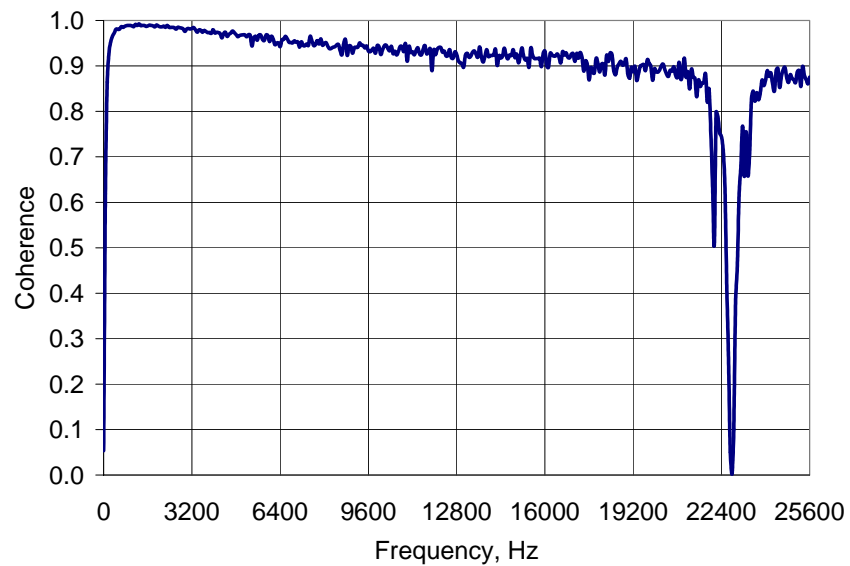


Fig. 4.7. Coherence function of the analog wireless data acquisition system.

4.2. Digital wireless data acquisition system

A digital wireless system, developed using a microcontroller, was used to transmit digital output signals of MEMS inertial sensors. The selected microcontroller has been widely utilized in different engineering applications (Parallax, 2004; Lindsay, 2003a; Kok et al., 2004a, 2004b, 2004c).

The microcontroller is surface-mounted to a 3" × 4" printed circuit board and it has a processing speed of 20 MHz and a program execution speed of approximately 4,000 instructions/sec. The microcontroller board is powered by a 9 Vdc source. On the board, there is a regulator that provides 50 mA of current and 5 V of power to a prototype area. A DB-9 connector is available to provide serial communications with a computer. This microcontroller is programmable through specific language (Parallax, 2004). Figure 4.8 shows the microcontroller board, and Table 4.2 summarizes pertinent characteristics of the microcontroller (Lindsay, 2003a; Parallax, 2004a, Kok et al., 2004a, 2004b).



Fig. 4.8. Microcontroller evaluation board utilized in the developments. The surface mount microcontroller package is located at the center of the board (Parallax, 2003a).

Table 4.2. Pertinent characteristics of the microcontroller utilized in the developments. (Parallax, 2003a).

Microcontroller	Processor Speed	Program Execution Speed
Microchip PIC16C57c	20 MHz	~4,000 instruction/sec.
RAM Size	Number of I/O pins	Voltage
36 Bytes	16 + 2 Dedicated serial	5 – 15 Vdc

RF transmitter and receiver units with carrier frequency of 433.92 MHz were utilized to define a wireless data communications link. The transmitter and receiver were manufactured by LINX (LINX, 2003). These RF modules integrate the antenna, data processor, and all the necessary electronics into one package. The on-board encoder and decoder of the modules allow them to be interface with the microcontroller that was selected. Figure 4.9 shows the RF modules used, and Table 4.3 summarizes pertinent characteristics of the modules (Parallax, 2003b; Kok et al., 2004a, 2004b).

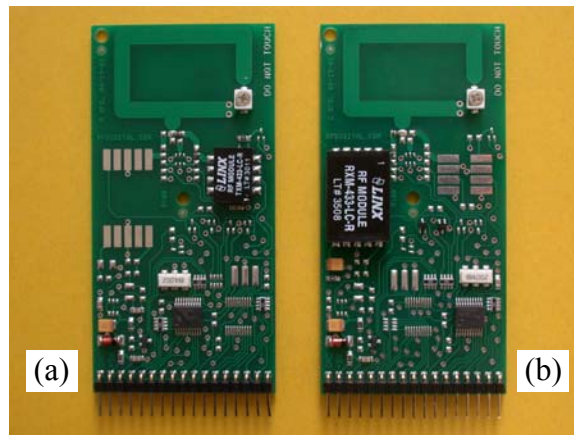


Fig. 4.9. RF modules utilized: (a) transmitter (b) receiver (Parallax, 2003b).

Table 4.3. Pertinent characteristics of the RF components utilized in the developments (Parallax, 2003b).

Carrier frequency	Data rate	Supply voltage	Data range	Operating temperature
433.92 MHz	5,000 bps	5 V	80 m	10°C to 60 °C

4.2.1. Connection of the microcontroller

The microcontroller board is connected to a computer via a DB-9 connector to define serial communications. Serial connection of the board and the computer allows signal communications with the inertial sensors. Figure 4.10 shows the connection diagram of the microcontroller board with a computer (Lindsay, 2003a).

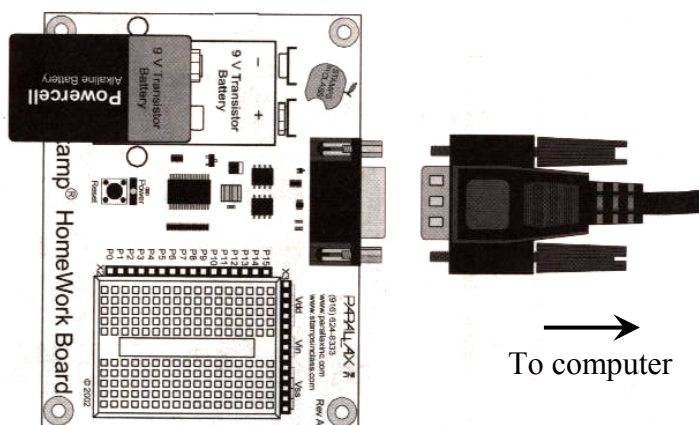


Fig. 4.10. Schematic showing connection of the microcontroller board to a computer (Lindsay, 2003a).

The digital wireless system is defined by a transmitter and a receiver microcontroller unit. The transmitter unit consists of the accelerometer, RF transmitter, and the microcontroller board. The accelerometer, with the corresponded signal conditioning circuitry, is connected to the microcontroller board. Pin 3 and Pin 8 of the accelerometer are connected to the Vss and the Vdd pins to obtain 5 V from the board. Digital output pins of the accelerometer, Pin 4 (y_{out}) and Pin 5 (x_{out}), are connected to the P9 and the P8 of the board, respectively. For the wireless transmitter module, Pins 2 and 3 (+5VDC and Mode) are connected to Vdd, and Pin 1 (GND) is connected to Vss. Pin 4

of the transmitter (TXD) is connected to P13 on the board to obtain serial data from the microcontroller for wireless transmission. Figure 4.11 shows the block diagram of the transmitter microcontroller unit (Lindsay, 2003a; Kok et al., 2004a, 2004b; Parallax, 2003a, 2003b).

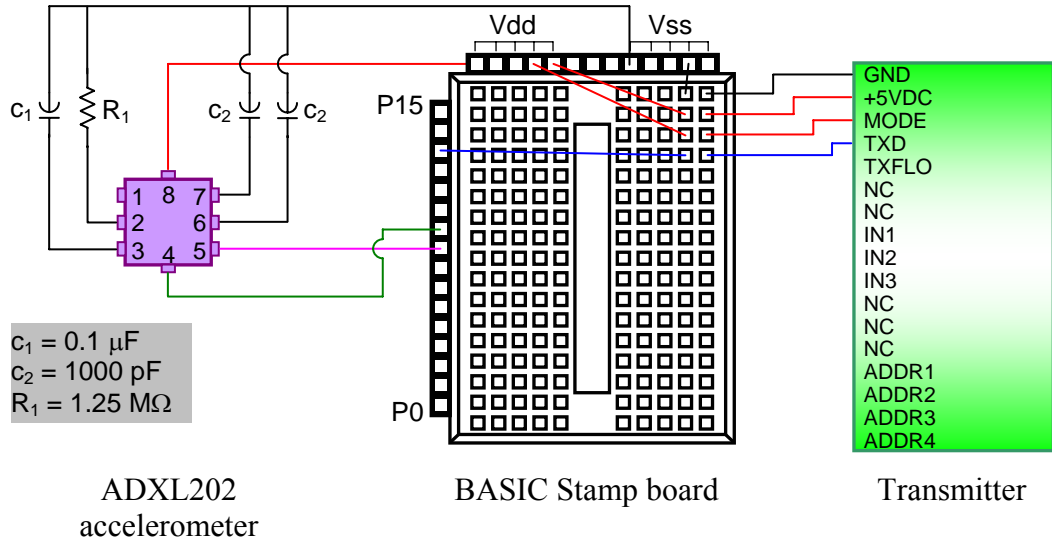


Fig. 4.11. Block diagram showing connections of the transmitter unit.

For the receiver unit, the wireless receiver module was powered by connecting Pin 1 to Vss, and Pin 2 and 3 (+5VDC and Mode) to Vdd of the microcontroller board. Pin 6 (RXD) of the receiver is connected to P4 of the board to send data to the microcontroller. Figure 4.12 shows the block diagrams of the receiver microcontroller unit, while Figs 4.13 and 4.14 show the actual setup of the transmitter and receiver units, respectively (Lindsay, 2003a; Kok et al., 2004a, 2004b; Parallax, 2003a, 2003b).

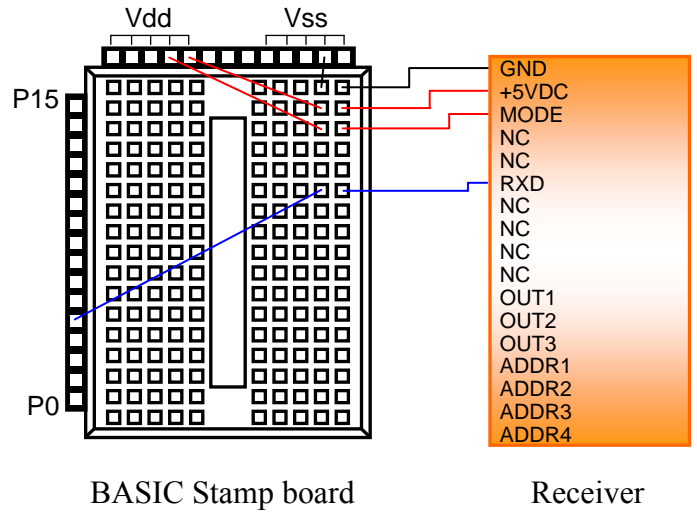


Fig. 4.12. Block diagram showing connections of the receiver unit.

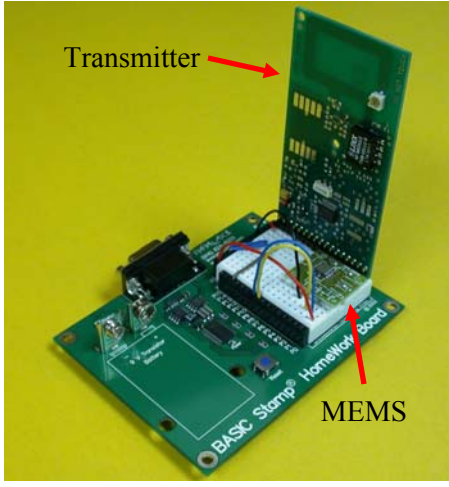


Fig. 4.13. Transmitter unit consists of the microcontroller board, MEMS accelerometer, and the wireless RF module.

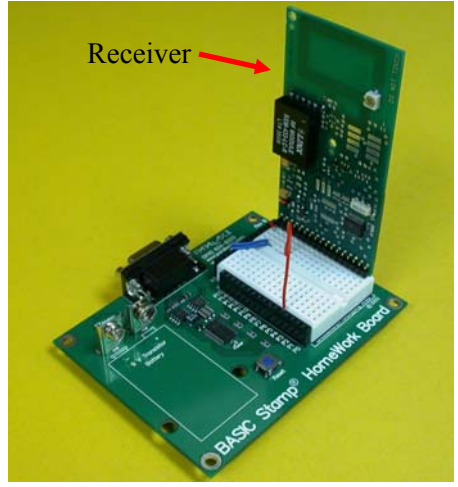


Fig. 4.14. Receiver unit consists of the microcontroller board and the wireless RF module.

4.2.2. Software interface

The microcontroller and the RF modules are designed to be programmable with the PBASIC language (Parallax, 2004). PBASIC version 2.5 was used in the developments. PBASIC programs were written using the BASIC stamp window editor (Lindsay, 2003a, 2003b). A program was developed to perform digital signals processing of MEMS inertial sensors and to control the RF modules (Kok et al. 2004a, 2004b).

Figure 4.15 shows the interface of the BASIC Stamp Window Editor.

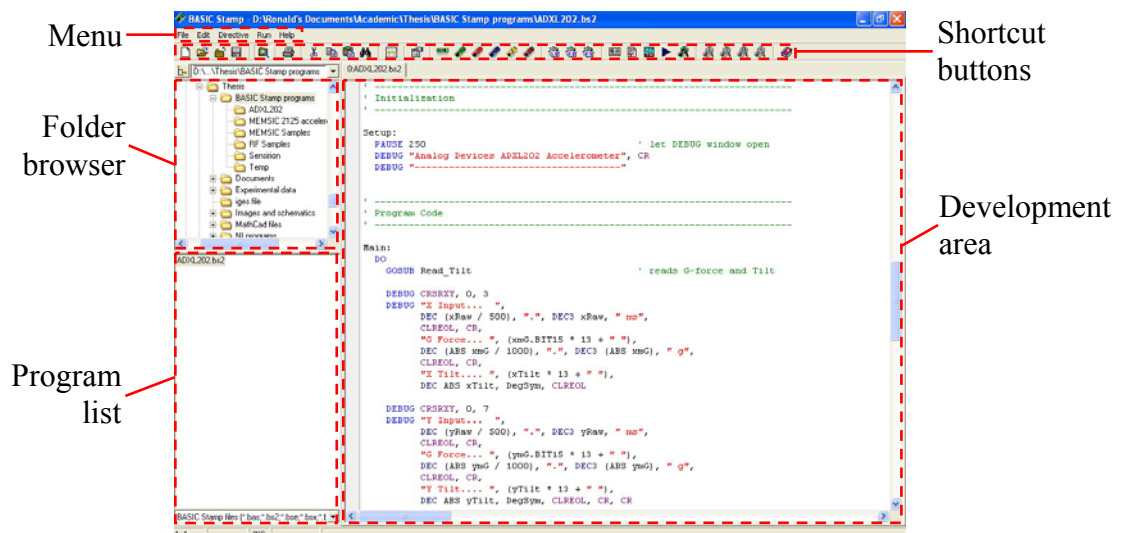


Fig. 4.15. Interface of the BASIC Stamp Window Editor used to program the microcontroller

The interface of the BASIC stamp window editor is divided into three major sections: folder browser, program list, and development area. The first two sections allow easy allocation of existing programs and workspaces. The development area is the core of the editor, which is utilized to develop the program.

4.2.3. Construction of the program

A PBASIC program is constructed by defining three major portions: definition of the microcontroller, definition of the variables, and definition of the control code. In order to successfully download the program to the microcontroller, the header of the code needs to specify the type of microcontroller module utilized. For a BS2 microcontroller programmed with the PBASIC 2.5 version, the microcontroller definition:

```
' {$STAMP BS2}  
' {$PBASIC 2.5}
```

is added at the beginning of the code. The next portion of the program defines the variables used in the program. Variables size can be defined as bit (0 and 1), nib (0 to 15), byte (0 to 255), and word (0 to 65535), depending on the size that is required. It is possible to define as many variables as needed in the program. However, the sum of the allocated variables at a given time is limited to 26 bytes due to the available memory on the microcontroller. The last portion of the program is the control code, which contains all the commands, subroutines, and algorithms that are necessary to perform specific operations. (Parallax, 2004; Parallax, 2003a; Lindsay, 2003b).

Before downloading and using, the program needs to be compiled. This is done by selecting *Run* → *Check Syntax*, from the menu. If the program is executable, *Tokenize successful* will be displayed at the lower left corner of the program area. If there are problems in the program, an error message will be returned with the description of the problems. Common errors might be caused by loose connections of serial cables, incorrect definition of BASIC Stamp module, undefined variables, and typographical errors in the control code. Once the program has been successfully compiled, it is

downloaded to the EEPROM of the microcontroller for permanent storage. The program can be downloaded by selecting *Run* → *Run*, from the menu or by selecting the shortcut button (Parallax, 2003a; Lindsay, 2003a, 2003b).

5. APPLICATIONS

Three representative applications were realized to demonstrate applicability of the developed wireless MEMS inertial systems to perform health monitoring of structures. The first application involved modal analysis of a cantilever using MEMS accelerometers. In this application, a cantilever was characterized by using analytical, computational, and experimental methodologies. The results indicated that attaching MEMS accelerometers introduce minimal, but measurable effects to the dynamic characteristics of the cantilever. The second application involved utilization of the MEMS accelerometers and the digital wireless system to perform high resolution tilt and rotation measurements of an object subjected to linear acceleration. This application illustrates the calibration procedures for the developed digital wireless MEMS inertial system. The third application involved utilization of a MEMS gyroscope and the digital wireless system to perform angular rate measurements. A proof of concept analog to digital conversion circuit was built, and the results indicate feasibility of performing wireless angular rate measurements of structures.

5.1. Modal analysis of a cantilever

Some of the advantages of using MEMS accelerometers are their small footprint and light weight, which introduce minimal effects to the dynamic characteristics of the structures being tested. A cantilever was utilized as the test structure to verify the applicability of MEMS accelerometers to modal analysis.

Modal analysis of the test cantilever was performed using analytical, computational, and experimental methods, to determine the effects of attaching MEMS accelerometers in the dynamic characteristics of the cantilever. Analysis was performed based on two approaches: the first approach involved solving the equation of motion of a beam in bending to determine the mode shapes and the corresponding natural frequencies. The second approach involved applying the Rayleigh's energy method to determine the fundamental natural frequency of the cantilever, with and without MEMS accelerometers attached. A computation model of the cantilever was created and its modes of vibration and corresponding natural frequency were determined based on the finite element method (FEM). Experimental analysis was performed based on of noninvasive, full-field-of-view, optoelectronic holography (OEH) to determine the modal characteristics of the cantilever. In addition, the analog wireless system was utilized with the MEMS accelerometers to study the natural frequency and to reconstruct the mode shapes of the cantilever.

The cantilever that was investigated is made of aluminum alloy (AL7075-T6), with dimensions of $16.3 \times 3.8 \times 0.9 \text{ cm}^3$. The base of the cantilever has dimensions of $5.08 \times 5.08 \times 5.08 \text{ cm}^3$. The base was machined out of a single piece of aluminum to allow the cantilever to be rigidly attached to a piezoelectric shaker (PZT). The entire beam has a mass of 456.8 gr, and a mass density of 2571.314 kg/m^3 . Figure 5.1 shows the experimental setup, which consists of the cantilever and the PZT shaker.

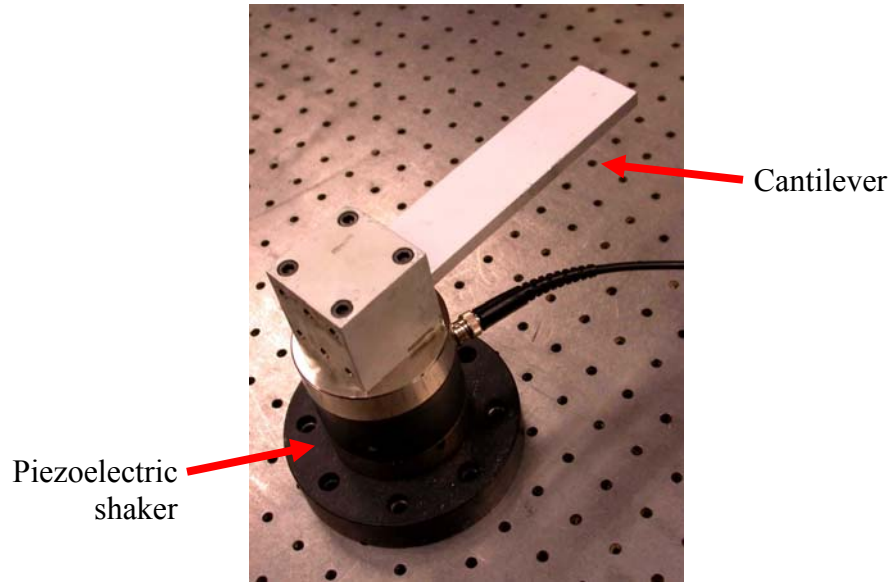


Fig. 5.1. Experimental setup to perform modal analysis of a cantilever.

5.1.1. Analytical considerations

Analytical methods were applied to calculate the natural frequencies and the mode shapes of the cantilever. In order to define and solve the governing equation, a simply supported beam that carries a distributed load, was considered and is shown in Fig. 5.2 (Paz, 1991; Volterra and Zachmanoglou, 1965; Hibbeler, 1997; Rao, 1995).

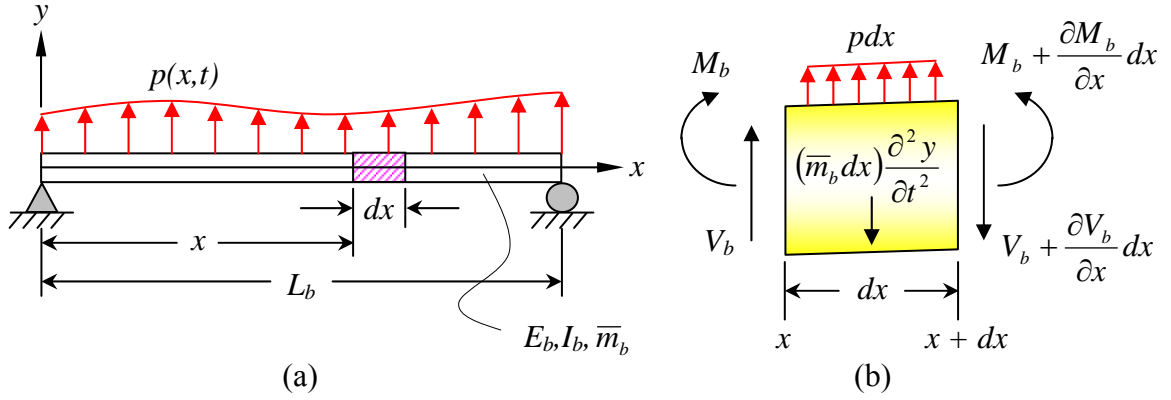


Fig. 5.2. Beam subjected to a distributed load: (a) simply supported beam with distributed load $p(x,t)$ and, (b) free body diagram of a beam element of length dx .

In Fig. 5.2 (a), L_b , I_b , \bar{m}_b , and E_b , represents the length, the area moment of inertia, the mass per unit length of the beam, and the modulus of elasticity of the material of the beam, respectively. The term $p(x,t)$ represents the distributed load along the beam. In Fig. 5.2 (b), V_b and $V_b + (\partial V_b / \partial x)dx$ are shear forces, while M_b and $M_b + (\partial M_b / \partial x)dx$ are bending moments of the beam element, dx . For the beam element, the equilibrium of the lateral forces can be written as (Paz, 1991; Volterra and Zachmanoglou, 1965; Hibbeler, 1997; Rao, 1995)

$$V_b - \left(V_b + \frac{\partial V_b}{\partial x} dx \right) + p(x,t)dx - \bar{m}_b dx \frac{\partial^2 y}{\partial t^2} = 0$$

$$\text{or } p(x,t) = \frac{\partial V_b}{\partial x} dx + \bar{m}_b \frac{\partial^2 y}{\partial t^2} , \quad (5.1)$$

and the equilibrium of the bending moments can be written as

$$M_b - \left(M_b + \frac{\partial M_b}{\partial x} dx \right) + V_b dx = 0 \quad \text{or } V_b = \frac{\partial M_b}{\partial x} . \quad (5.2)$$

Since the beam deforms by the internal moment, M_b , the radius of curvature, R , needs to be taken into account. R is defined by (Hibbeler, 1997)

$$\frac{1}{R} = \frac{M_b}{E_b I_b} \quad . \quad (5.3)$$

With the elastic curve of the beam defined as $y = y(x)$, the relation between the radius of curvature and the elastic curve of the beam is (Anton, 1995; Hibbeler, 1997)

$$\frac{1}{R} = \frac{\frac{\partial^2 y}{\partial x^2}}{\left[1 + \left(\frac{\partial y}{\partial x}\right)^2\right]^{\frac{3}{2}}} \quad . \quad (5.4)$$

Substitution of Eq. 5.3 into 5.4 yields

$$\frac{\frac{\partial^2 y}{\partial x^2}}{\left[1 + \left(\frac{\partial y}{\partial x}\right)^2\right]^{\frac{3}{2}}} = \frac{M_b}{E_b I_b} \quad . \quad (5.5)$$

Since the deformation of the beam is small, the term $(\partial y / \partial x)^2$ can be neglected.

Therefore, Eq. 5.5 can be rewritten as

$$M_b = E_b I_b \frac{\partial^2 y}{\partial x^2} \quad , \quad (5.6)$$

while Eqs 5.1 and 5.2 can be written as

$$p(x, t) = E_b I_b \frac{\partial^4 y}{\partial x^4} + \bar{m}_b \frac{\partial^2 y}{\partial t^2} \quad , \quad (5.7)$$

and

$$V_b = E_b I_b \frac{\partial^3 y}{\partial x^3} , \quad (5.8)$$

respectively.

When the distributed load is removed, the beam will return to its initial position and inertia will cause the beam to vibrate. Therefore, the equation for free vibrations is defined as (Paz, 1991; Volterra and Zachmanoglou, 1965; Rao, 1995)

$$E_b I_b \frac{\partial^4 y}{\partial x^4} + \bar{m}_b \frac{\partial^2 y}{\partial t^2} = 0 . \quad (5.9)$$

Equation 5.9 can be solved by the method of separation of variables. This method assumes that the solution can be expressed into two functions: (1) function of position, $\Psi(x)$, and (2) function of time, $f(t)$, as (O'Neil, 1991; Paz, 1991; Volterra and Zachmanoglou, 1965; Rao, 1995)

$$y(x, t) = \Psi(x)f(t) . \quad (5.10)$$

By substituting Eq. 5.10 into 5.9, it is obtained

$$E_b I_b f(t) \frac{\partial^4 \Psi(x)}{\partial x^4} + \bar{m}_b \Psi(x) \frac{\partial^2 f(t)}{\partial t^2} = 0 . \quad (5.11)$$

In order to apply separation of variables to Eq. 5.11, both sides Eq. 5.11 are divided by $\bar{m}_b \Psi(x)f(t)$

$$\frac{E_b I_b}{\bar{m}_b} \frac{\partial^4 \Psi(x)}{\partial x^4} = - \frac{1}{f(t)} \frac{\partial^2 f(t)}{\partial t^2} , \quad (5.12)$$

which indicates that both sides must be equal to the same constant. Assuming that the constant is $\omega_{n_beam}^2$, the left hand side of Eq. 5.12 can be written as

$$\frac{E_b I_b}{\bar{m}_b} \frac{\partial^4 \Psi(x)}{\partial x^4} = \omega_{n_beam}^2 \quad \rightarrow \quad \partial^4 \Psi(x) - \kappa^4 \partial x^4 = 0 \quad , \quad (5.13)$$

with

$$\kappa^4 = \frac{\bar{m}_b \omega_{n_beam}^2}{E_b I_b} \quad , \quad (5.14)$$

and the right hand side of the Eq. 5.12 can be written as

$$-\frac{1}{f(t)} \frac{\partial^2 f(t)}{\partial t^2} = \omega_{n_beam}^2 \quad \rightarrow \quad \frac{\partial^2 f(t)}{\partial t^2} + \omega_{n_beam}^2 f(t) = 0 \quad . \quad (5.15)$$

Equation 5.14 can be rewritten in terms of ω_{n_beam} as

$$\omega_{n_beam} = (\kappa L_b)^2 \sqrt{\frac{E_b I_b}{\bar{m}_b L_b^4}} \quad . \quad (5.16)$$

The general solution of Eq. 5.13 is a linear combination of $\sin \kappa x$, $\cos \kappa x$, $\sinh \kappa x$, and $\cosh \kappa x$, given as (O'Neil, 1991; Paz, 1991; Volterra and Zachmanoglou, 1965; Rao, 1995), viz.,

$$\Psi(x) = B_1 \sin \kappa x + B_2 \cos \kappa x + B_3 \sinh \kappa x + B_4 \cosh \kappa x \quad , \quad (5.17)$$

with B_1, B_2, B_3, B_4 , being constants of integration that depend on the applied boundary conditions. Equation 5.17 represents the mode shapes of vibration of a beam. For cantilever boundary conditions, there are no deflections at the fixed end (i.e., $x = 0$) of the beam and the slope is zero. At the free end of the cantilever (i.e., $x = L_b$), there are no bending moments and no shear forces. The following equations summarize the boundary conditions of the cantilever (Paz, 1991; Volterra and Zachmanoglou, 1965; Rao, 1995)

At $x = 0$,

$$\Psi(0) = 0 \quad ; \quad \dot{\Psi}(0) = 0 \quad . \quad (5.18)$$

At $x = L_b$,

$$\ddot{\Psi}(L_b) = 0 \quad ; \quad \ddot{\Psi}(L_b) = 0 \quad . \quad (5.19)$$

By applying the boundary conditions given by Eqs 5.18 and 5.19 to Eq. 5.17, the following equation is obtained (Paz, 1991; Volterra and Zachmanoglou, 1965; Rao, 1995)

$$\sinh \kappa_n L_b \cdot \cosh \kappa_n L_b + 1 = 0 \quad , \quad (5.20)$$

where the subscript n represents the number of a mode of vibration. To determine the roots, $\kappa_n L_b$, of Eq. 5.20, numerical methods based on the Newton-Raphson algorithm can be applied (Anton, 1995). Therefore, the natural frequencies for each root of Eq. 5.20 are determined by

$$\omega_{n_beam} = (\kappa_n L_b)^2 \sqrt{\frac{E_b I_b}{\bar{m}_b L_b^4}} \quad , \quad (5.21)$$

and the corresponding mode shapes are determined by

$$\Psi(x) = (\cosh \kappa_n x - \cos \kappa_n x) - \sigma_n (\sinh \kappa_n x - \sin \kappa_n x) \quad , \quad (5.22)$$

with

$$\sigma_n = \frac{\cosh \kappa_n L_b + \cos \kappa_n L_b}{\sinh \kappa_n L_b + \sin \kappa_n L_b} \quad . \quad (5.23)$$

Table 5.1 summarize the roots of Eq. 5.20, including the values of the coefficient, σ_n , for the first three modes of vibrations of a cantilever (Paz, 1991; Volterra and Zachmanoglou, 1965, Rao, 1995).

Table 5.1. The first three roots of Eq. 5.20 and the corresponding constants, σ_n , that define the mode shapes of a cantilever for its first three bending modes of vibration (Paz, 1991; Volterra and Zachmanoglou, 1965, Rao, 1995).

Modes of vibration, n	$(\kappa_n L_b)^2$	σ_n
1	3.5160	0.734096
2	22.0345	1.018466
3	61.6972	0.99225

By applying Eq. 5.21, the first three modes of vibration are calculated to be 283.8 Hz, 1778.5 Hz, and 4980 Hz, respectively. Using Eqs 5.22 and 5.23, the mode shapes of for vibration of the cantilever are calculated and are displayed in Fig. 5.3.

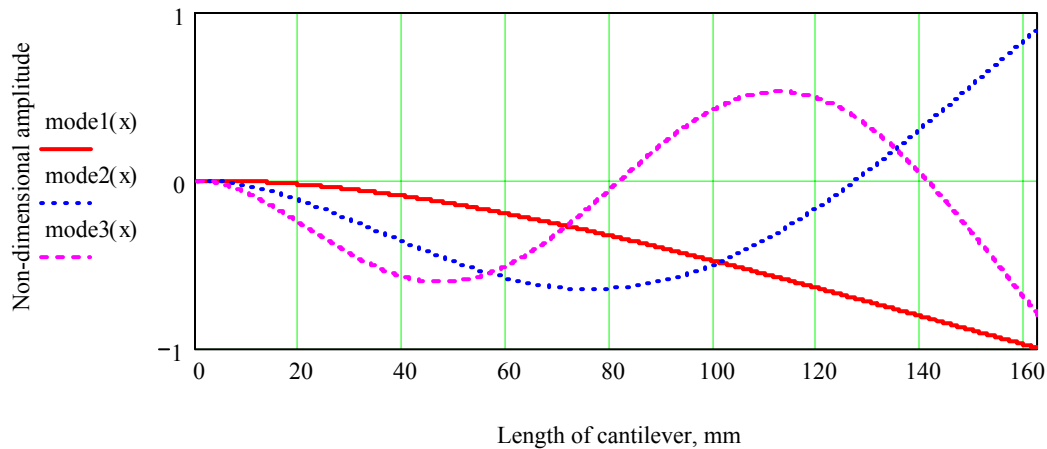


Fig. 5.3. First three bending modes of vibration of the test cantilever.

In order to evaluate the changes in the characteristics of the fundamental natural frequency of the cantilever after attaching MEMS accelerometers, Rayleigh's energy method was utilized. The configuration that was considered consists of a cantilever with a mass, m_{mass} , attached at its free end, as shown in Fig. 5.4. To determine the natural frequency of this configuration using Rayleigh's method, two assumptions were made: (1)

the shape of the deflection curve of the cantilever is equal to the deflection induced by a force, F_{mass} , applied at the free end of the cantilever and, (2) the motion of the cantilever is harmonic and having the form of (Thomson and Dahleh, 1998; Rao, 1995; Paz, 1991)

$$y = \gamma \sin(\omega_b t + \alpha) \quad . \quad (5.24)$$

In Eqs 5.24, y is the deflection of the cantilever at its free end, γ is the maximum amplitude of the harmonic motion, and ω_b and α are the frequency and the phase of the harmonic motion, respectively.

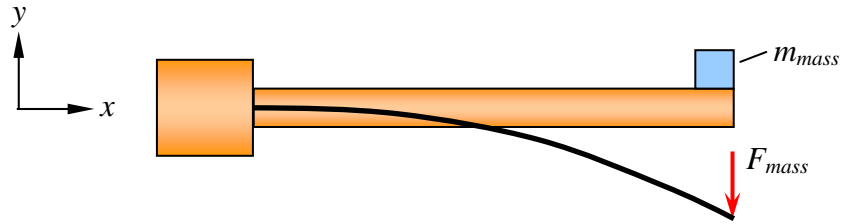


Fig. 5.4. Cantilever with a mass, m_{mass} , attached at its free end and the corresponding deflection curve of the cantilever.

With the concentrated force applied at the free end of the cantilever, the shape function characterizing the deflection of the cantilever, $u(x)$, is defined as (Thomson and Dahleh, 1998; Rao, 1995; Paz, 1991)

$$u(x) = \frac{3y}{L_b^3} \left(\frac{L_b x^2}{2} - \frac{x^3}{6} \right) \quad . \quad (5.25)$$

By substituting Eq. 5.24 into 5.25, it is obtained that

$$u(x) = \frac{3L_b x^2 - x^3}{2L_b^3} \gamma \sin(\omega_b t + \alpha) \quad . \quad (5.26)$$

Equation 5.26 can be used to calculate that maximum kinetic energy of the cantilever, T_{max} , which is defined by the sum of kinetic energy due to the distributed mass of the beam, T_b , and the kinetic energy of the mass at the free end, T_{mass} .

T_b and T_{mass} have the form

$$T_b = \int_0^L \frac{1}{2} \left(\frac{m_b}{L} \right) \dot{u}^2 dx \quad , \quad (5.27)$$

and

$$T_{mass} = \frac{1}{2} m_{mass} \omega_b^2 \gamma^2 \quad , \quad (5.28)$$

where m_b is the mass of the cantilever. Using Eqs 5.26 to 5.28, T_{max} can be determined as

$$T_{max} = \frac{m_b}{L} \int_0^L \left(\frac{3Lx^2 - x^2}{2L^3} \gamma \omega_b \right)^2 dx + \frac{1}{2} m_{mass} \omega_b^2 \gamma^2 \quad . \quad (5.29)$$

Noting that the potential energy of the cantilever is equal to the work done by the concentrated force, the maximum potential energy, V_{max} , can be determined as

$$V_{max} = \frac{1}{2} F_{mass} \gamma = \frac{3E_b I_b}{2L_b^3} \gamma^2 \quad . \quad (5.30)$$

By applying Eqs 5.29 and Eq. 5.30, the fundamental natural frequency of the cantilever with a mass attached at its free end can be determined as

$$\omega_b = \sqrt{\frac{3E_b I_b}{L_b^3 \left[\frac{33}{140} m_b + \frac{1}{2} m_{mass} \right]}} \quad . \quad (5.31)$$

Using Eq. 5.31 and the corresponding material properties of the test beam, the fundamental natural frequency of the cantilever without any additional mass attached was

determined to be 294.8 Hz. Recalling that the MEMS accelerometer utilized has a mass of 160 mgr, and by adding this mass at the free end of the cantilever, the modified natural frequency of the cantilever with the added mass was determined to be 294.4 Hz, which represents a 0.14 % change. This result indicates that MEMS accelerometers have minimal yet measurable effects on the fundamental natural frequencies of the structures being measured, which verifies their applicability to experimental modal analysis.

To investigate modal characteristics of the entire cantilever, multiple MEMS accelerometers may be required, as shown in Fig. 5.5. Further investigations involved the development of analytical solutions of the cantilever with multiple masses attached. The solutions were developed based on the utilization of the Rayleigh's energy method (Paz, 1991; Rao, 1995; Thomson and Dahleh, 1998).

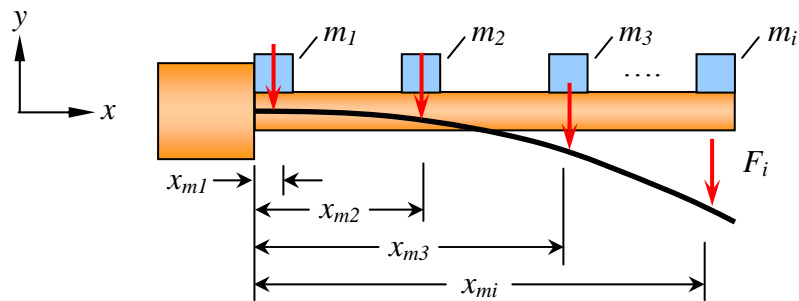


Fig. 5.5. Cantilever with multiple masses, m_1 to m_n , attached to arbitrary locations along the cantilever, and the corresponding deflection curve the cantilever.

Referring to Fig. 5.5, the boundary conditions of the cantilever at the fixed end ($x=0$) and free end ($x=L_b$) are (Paz, 1991; Rao, 1995; Thomson and Dahleh, 1998)

$$\text{At } x = 0 \left\{ \begin{array}{l} y = 0 \\ \dot{y} = 0 \\ \ddot{y} = \frac{M_b}{E_b I_b} \neq 0 \end{array} \right\}, \quad \text{at } x = L_b \left\{ \begin{array}{l} y \neq 0 \\ \dot{y} \neq 0 \\ \ddot{y} = 0 \end{array} \right\}. \quad (5.32)$$

In order to define the frequency equation for such a configuration, a shape function of the deformed cantilever satisfying the boundary conditions described by Eq. 5.32 can be written as

$$y(x) = A \left(1 - \cos \frac{\pi x}{2L_b} \right), \quad (5.33)$$

where A represents amplitude of the deformation. For a cantilever, the maximum deflection occurs at the free end of the beam regardless of the location of the masses, and the maximum deflection, y_{max} , is

$$y_{max} = A \left(1 - \cos \frac{\pi L_b}{2L_b} \right) = A. \quad (5.34)$$

The displacement of the beam where a single mass is located, y_{mi} , can be determined by

$$y_{mi} = A \left(1 - \cos \frac{\pi x_{mi}}{2L_b} \right). \quad (5.35)$$

Similar to Eq. 5.29, the maximum kinetic energy of the system, T_{max} , can be determined by the sum of the kinetic energy of individual masses attached to the cantilever, ΣT_{mass} , and the sum of the kinetic energy due to the distributed mass of the beam, T_b . ΣT_{mass} can therefore, be determined by

$$\sum T_{mass} = \sum_{r=1}^i \frac{1}{2} m_r \left[A \left(1 - \cos \frac{\pi x_{mr} m_r}{2L_b} \right) \omega_b \right]^2, \quad (5.36)$$

and T_b can be determined as

$$T_b = \frac{1}{2} \bar{m}_b \int_0^L (y \omega_b)^2 dx, \quad (5.37)$$

where \bar{m}_b , is the mass per unit length of the beam. Therefore, the maximum kinetic energy of the system is determined by

$$T_{max} = \frac{1}{2} \bar{m}_b \int_0^L (y \omega_b)^2 dx + \sum_{r=1}^i \frac{1}{2} m_r \left[A \left(1 - \cos \frac{\pi x_{mr} m_r}{2L_b} \right) \omega_b \right]^2, \quad (5.38)$$

which after simplification, yields

$$T_{max} = \frac{1}{2} A^2 \omega_b^2 \left\{ \frac{\bar{m} L_b (3\pi - 8)}{2\pi} + \sum_{r=1}^i m_r \left(1 - \cos \frac{\pi x_{mr} m_r}{2L_b} \right)^2 \right\}. \quad (5.39)$$

Noting that the potential energy of the cantilever is equal to the strain energy stored in the structure, the maximum potential energy, V_{max} , is determined by

$$V_{max} = \frac{1}{2} E_b I_b \int_0^L \left(\frac{d^2 y}{dx^2} \right)^2 dx, \quad (5.40)$$

substitution of Eq. 5.33 and simplification yields

$$V_{max} = \frac{A^2 E_b I_b \pi^4}{64 L_b^3}. \quad (5.41)$$

The frequency equation of a cantilever, with multiple masses attached, can be determined by combination of Eqs. 5.39 and 5.41 to yield

$$\omega_b = \sqrt{\frac{2\pi^5 E_b I_b}{32L_b^3 \left\{ \bar{m}_b L_b (3\pi - 8) + 2\pi \left[\sum_{r=1}^i m_r \left(1 - \cos \frac{\pi x_{mr} m_r}{2L_b} \right) \right] \right\}}} . \quad (5.42)$$

By using Eq. 5.42, the fundamental natural frequency of the cantilever without any additional masses attached is determined to be 295.7 Hz, which has a difference of 0.3 % when compared with the natural frequency obtained with Eq. 5.31. This result indicates that Eq. 5.42 provides an accurate estimation of the natural frequency of the cantilever.

With Eq. 5.42, analysis was performed to predict the fundamental natural frequency of the cantilever with an accelerometer attached at various locations along its longitudinal axis. Representative results are summarized in Fig. 5.6. The results indicate a nonlinear relationship between the fundamental natural frequency of the cantilever and the location of one accelerometer. The natural frequency of the cantilever varies from 295.74 Hz with the accelerometer attached at its base, to 295 Hz with the accelerometer attached at its free end.

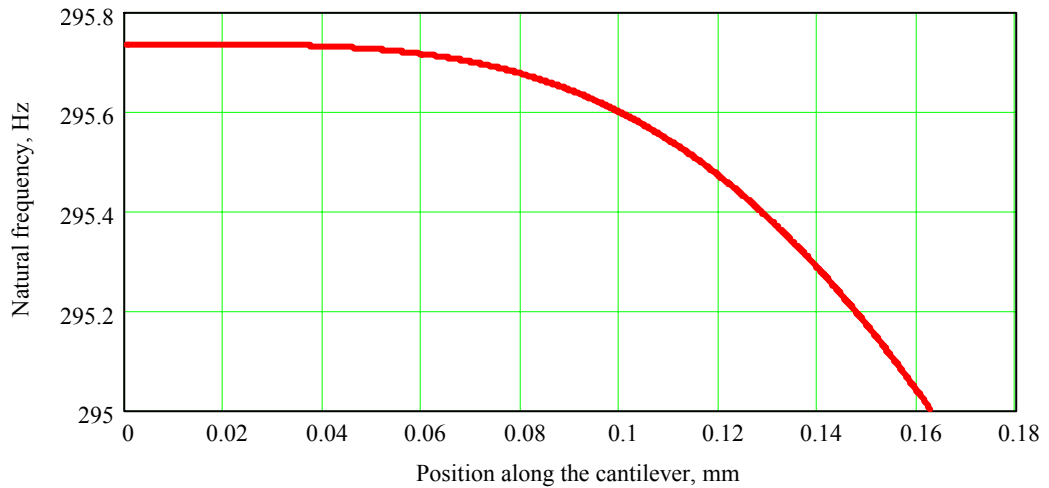


Fig. 5.6. Fundamental natural frequency of the cantilever versus the locations of one accelerometer attached along the longitudinal axis of the cantilever.

Equation 5.42 was used to determine the natural frequency of the cantilever with the attachment of five accelerometers. The accelerometers were evenly distributed along the cantilever, with locations at 0 mm, 40.6 mm, 81.3 mm, 121.9 mm, and 162.2 mm, respectively. This configuration yielded the natural frequency of the cantilever to be 294.7 Hz. Comparing this result with the cantilever without any additional mass attached, the change in the natural frequency is determined to be 1 Hz, or 0.34 %. This result indicates that attachment of MEMS accelerometers introduce minimum yet measurable effects to the natural frequency of the test structure.

5.1.2. Computational considerations

A computation model of the cantilever was generated based on its dimensions and material properties. The purpose of performing computation analysis was to predict the natural frequencies and the corresponding mode shapes of the cantilever. The results were used to compare with analytical and experimental results. Figure 5.7 shows CAD model of the cantilever of interest (Pro/Engineer, 2001; Toogood, 1998).

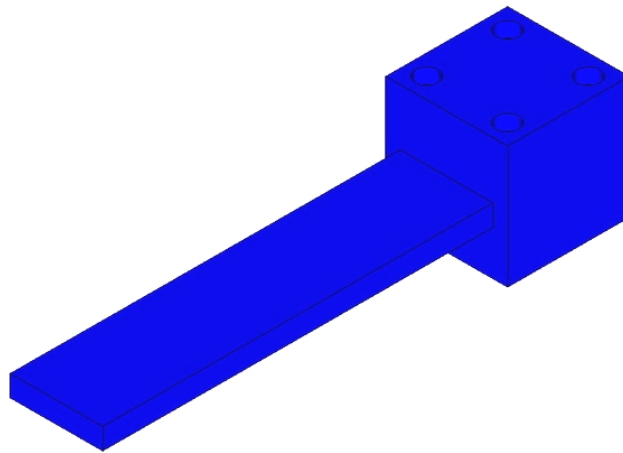


Fig. 5.7. CAD model of the cantilever.

FEM was applied to study the modal characteristics of the cantilever by solving an eigenvalue problem corresponding to undamped and free-vibrations conditions. Figure 5.8 displays FEM predicted mode shape of the fundamental natural frequency calculated at 264.7 Hz, while Figs 5.9 to 5.12 show the second to the fifth modes of vibration of the cantilever. Table 5.2 summarizes the FEM results for the first five modes of vibration and the corresponding calculated frequencies (Toogood, 2000).

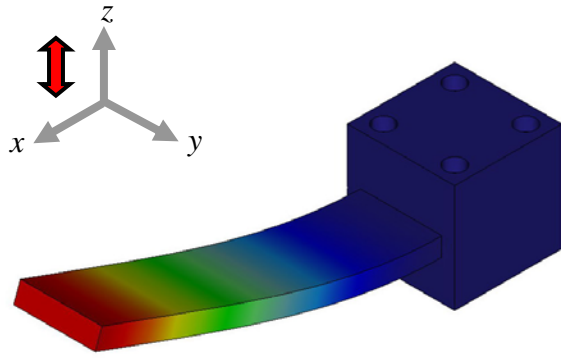


Fig. 5.8. 1st mode of vibration determined at 264.7 Hz. The cantilever deforms along the z axis.

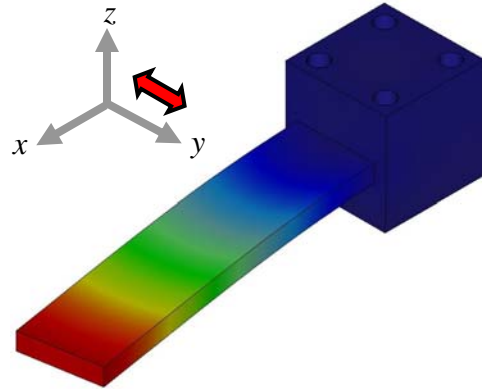


Fig. 5.9. 2nd mode of vibration determined at 1008.4 Hz. The cantilever deforms along the y axis.

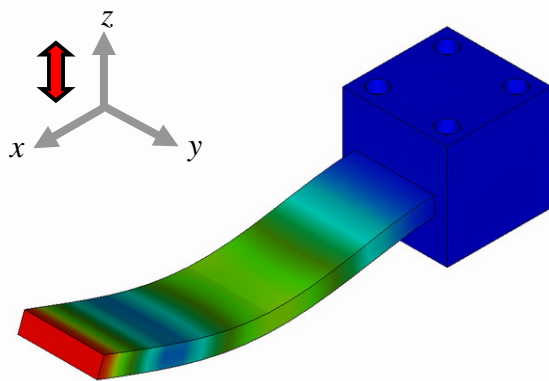


Fig. 5.10. 3rd mode of vibration determined at 1636.9 Hz. The cantilever deforms along the z axis.

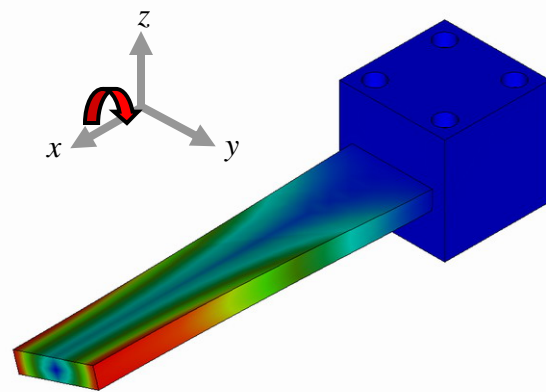


Fig. 5.11. 4th mode of vibration determined at 2075.8 Hz. The cantilever twists about the x axis.

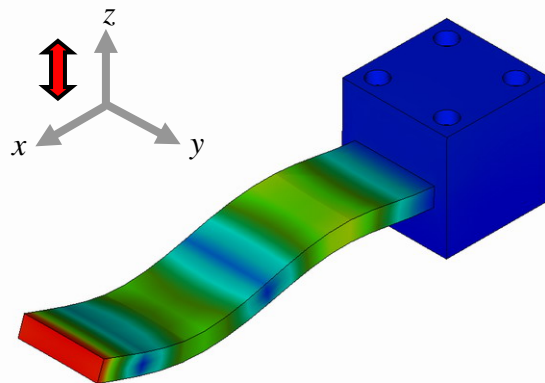


Fig. 5.12. 5th mode of vibration determined at 4515.0 Hz. The cantilever deforms along the z axis.

Table 5.2. FEM calculated modes of vibrations of the cantilever.

Mode number	Frequency, Hz	Modes of vibration
1	264.7	1st bending
2	1008.4	1st in-plane
3	1636.9	2nd bending
4	2075.8	1st torsion
5	4515.0	3rd bending

5.1.3. Experimental characterization of the cantilever

In order to perform modal analysis of the cantilever, optoelectronic holography (OEH) methodology was utilized (Furlong and Pryputniewicz, 2002; Pryputniewicz, 2003). The experimental setup consists of the cantilever, PZT, function generator, OEH system, NI DAQ system, and MEMS accelerometers. Figure 5.13 depicts schematic of the experimental setup (Kok, 2003a; Pryputniewicz, 2003).

In Fig. 5.13, the laser light is split by a beam splitter (BS). The split light is steered by mirrors (M1 and M2) to the phase shifters (PS1 and PS2). The phase shifted light source is directed to spatial filters and beam expanders (SE1 and SE2). The expanded light source of SE1 is transmitted to the object beam rotator (BR) and utilized to illuminate the cantilever. This beam is referred to as the object beam. Reflection of the cantilever is collected by a speckle interferometer (SI) and detected by a CCD camera. The expanded light of SE2 is directed to the CCD camera, to work as the reference beam, and combined with the object beam (Kreis, 1996; Pryputniewicz, 2003; Stetson and Brohinsky, 1985, 1987, 1988; Stetson et al., 1989).

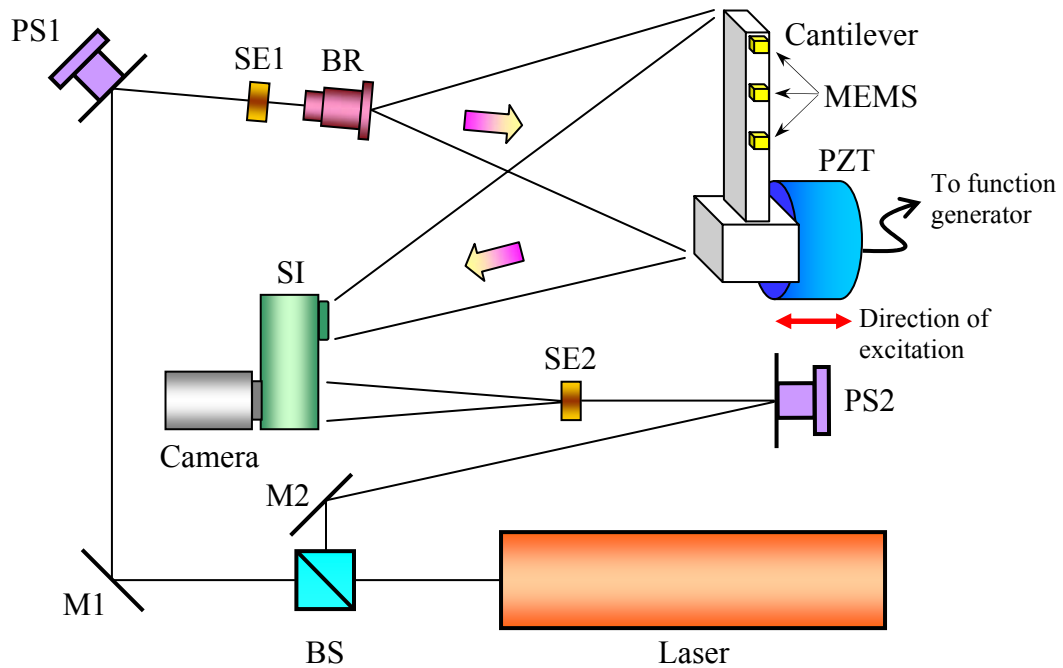


Fig. 5.13. Optoelectronic holography (OEH) system used to perform modal analysis of the cantilever with attached MEMS accelerometers (Pryputniewicz, 2003).

By using the time-averaged optoelectronic holographic technique, deformation of the cantilever is determined by measuring optical path length differences between object beam and the reference beam. Results of differences in optical path length induce interference of light, which in turn generate different fringe patterns on the objects (Furlong, 1999; Furlong and Pryputniewicz, 1995a, 1995b, 1998; Kreis, 1996; Pryputniewicz, 1993a, 2003; Pryputniewicz and Stetson, 1989).

In the setup shown in Fig. 5.13, the cantilever was rigidly attached to the piezoelectric shaker, which in turn was driven by sinusoidal signals. The amplitude of the signals were varied from 1 to 24 V, and the driving frequency was swept from 0 Hz to

10 kHz with an increment of 0.01 Hz. Multiple measurements were performed to obtain representative results.

The first experiment involved exciting the cantilever to determine its natural frequencies and the corresponding mode shapes. The second experiment was performed with five MEMS accelerometers attached along the side of the cantilever, with locations at 0 mm, 40.6 mm, 81.3 mm, 121.9 mm, and 162.2 mm, to study the effects of MEMS accelerometers to the modal characteristics of the cantilever.

Representative OEH results are displayed in Figs 5.14 and 5.15, which show the interferograms of the cantilever resonating at its first and second bending modes of vibrations. For each figure, interferograms on the left side represent the cantilever without MEMS accelerometer attached, and interferograms on the right side represent the cantilever with attached MEMS accelerometers. Table 5.3 summarizes the magnitude of the observed natural frequencies of vibration of the cantilever. Experimental results indicate that MEMS accelerometers introduce minimum, yet measurable, effects on the dynamic characteristics of the cantilever (Kok et. al., 2004).

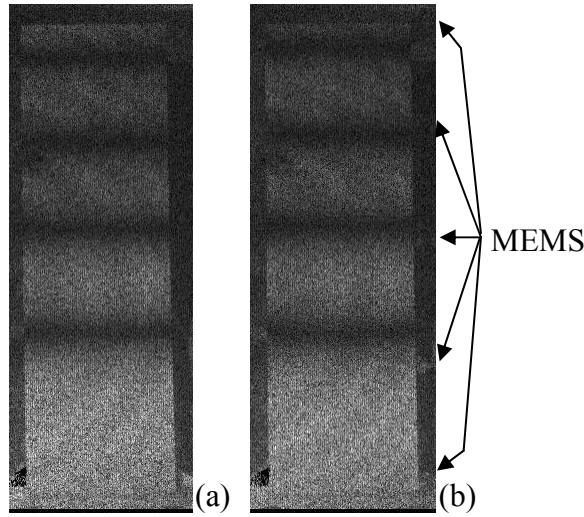


Fig. 5.14. 1st bending mode of the cantilever: (a) without MEMS accelerometer attached and, (b) with MEMS accelerometer.

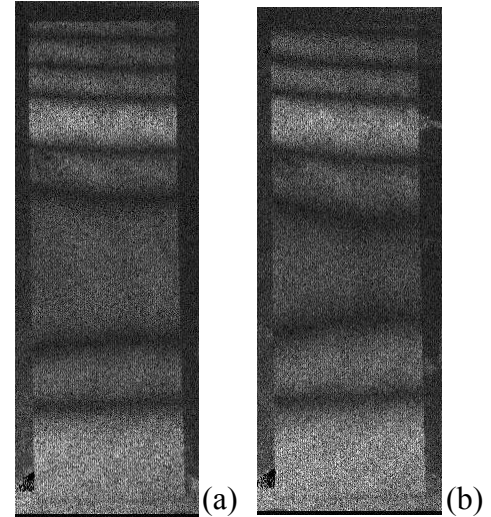


Fig. 5.15. 2nd bending mode of the cantilever: (a) without MEMS accelerometer attached and, (b) with MEMS accelerometer.

Table 5.3. Experimental determination of natural frequencies of the test cantilever using OEH methodologies (Furlong and Pryputniewicz, 2002; Pryputniewicz, 2003).

	1st bending	2nd bending
Without MEMS	290.5 Hz	1834.0 Hz
With MEMS	290.5 Hz	1832.5 Hz

Table 5.4 summarizes natural frequencies of the cantilever, determined using analytical, computational, and experimental techniques. For the first bending mode, comparisons of analytical and experimental results showed a difference of 2.40 %, while the comparisons of computational and experimental results show a difference of 9.81 %. The results indicate that the analytical approach provides acceptable determination of modal characteristics of the cantilever.

Table 5.4. Natural frequencies of the cantilever determined using analytical, computational, and experimental techniques

Mode of vibration	Analytical (Eq. of motion)	Analytical (Rayleigh)	Experimental	Computational
1st bending	283.8 Hz	294.8 Hz	290.6 Hz	264.7 Hz
2nd bending	1778.5 Hz	N/A	1967.0 Hz	1636.9 Hz
3rd bending	4980 Hz	N/A	N/A	4515.0 Hz

Using the analog wireless system, five MEMS accelerometers were attached along the side of the cantilever to perform preliminary experimental modal analysis. The locations of the accelerometers were evenly distributed along the cantilever, as shown in Figs 5.14 and 5.15. The cantilever was excited at its natural frequencies, and the outputs of the accelerometers were wirelessly transmitted to perform spectrum analysis. Power spectra of the MEMS accelerometers were determined, and by plotting the power spectra of the individual accelerometers, the mode shapes of the cantilever were reconstructed. Figure 5.16 summarizes preliminary experimental modal analysis of the cantilever using the analog wireless MEMS system developed in this Thesis. Results of Fig. 5.16 correlate well with the results shown in Fig. 5.3.

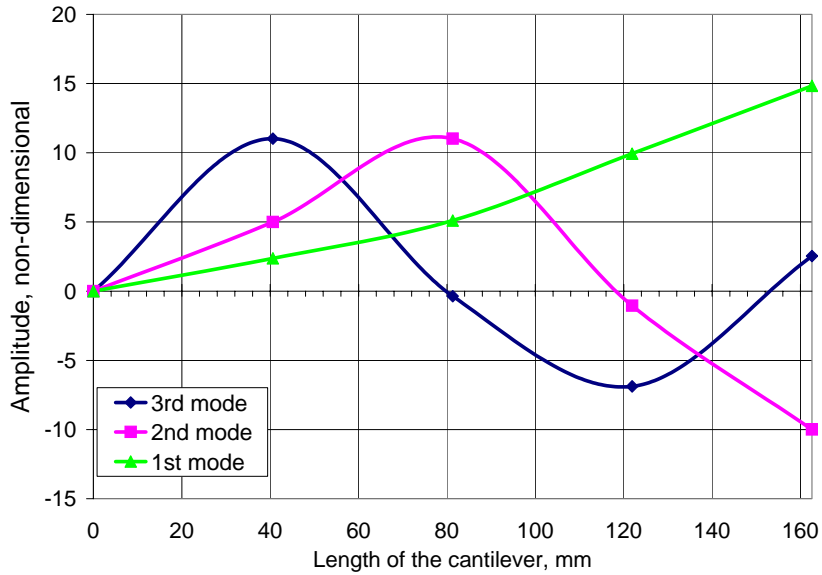


Fig. 5.16. Mode shapes of vibration of the cantilever measured using the analog wireless MEMS inertial system.

In Fig. 5.16, the horizontal axis represents the length of the cantilever, and the vertical axis shows the non-dimensional amplitude of the cantilever. Results illustrate feasibility of using the analog wireless MEMS inertial system to experimental modal analysis. The results also indicate that resolution of the measurements can be improved by using additional accelerometers.

5.2. Tilt and rotation measurements

MEMS accelerometers, integrated with the digital wireless system, were applied to perform high resolution tilt and rotation measurements of an object subjected to angular and linear accelerations. In order to verify the functionality and the resolution of

the digital wireless system, an experimental setup was developed based on the utilization of a computerized, high resolution rotational stage. The programs were developed for the system, and the system was calibrated to yield high-resolution measurements.

5.2.1. Programming of the microcontroller

The microcontroller and the RF modules are designed to be programmable with the PBASIC language (Parallax, 2004; Lindsay, 2003a, 2003b; Kok et al., 2004a, 2004b). A PBASIC program is constructed in three major sections: definition of the microcontroller, definition of the variables, and control code. The control program is downloaded to the EEPROM of the microcontroller after being successfully compiled (Parallax, 2004; Lindsay, 2003a, 2003b).

The MEMS accelerometers utilized in the developments use changes in gravitational forces to perform tilt and rotation measurements. Angular measurements are achieved by measuring the duty cycle of the digital output signals generated by the accelerometer (Analog Devices, 2001; Hsu, 2002; Kovacs, 1998). Figure 5.17 shows a typical digital output signal corresponding to one of the axes of the MEMS accelerometer. In Fig. 5.17, time t_1 is proportional to changes in gravitational forces, and time t_2 is the period of the carrier signal. At 0g acceleration, the ratio of the duty cycle is 50%.

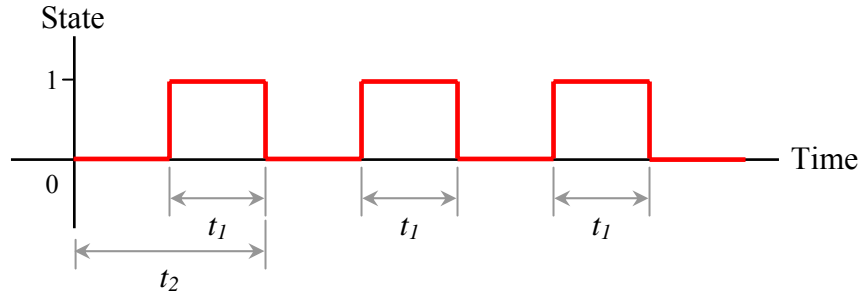


Fig. 5.17. Digital output signal of a MEMS accelerometer.

The code developed consists of a main program and three subroutines. The first subroutine was used to measure the pulse width of the digital output signals of the accelerometer. Measurement of pulse width can be achieved by using the pulse in (PULSIN) command, which has the following format (Lindsay, 2003a, 2003b)

`PULSIN Pin, State, Variable`

where *Pin* defines which I/O pin on the microcontroller board is connected to the input data source. *State* defines the logical state, which is either low (0) or high (1), of which the duty cycle will be measured. Since t_1 represents the pulse width of the “on” portion of the duty cycle, the *State* of the program is defined as high in this case. The measured data is saved as a specific *Variable* that is defined by the programmer to perform further analysis. Using this command, pulse width of t_2 can be measured by summing the pulse width of the “on” portion and the pulse width of the “off” portion.

After duty cycles are measured, gravitational forces for each axis of the accelerometer are calculated using (Analog Devices, 2001; Kok et al, 2004a, 2004b, 2004c)

$$A(g) = \left(\frac{t_1}{t_2} - \eta_1 \right) \cdot \eta_2 \quad . \quad (5.43)$$

In Eq. 5.43, $A(g)$ is the acceleration measured in g's ($1 \text{ g} = 9.81 \text{ m/s}^2$), η_1 is the ratio of the duty cycle outputs at 0 g, and η_2 is the reciprocal sensitivity of the accelerometer. According to the manufacturer, η_1 is equal to 0.5 as the duty cycle of the accelerometer is 50 % at 0 g, and η_2 is equal to 8 because the accelerometer has a sensitivity of 12.5 %/g.

With dual-axes acceleration determined, tilt and rotation measurements, θ , are performed. The second subroutine of the program converts acceleration from g's, to tilt angles in degrees, by using the equation (Analog Devices, 2001; Kok et al, 2004a, 2004b, 2004c),

$$\theta = \sin^{-1} \left[\frac{A(g)}{1g} \right] \quad . \quad (5.44)$$

Instead of 0° to 360° , or $2-\pi$ radians, a circle is represented from 0 to 256 brads (i.e., binary radian) for the selected microcontroller. Therefore, cosine of an angle varies from -127 to 127, which is identical to -1 to 1 in radian scale. Due to this difference in scale, t_1 needs to be normalized to 127 before it can be substituted into Eq. 5.43. Also, after the angle in brads is determined, the result needs to be converted back to degrees for display. In order to display the measured angle in the correct units, a third subroutine was developed to correct the sign of the output (EME systems, 2001).

After the calculations are completed, the program returns to the main routine to display the results. By using the debug command (DEBUG) in the PBASIC program, the

values can be displayed in the debug terminal. The debug terminal is opened by execution of the program, or it can be opened by selecting *Run* → *Debug* → *New* and then selecting the COM Port that is connected to the microcontroller (Lindsay, 2003a, 2003b). Figure 5.18 shows snapshot of the debug terminal.

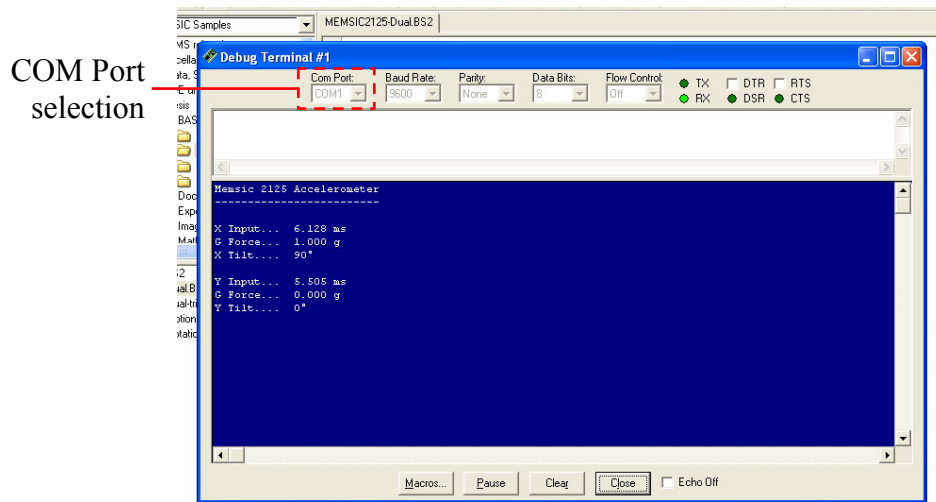


Fig. 5.18. Debug terminal showing dual-axes acceleration measurements.

The final portion of the program was developed to send the measured data to the transmitter for wireless transmission. In this case, the serial out command (SEROUT) was utilized. The SEROUT command has the following format (Lindsay, 2003a, 2003b)

SEROUT *Tpin*, *Baudmode*, [*OutputData*]

Tpin specifies which I/O pin of the microcontroller board is connected to the data out pin of the transmitter, as shown in Fig. 4.11. *Baudmode* defines the serial timing configuration, which is equal to 9600 bauds for the microcontroller. *OutputData* specifies the data that will be transmitted.

The program at the receiver unit follows a similar procedure as the transmitter. In order to receive wireless data, the serial in command (SERIN) is utilized. SERIN command has the following format (Lindsay, 2003a, 2003b),

SERIN Rpin, Baudmode, [InputData]

Similar to SEROUT, *Rpin* specifies which I/O pin of the microcontroller board is connected to the data in pin of the receiver, and *InputData* specifies the input data into the specified variables.

Figure 5.19 shows the flow diagram of the programs and subroutines utilized in the RF transmitter and receiver units. Figure 5.19 (a) represents the flow diagram of the transmitter unit, and Fig. 5.19 (b) represents the flow diagram of the receiver unit. For the transmitter unit, the control code was developed to measure the pulse widths of the duty cycle outputs of the MEMS accelerometers. By utilizing the pulse widths, for each axis, into Eq. 5.43, dual-axes accelerations were determined. With the dual-axes acceleration recovered and by applying Eq. 5.44, θ was determined. The acceleration and angular measurements were then displayed in both numeric and graphical formats. In addition, the results were exported to data files for future use. In order to achieve high resolution measurements, the results were evaluated based on 16 bit arithmetic. However, the RF component utilized in the developments can only transmit 8 bits data. Therefore, the measured pulse widths were scaled to 8 bit for wireless transmission. The complete source codes of the transmitter and the receiver units are shown in Appendix C and D (Kok et al, 2004a, 2004b, 2004c; Parallax, 2003b).

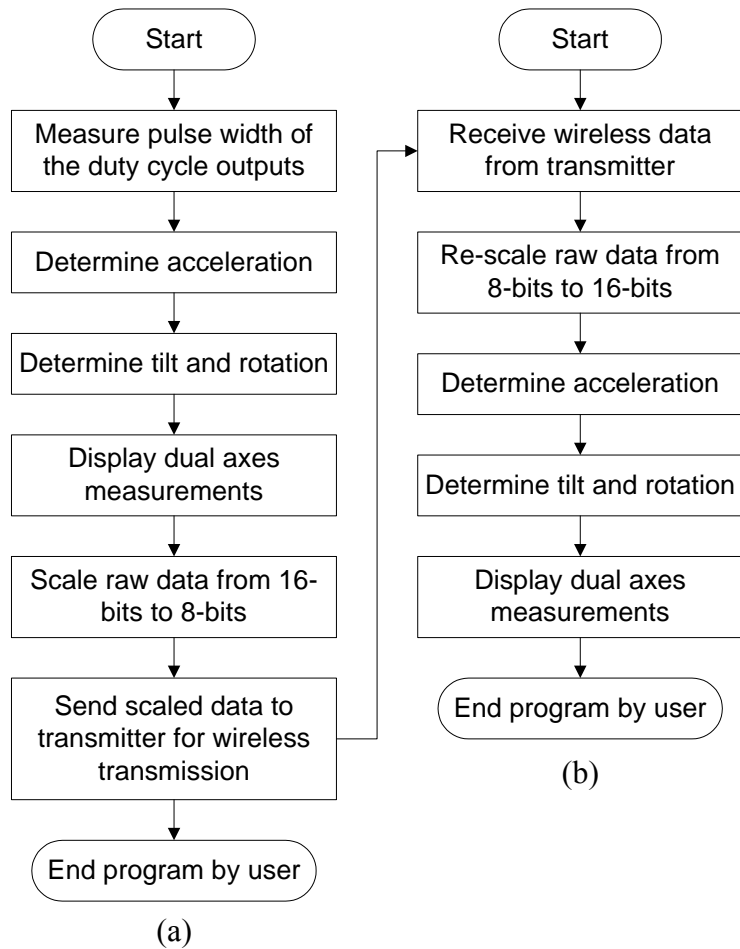


Fig. 5.19. Flow diagram of the program developed to interface digital output signals of the MEMS accelerometer with the wireless microcontroller system: (a) transmitter unit, and (b) the receiver unit.

5.2.2. Graphical display of measurements

The Debug terminal of the BASIC Stamp Editor can only display real time measurements and has no capability of saving the results. In order to demonstrate real-time measurements in a graphical display and to save the results, StampPlot Pro from

SelmaWare was utilized (StampPlot, 2003). StampPlot Pro is compatible with the PBASIC language. It is capable to display and export measurements of multiple channels into a text file and it also provides real-time graphical display of data (SelmaWare, 2003).

The DEBUG command was utilized to send data for display in StampPlot Pro. The DEBUG command has the following format (SelmaWare, 2003; StampPlot Pro, 2003),

```
DEBUG DEC var1, ",", DEC var2, ",", DEC var3
```

In this command, DEC is the decimal formatter that is used to display variables in decimal form, and *var1* to *var3* represent the variables of the measurements. The program is capable to display up to 10 different variables (Lindsay, 2003a, 2003b; StampPlot Pro, 2003). Since the Debug terminal and the StampPlot window obtains data from the microcontroller via the serial port, both windows cannot be opened at the same time. To obtain graphical display of data, the first step is to execute the PBASIC program, the second step is to close the Debug terminal in the BASIC Stamp editor, and the last step is to execute the StampPlot window to display and record the data (StampPlot Pro, 2003). Figure 5.20 shows the interface of StampPlot Pro.

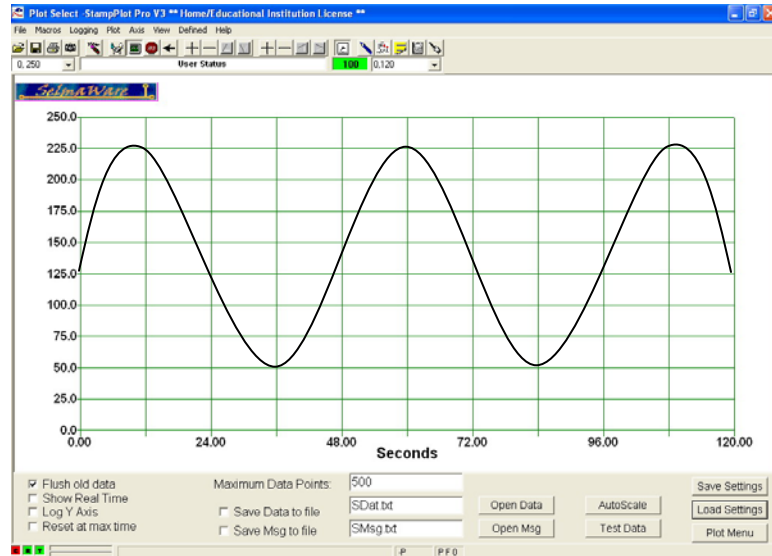


Fig. 5.20. Interface of the StampPlot Pro program used to display graphical information from the developed digital wireless system.

5.2.3. Calibration of the ADXL202 accelerometer with the microcontroller system

MEMS accelerometers are designed to operate at a carrier frequency ranging from 100 Hz to 1 kHz, which can be defined by the driving electronics. In order to balance the speed of the microcontroller with the output speed of the MEMS sensors, the carrier frequency of the digital output signals of the sensors is recommended to be 100 Hz (Analog Devices, 2004; Application Note, 2001). Actual driving electronics, however, induce slight inherent variations in duty cycles since typical resistors used to define the driving electronics have approximately 2% to 5% tolerances. Even with high accuracy components, it is difficult to achieve steady duty cycles at a frequency of 100 Hz. In order to compensate for such variations, calibration of the accelerometer and the microcontroller system was performed (Kok et al., 2004a, 2004b, 2004c).

An experimental setup to produce high-resolution tilts and rotations was developed and used to perform accurate characterization of the wireless system. The setup consisted of a high precision rotational stage (Newport, 2004a), a computerized motion controller (Newport, 2004b), an oscilloscope, the digital wireless accelerometer system, and a computer. For the MEMS accelerometer driving circuit, frequencies of the duty cycles of the accelerometer were measured with an oscilloscope, and adjusted by using different resistors to achieve 100 Hz with minimal deviations. Once the accelerometer circuitry was adjusted, the wireless system was rigidly attached to the rotational stage and orientated in such a way that the x -axis and the y -axis of the accelerometer were parallel and perpendicular to the earth's surface, respectively. Figure 5.21 shows configuration of the experimental setup, which shows the original orientation of the inertial sensor, and Fig. 5.22 shows the actual transmission unit attached to the high-precision rotational stage (Kok et al., 2004a, 2004b, 2004c).

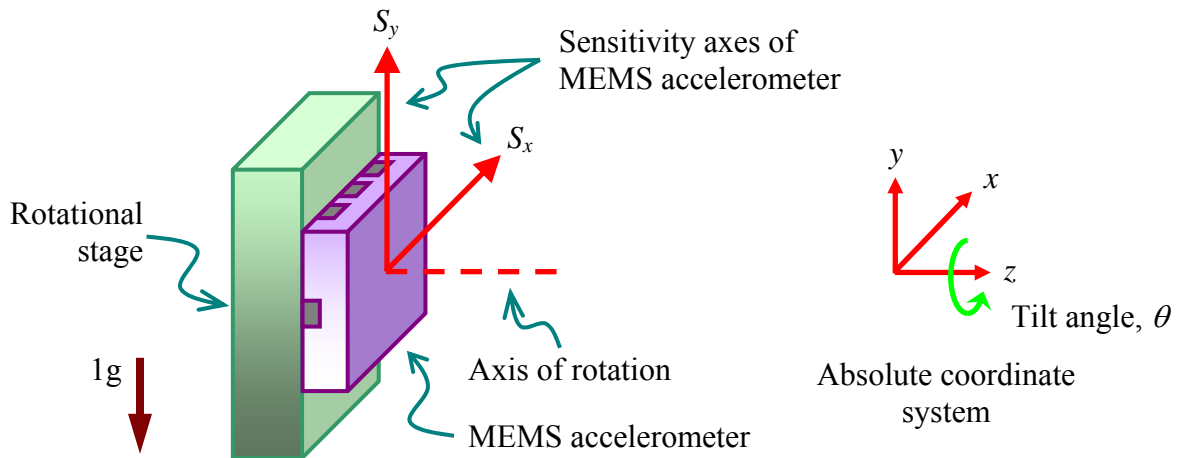


Fig. 5.21. Schematic diagram showing the coordinate system used in the calibration process of the MEMS accelerometer.

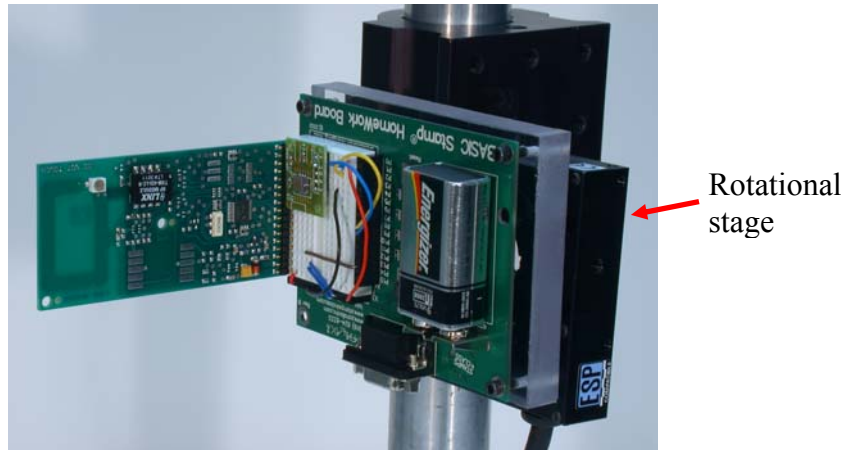


Fig. 5.22. Experimental setup showing the wireless transmitter unit and the high-resolution rotational stage.

According to the specifications of the MEMS accelerometer, the measured gravitational acceleration for dual-axes varies from -1 g to 1 g. The accelerometer has the largest sensitivity when the measuring axis is parallel to the direction of the force of gravity and the accelerometer is insensitive when the measuring axis is perpendicular to the earth's surface (Analog Devices, 2001). The initial position of the inertial sensor was orientated as shown in Fig. 5.21, where the x -axis has 0 g acceleration and the y -axis has 1 g acceleration. In order to perform fine adjustments to precisely align the inertial sensor, t_1 of the y -axis was utilized. The accelerometer was rotated by angular increments of 0.01° , in both directions, until t_1 of the y -axis reached its maximum.

Dual-axes angular measurements were performed after the initial orientation of the accelerometer was determined. In order to calibrate the accelerometer and the microcontroller system, t_1 and t_2 for each axis, were measured using the microcontroller

and the programs that were developed. With the high precision rotational stage, the inertial sensor was rotated 360° and measurements were taken.

Figure 5.23 shows results of the initial rotation measurements. The results illustrate that acceleration of the x-axis varies from -0.86g to 1.24g, while acceleration of the y-axis varies from 1.02g to 0.96g.

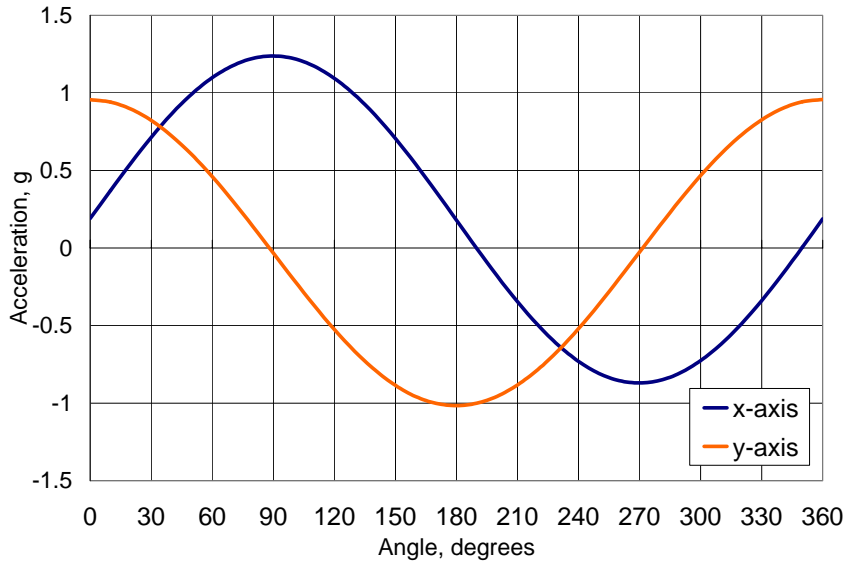


Fig. 5.23. Uncalibrated dual-axes acceleration measurements as a function of a full 360° rotation.

The result of the initial measurements indicate the need for calibration of the measurements output, which is performed by using Eqs 5.45 and 5.46, as

$$\sin \theta = \left(\frac{t_1}{t_2} - \eta_1 \right) \cdot \eta_2 \quad , \quad (5.45)$$

or,

$$\sin \theta = \frac{t_1}{t_2} \cdot \eta_2 - \eta_3 \quad , \quad (5.46)$$

by introducing a new variable η_3 defined as

$$\eta_1 \cdot \eta_2 = \eta_3 \quad . \quad (5.47)$$

The calibration process consisted of the determination of the two unknown η_2 and η_3 . Since the accelerometer was rotated 360° while multiple measurements, p , were taken, Eq. 5.46 can be expressed in matrix form as

$$[M_1] = [M_2] \cdot [M_3] \quad , \quad (5.48)$$

where

$$[M_1] = \begin{bmatrix} \sin \theta_1 \\ \sin \theta_2 \\ \vdots \\ \sin \theta_p \end{bmatrix} \quad , \quad (5.49)$$

$$[M_2] = \begin{bmatrix} \begin{pmatrix} t_1 \\ t_2 \end{pmatrix}_1 & 1 \\ \begin{pmatrix} t_1 \\ t_2 \end{pmatrix}_2 & 1 \\ \vdots & \vdots \\ \begin{pmatrix} t_1 \\ t_2 \end{pmatrix}_p & 1 \end{bmatrix} \quad , \quad (5.50)$$

and

$$[M_3] = \begin{bmatrix} \eta_2 \\ -\eta_3 \end{bmatrix} \quad . \quad (5.51)$$

Calibration of the measurements was achieved by determining the unknowns η_2 and η_3 . With matrices M_1 , M_2 , and M_3 defined by Eq. 5.49 to Eq. 5.51, respectively,

application of the least-squares error minimization technique to Eq. 5.48 yields

(Pryputniewicz, 1993)

$$[M_2]^T \cdot [M_1] = [M_2]^T \cdot [M_2] \cdot [M_3] \quad , \quad (5.52)$$

which can be expanded as,

$$\begin{bmatrix} \left(\frac{t_1}{t_2}\right)_1 & \left(\frac{t_1}{t_2}\right)_2 & \dots & \left(\frac{t_1}{t_2}\right)_p \\ 1 & 1 & \dots & 1 \end{bmatrix} \cdot \begin{bmatrix} \sin \theta_1 \\ \sin \theta_2 \\ \vdots \\ \sin \theta_p \end{bmatrix} = \begin{bmatrix} \left(\frac{t_1}{t_2}\right)_1 & \left(\frac{t_1}{t_2}\right)_2 & \dots & \left(\frac{t_1}{t_2}\right)_p \\ 1 & 1 & \dots & 1 \end{bmatrix} \cdot \begin{bmatrix} \left(\frac{t_1}{t_2}\right)_1 & 1 \\ \left(\frac{t_1}{t_2}\right)_2 & 1 \\ \vdots & \vdots \\ \left(\frac{t_1}{t_2}\right)_p & 1 \end{bmatrix} \cdot \begin{bmatrix} \eta_2 \\ -\eta_3 \end{bmatrix} \quad \text{or,}$$

$$\begin{bmatrix} \sum_{s=1}^p \left(\frac{t_1}{t_2}\right)_s \cdot \sin \theta_s \\ \sum_{s=1}^p \sin \theta_s \end{bmatrix} = \begin{bmatrix} \sum_{s=1}^p \left(\frac{t_1}{t_2}\right)_s^2 & \sum_{s=1}^p \left(\frac{t_1}{t_2}\right)_s \\ \sum_{s=1}^p \left(\frac{t_1}{t_2}\right)_s & \sum_{s=1}^p p_s \end{bmatrix} \cdot \begin{bmatrix} \eta_2 \\ -\eta_3 \end{bmatrix} \quad . \quad (5.53)$$

By setting,

$$J_1 = \sum_{s=1}^p \left(\frac{t_1}{t_2}\right)_s \cdot \sin \theta_s \quad , \quad (5.54)$$

$$J_2 = \sum_{s=1}^p \sin \theta_s \quad , \quad (5.55)$$

$$J_3 = \sum_{s=1}^p \left(\frac{t_1}{t_2}\right)_s^2 \quad , \quad (5.56)$$

$$J_4 = \sum_{s=1}^p \left(\frac{t_1}{t_2} \right)_s , \quad (5.57)$$

$$J_5 = \sum_{s=1}^p p_s , \quad (5.58)$$

Eq. 5.53 yields,

$$\begin{bmatrix} J_1 \\ J_2 \end{bmatrix} = \begin{bmatrix} J_3 & J_4 \\ J_4 & J_5 \end{bmatrix} \cdot \begin{bmatrix} \eta_2 \\ -\eta_3 \end{bmatrix} , \quad (5.59)$$

therefore, the two unknowns constants, η_2 and η_3 , can be determined as,

$$\begin{bmatrix} \eta_2 \\ -\eta_3 \end{bmatrix} = \frac{1}{J_3 J_5 - J_4^2} \begin{bmatrix} J_5 & -J_4 \\ -J_4 & J_3 \end{bmatrix} \cdot \begin{bmatrix} J_1 \\ J_2 \end{bmatrix} . \quad (5.60)$$

Based on the dual-axes measurements, J_1 to J_5 , for the x and y axis, are equal to

$$\begin{aligned} J_{1x} &= 2.369 , \\ J_{2x} &= -8.323 \times 10^{-17} , \\ J_{3x} &= 10.434 , \\ J_{4x} &= 19.352 , \\ J_{5x} &= 37 , \end{aligned} \quad (5.61)$$

and,

$$\begin{aligned} J_{1y} &= 2.838 , \\ J_{2y} &= 1 , \\ J_{3y} &= 9.526 , \\ J_{4y} &= 18.488 , \\ J_{5y} &= 37 . \end{aligned} \quad (5.62)$$

By substituting Eqs 5.61 and 5.62 into Eq. 5.60, η_2 and η_3 for the x and y axis are determined to be

$$\begin{aligned} \eta_{2_x} &= 7.597 \quad , \\ \eta_{3_x} &= 3.973 \quad , \end{aligned} \tag{5.63}$$

and,

$$\begin{aligned} \eta_{2_y} &= 8.114 \quad , \\ \eta_{3_y} &= 4.027 \quad . \end{aligned} \tag{5.64}$$

Recalling that η_2 represents the reciprocal sensitivity of the accelerometer and using the experimental results, the x and the y -axis of the MEMS accelerometer have sensitivities of 13.163 %/g and 12.324 %/g, respectively. Comparing these results with the manufacturer's specifications, the x -axis has a deviation of 5.037 % and the y -axis has a deviation of -1.428 % in sensitivity. In addition, the x -axis has a deviation of 4.398% and the y -axis has a deviation of -0.806% in ratio of duty cycle. Representative results of the calibrated rotation measurements are shown in Figs 5.24 and 5.25 (Kok et al., 2004a, 2004b, 2004c).

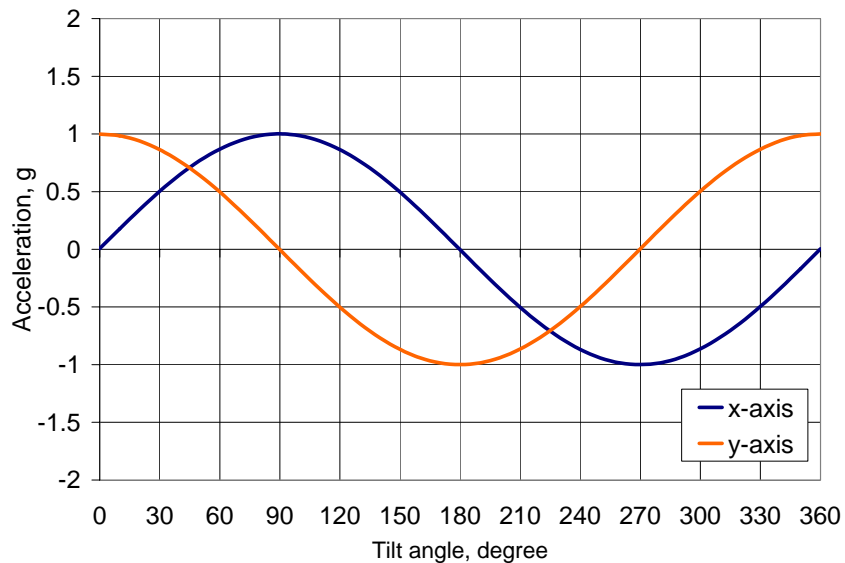


Fig. 5.24. Calibrated rotation measurements using the developed digital wireless data acquisition system and the dual-axes MEMS inertial sensor.

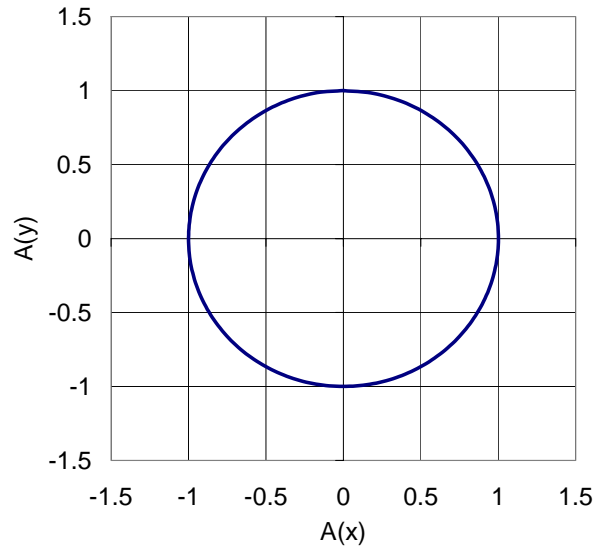


Fig. 5.25. Polar representation of dual-axes measured with the developed wireless data acquisition system. $A(x)$ is acceleration along the x -axis, and $A(y)$ is acceleration along the y -axis.

With η_2 and η_3 determined, the resolution of the rotation measurements was evaluated by using uncertainty analysis based on the root mean square (RSS) approach as (Pryputniewicz, 1993)

$$\delta(\sin \theta) = \sqrt{\left[\frac{\partial(\sin \theta)}{\partial t_1} \delta t_1 \right]^2 + \left[\frac{\partial(\sin \theta)}{\partial t_2} \delta t_2 \right]^2}, \quad (5.65)$$

where,

$$\frac{\partial(\sin \theta)}{\partial t_1} \left(\frac{t_1}{t_2} \eta_2 - \eta_3 \right) = \frac{\eta_2}{t_2}, \quad (5.66)$$

and,

$$\frac{\partial(\sin \theta)}{\partial t_2} \left(\frac{t_1}{t_2} \eta_2 - \eta_3 \right) = -\frac{\eta_2}{t_2^2} \quad . \quad (5.67)$$

Equation 5.67 can, therefore, be expressed as,

$$\delta(\sin \theta) = \sqrt{\left(\frac{\eta_2}{t_2} \delta t_1 \right)^2 + \left(-\frac{\eta_2}{t_2^2} \delta t_2 \right)^2} \quad . \quad (5.68)$$

In Eqs 5.65 and 5.68, δt_1 and δt_2 represent uncertainty of the input gravitational forces of the accelerometer, and the uncertainty of the period of the accelerometer's carrier frequency, respectively. δt_1 and δt_2 were determined by the standard deviation of the measurements, and according to the experimental results and Eq. 5.68, the angular resolution of the digital wireless system, based on the dual-axes MEMS accelerometer, was determined to be 1.8 mrad, or 0.103°.

The initial wireless tilt and rotation measurements were performed with the transmitter and receiver unit separated by 1.5 m. The measurements were repeated with the RF modules separated by approximately 18.5 m. Both of these measurements indicated that the RF components introduce low noise to the transmitted signals and provide reliable wireless communication across long distances.

5.3. Angular rate measurements with MEMS gyroscopes

Experiments were performed using MEMS gyroscopes interfaced with the microcontroller to perform angular rate measurements. The same experimental setup as

described in Section 5.2.3 was utilized. Since the MEMS gyroscope only generates analog output signals, an analog to digital conversion circuit was developed.

5.3.1. Analog to digital conversion

An analog to digital conversion circuit was built to convert the analog outputs of the gyroscope to measurable digital values for the microcontroller. A signal channel 8-bit analog-to-digital (A/D) converter was utilized in the developments (Application Note, 2002). The A/D converter utilized can be driven by a 5 Vdc supply and no additional driving electronics are required for its operation. Figure 5.26 shows the connection diagram of the gyroscope with A/D conversion capabilities (Parallax, 2004; National Semiconductor, 2002, Lindsay, 2003c).

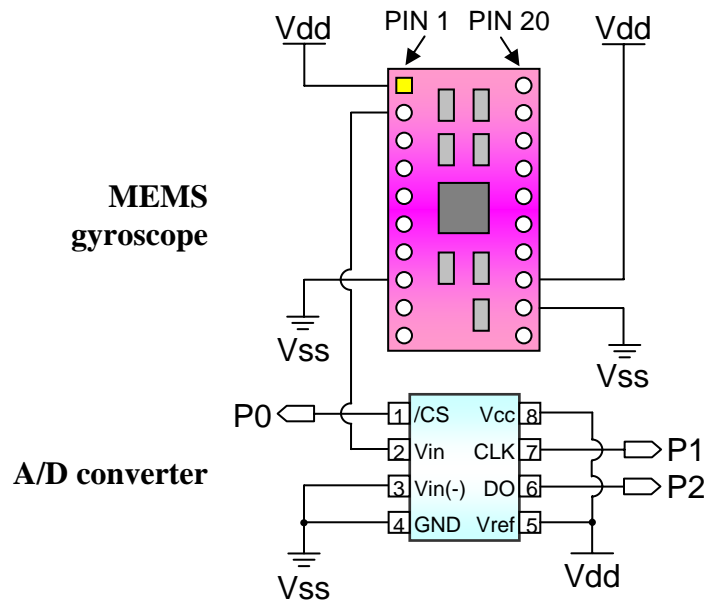


Fig. 5.26. Connection diagram of the MEMS gyroscope and the A/D converter to the microcontroller board. P0 to P2 are the corresponding I/O pins on the microcontroller board.

In Fig. 5.26, Pin1, Pin6, and Pin7 of the A/D converter are connected to P0, P2, and P1 of the microcontroller board, respectively. Pin1 of the A/D converter (/CS) is used to activate the chip. Pin7 of the converter (CLK) is the clock, and Pin6 (D0) is the serial output pin. These pins are directly interfaced and controlled by the microcontroller. Pin8 and Pin5 of the A/D converter are connected to the power supply, and Pin3 and Pin4 of the converter are connected to ground. Output pin of the MEMS gyroscope, Pin2, is connected to Pin2 of the A/D converter for analog to digital conversion (National Semiconductor, 2002; Lindsay, 2003a, 2003c).

5.3.2. Programming of the microcontroller

The core of the A/D conversion program include activation of the chip , setting of the clock at the correct duration, and synchronizing the serial data, which is achieved by the following PBASIC commands (Lindsay 2003b, 2003c)

```
HIGH CS  
LOW CS  
LOW CLK  
PULSOUT CLK, 210  
SHIFTIN data_pin, clock_pin, MSBPOST,[variable\bits]
```

The first two commands are used to send a high signal (5 V) followed by a low signal to the /CS pin to start the conversion. The third and the fourth commands are used to activate the clock and setup the pulse duration for the A/D converter, which is equal to 420 μ s, as recommended by the manufacturer to balance the speed of the microcontroller and the A/D converter. The last command sends the clock pulses to the A/D converter,

reads the output bits, and loads the output bits to the predefined variable. The results of this A/D conversion yields an 8-bit binary value (Lindsay, 2003c). The complete A/D conversion program is shown in Appendix E, and Figure 5.27 shows the flow diagram of the program.

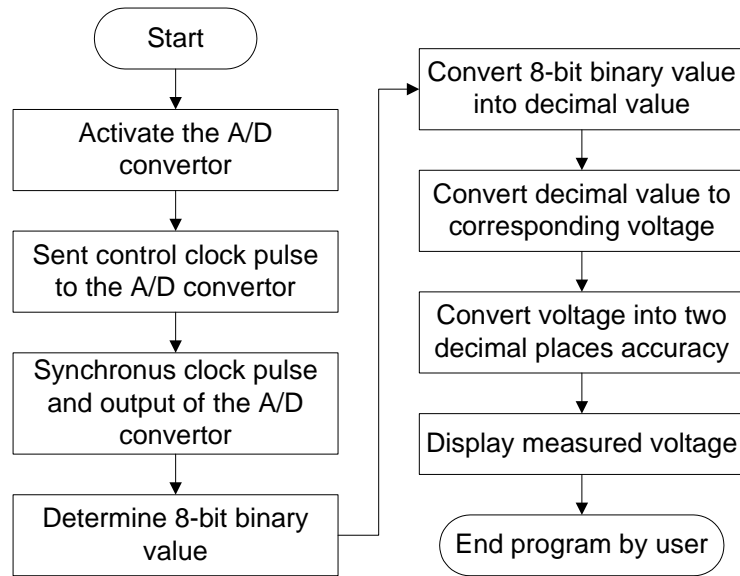


Fig. 5.27. Flow diagram of the program developed to interface the microcontroller with an ADXRS150 MEMS gyroscope.

5.3.3. Preliminary angular rate measurements

Figure 5.28 illustrates the experimental setup used for angular rate measurements with a MEMS gyroscope. Experiments were performed at different rotation speeds, varying from 1°/sec to 4°/sec, in both clockwise and counterclockwise directions. For each run, the gyroscope was rotated 45° to ensure accurate measurements.

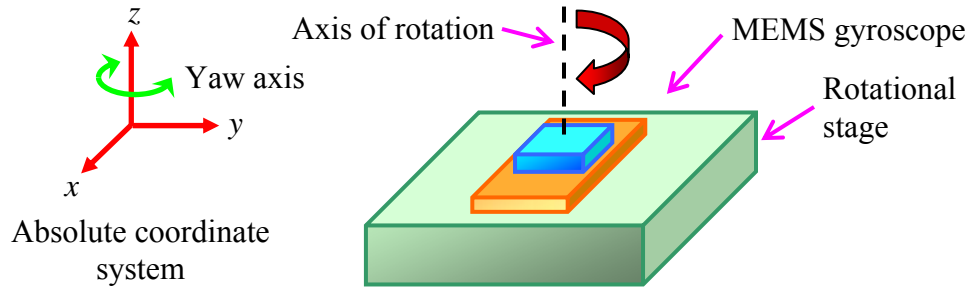


Fig. 5.28. Experimental configuration utilized to perform angular rate measurements using the ADXRS150 MEMS gyroscope.

The gyroscope produces linear analog output corresponding to the input angular rate, which can be determined by the following equation (Analog Devices, 2003b)

$$V_{out} = (0.015 \cdot R_{in}) + 2.5 \quad , \quad (5.69)$$

where V_{out} is the output voltage from the gyroscope, and R_{in} is the input angular rate in degree/sec. R_{in} is positive for clockwise rotations, and it is negative for counterclockwise rotations. Preliminary results are shown in Fig. 5.29.

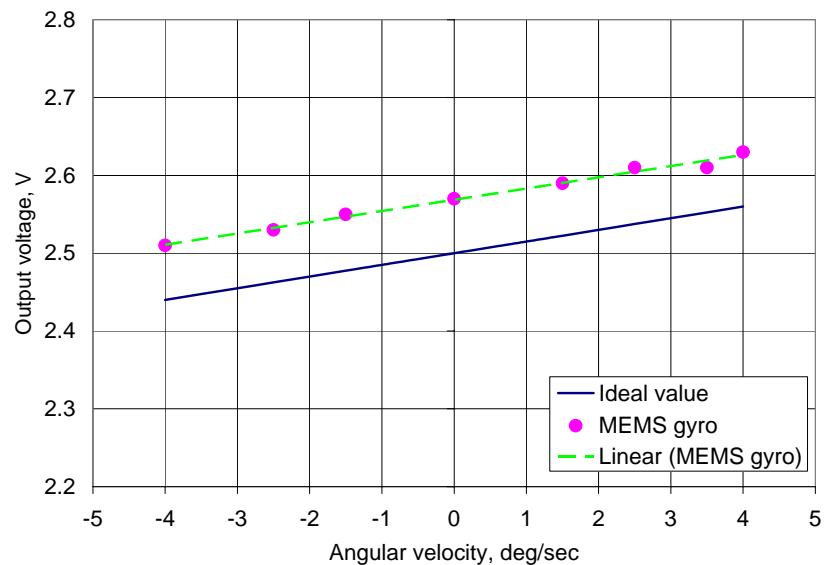


Fig. 5.29. Preliminary angular rate measurements using an ADXRS150 MEMS gyroscope and the microcontroller.

Based on the experimental results shown in fig. 5.29, the null voltage of the MEMS gyroscope, using the 8 bit A/D conversion and the microcontroller, was measured at 2.57 V. This result indicates a 0.07 V deviation from the ideal null voltage as specified by the MEMS gyroscope.

For the angular rate measurements, the linearized results show a trace that possesses the same slope as the one in ideal situation, with an offset of 0.07V. The uncertainty in measurements was caused by the limited resolution of analog to digital conversion. In order to improve the measuring accuracy, a higher resolution analog to digital converter will be utilized in the future.

6. CONCLUSIONS AND FUTURE WORKS

This thesis has demonstrated the feasibility of using MEMS inertial sensors for modal analysis of structures. It also has addressed the development of wireless systems for MEMS inertial sensors.

An in-depth study on the applicability of MEMS inertial sensors to perform health monitoring of structures was presented. The objectives of this thesis were: (1) characterize specific MEMS inertial sensors, (2) develop wireless systems to transfer output signals of MEMS sensors, (3) integrate the MEMS sensors into the wireless systems, and (4) develop applications for the wireless MEMS inertial systems.

Two commercially available MEMS inertial sensors were utilized. The Analog Devices ADXL202 dual-axes accelerometer was used to measure vibrations and orientations, and the Analog Devices ADXRS150 gyroscope was used to measure angular speeds.

The MEMS accelerometer was characterized using analytical, computational, and experimental techniques. Analytical modeling was utilized to demonstrate that measuring accuracy of the accelerometer is proportional to its fundamental natural frequency. Due to the large stiffness to mass ratios, MEMS accelerometers are characterized by high natural frequencies, which provide high measuring accuracy in wide frequency ranges while inducing minimum deviations to the measurements. Computational modeling was performed by application of FEM to study the dynamic characteristics of MEMS accelerometers. An asymmetric model of the proof mass of the accelerometer was created to determine its natural frequencies and the corresponding

mode shapes. Experimental analysis was performed by application of a laser vibrometer system. The MEMS accelerometer was subject to harmonic and random excitations in order to determine its fundamental natural frequency. Based on the computational and experimental result, the natural frequency of the accelerometer was determined to be 8.5 kHz.

The MEMS inertial sensors were integrated into two different wireless communication systems: one was designed to transmit the analog output signals, and the other was designed to transmit the digital output signals. Results of the characterizations indicate that the analog wireless system has a reliable linear FRF in the range of 400 Hz to 22 kHz, which is compatible with the FRF of the accelerometers utilized.

Modal analysis of a cantilever was performed in order to verify applicability of the analog wireless system. The results obtained were based on application of analytical, computation, and experimental methodologies. Analytical characterization was performed to determinate the natural frequency of the cantilever, with and without attachment of MEMS accelerometers. Computation characterization was performed by application of FEM to study the modal characteristics of the test cantilever. Experimental characterizations, based on using of the non invasive, full-field of view, OEH methodologies, were performed to determine the modes of vibrations of the cantilever with and without attachment of MEMS accelerometers. The results indicated that MEMS accelerometers introduce minimum, yet measurable, effects on the dynamic characteristics of the cantilever, which verify their applicability to modal analysis.

The digital wireless system and the MEMS accelerometers were utilized to perform high-resolution tilt and rotation measurements. The system was calibrated upon the actual driving electronics for the accelerometer. Since the system was developed based on a microcontroller, the computer source code was developed to interface the digital output signals of the MEMS accelerometers with the microcontroller and the RF components. The calibrated results indicated that the sensitivity of the x and the y axis of the accelerometer were 13.163 %/g and 12.324 %/g, respectively. The ratio of the duty cycle outputs at 0 g was determined as 52.3 % for the x -axis and 49.6 % for the y -axis. In addition, the angular resolution of the wireless microcontroller system, based on the dual-axes MEMS accelerometer, was determined to be 1.8 mrad, or 0.103°.

Additional results presented include application of the MEMS gyroscope and the microcontroller to perform angular rate measurements. Since the MEMS gyroscope only provides analog output signals, an 8-bit analog-to-digital conversion circuit was built. The corresponding source code was developed to perform analog-to-digital conversions in two decimal places accuracy. By using the microcontroller system, preliminary rate measurements were performed. These results indicate the feasibility of performing wireless angular rate measurements.

For future works, this thesis research could be further extended by the following list of tasks:

- (1) determination of the fundamental natural frequency of the ADXL202 accelerometer by using different computational packages and further experimental analysis,

- (2) characterize and compare different types of MEMS inertial sensors to determine which one is best suited for modal analysis,
- (3) miniaturization of the developed wireless systems and design of compact packages for the transmitter unit,
- (4) utilization of multiple wireless MEMS inertial sensors to perform modal analysis and health monitoring of real life, complex structures,
- (5) develop a high resolution analog-to-digital conversion circuit to perform high accuracy wireless angular rate measurements.

The above tasks aim to design and apply miniaturized wireless MEMS inertial systems for dynamic analysis of structures. Such wireless systems could be utilized in educational, experimental, civil, and industrial environments.

7. REFERENCES

- J. J. Allen and M. W. Jenkins, 2003, "Short course: The challenges of microelectromechanical (MEMS) technology," *4th International Symp. on MEMS and nanotechnology (4th-ISMAN)*, Charlotte, NC.
- Analog Devices, Inc., 2004, *MEMS and sensors*, <http://www.analog.com/en/cat/0,2878,764,00.html>, Norwood, MA.
- P. Avitabile, 2001, "Experimental modal analysis - A simple non-mathematical presentation," in *Sound and Vibration*.
- H. Anton, 1995, *Calculus with analytic geometry*, 5th ed., Wiley, New York, NY.
- Analog Devices, 2001, Application Note, "ADXL202 / ADXL210 - low cost ± 2 g / ± 10 g dual axis iMEMS® accelerometers with digital output," Analog Devices, Inc., Norwood, MA.
- Analog Devices, 2003a, Application Note, "New iMEMS angular rate sensing gyroscope," Analog Devices, Inc., Norwood, MA.
- Analog Devices, 2003b, Application Note, " $\pm 150^\circ$ /s single chip yaw rate gyro with signal conditioning," Analog Devices, Inc., Norwood, MA.
- Analog Devices, 2003c, Application Note, " $\pm 150^\circ$ /s single chip yaw rate gyro evaluation board," Analog Devices, Inc., Norwood, MA.
- H. van der Auweraer, 2001, "Structural dynamics modeling using modal analysis: applications, trends and challenges," *IEEE Instrumentation and Measurement Technology Conference*, Hungary.
- P. Bergstrom and G. Li, 2001, *Inertial Sensors*, published in M. Gad-el-Hak, *The MEMS Handbook*, CRC Press, Boca Raton, FL.
- J. Bernstein, 2003, "An overview of MEMS inertial sensing technology," in *SENSORS*, Advanstar Communications Inc., Cleveland, OH.
- R. Bitter, T. Mohiuddin, and M. Nawrocki, 2000, *LabVIEW advanced programming technique*, CRC Press, New York, NY.
- Caveo Technology, 2002, *Caveo anti-theft PC card*, <http://www.caveo.com/products/anti-theft.htm>, Newton, MA.

- H. Chung, T. Enomoto, M. Shinozuka, 2003, "MEMS-type accelerometers and wireless communication for structural monitoring," *Proc. Second MIT Conferences on Fluid and Solid Mechanics*, Cambridge, MA.
- T. Costlow, 2004, "Sensing Significant Growth," in *Automotive Engineering International*, SAE International, Brimfield.
- R. Dao, J. Pyle and S. Chaturvedi, 2002, "MEMS: A small technology with a huge impact on consumer electronics," in *Electronic Component News*, New York, NY.
- M. Elwenspoek and R. Wiegerink, 2001, *Mechanical microsensors*, Springer-Verlag, Berlin, Heidelberg.
- EME Systems, 2001, *Stamp II math note*, Berkeley, CA, 2001.
- C. Furlong, 1999, *Hybrid, experimental and computational, approach for the efficient study and optimization of mechanical and electro-mechanical components*, Ph.D. Dissertation, Worcester Polytechnic Institute, Worcester, MA.
- C. Furlong and R. J. Pryputniewicz, 1995a, "New opto-mechanical approach to quantitative characterization of fatigue behavior of dynamically loaded structures," *Proc. SPIE*, 2544:45-56.
- C. Furlong and R. J. Pryputniewicz, 1995b, "Opto-mechanical study and optimization of a cantilever plate dynamics," *Proc. SPIE*, 2545:45-56.
- C. Furlong and R. J. Pryputniewicz, 1998, "Electro-optic holography method for determination of surface shape and deformation," *Proc. SPIE*, 3478:86-97.
- C. Furlong and R. J. Pryputniewicz, 2002, "Characterization of shape and deformation of MEMS by quantitative optoelectronic metrology techniques," *Proc. SPIE*, 4778:1-10.
- M. Gad-el-Hak, 2001, *The MEMS Handbook*, CRC Press, Boca Raton, FL.
- J. Geen and D. Krakauer, 2003, "New iMEMS® Angular-Rate-Sensing Gyroscope," in *Analog Dialogue*, Analog Devices Inc., Norwood, MA.
- M. Hashimoto, 1999, "A 3-Axis Silicon Piezoresistive Accelerometer, Sensors," in *SENSORS*, Advanstar Communications Inc., Cleveland, OH, February 1999.
- R. C. Hibbeler, 1997, *Mechanics of materials*, Prentice-Hall, Upper Saddle River, NJ.
- T.-R. Hsu, 2002, *MEMS & microsystems: design and manufacture*, McGraw-Hill, New York, NY.

- C. Jeong, S. Seok, B. Lee, H. Kim, and K. Chun, 2004, "A study on resonant frequency and Q factor tunings for MEMS vibratory gyroscopes," in *Journal of Micromechanics and Microengineering*.
- H. Johari, 2003, *Development of MEMS Sensors for Measurements of Pressure, Relative Humidity, and Temperature*, M.S. Thesis, Worcester Polytechnic Institute, Worcester, MA.
- C. D. Johnson, 1997, *Process Control Instrumentation Technology*, Prentice-Hall, Upper Saddle River, NJ.
- A. Khazan, 1994, *Transducers and their elements*, Prentice-Hall, Upper Saddle River, NJ.
- R. Kok, C. Furlong, and R. J. Pryputniewicz, 2003a, "Experimental modal analysis using MEMS accelerometers," *Proc. 30th Annual Symp. and Exhibition of IMAPS-NE*, Boxboro, MA, pp.116-123.
- R. Kok, C. Furlong, and R. J. Pryputniewicz, 2003b, "Application of MEMS accelerometers for modal analysis," *Proc. 4th International Symp. on MEMS and nanotechnology (4th-ISMN)*, Charlotte, NC, pp.71-78.
- R. Kok, C. Furlong, and R. J. Pryputniewicz, 2003c, "Development of a wireless MEMS inertial system for health monitoring of structures," *Proc. MRS 2003*, Boston, MA.
- R. Kok, C. Furlong, and R. J. Pryputniewicz, 2004a, "Development of a wireless MEMS inertial system for measurements of rotations," *Proc. 31st Annual Symp. and Exhibition of IMAPS-NE*, Boxboro, MA, pp.50-56.
- R. Kok, C. Furlong, and R. J. Pryputniewicz, 2004b, "Modal testing with wireless MEMS inertial sensors," *Proc. SEM X International Congress & Exposition on Experimental & Applied Mechanics*, Costa Mesa, CA.
- R. Kok, C. Furlong, and R. J. Pryputniewicz, 2004c, "Health monitoring of structures with wireless MEMS inertial systems," *Proc. SEM 15th International Invitational UACEM Symposium*, Springfield, MA, pp.252-260.
- V. A. Kottapalli, A. S. Kiremidjian, J. P. Lynch, E. Carryer, T. W. Kenny, K. H. Law, and Y. Lei, 2003, "Two-tiered wireless sensor network architecture for structural health monitoring," *Proc. SPIE 10th Annual International Symp. on Smart Structures and Materials*, San Diego, CA.
- G. Kulwanoski and J. Schnellinger, 2004, "The principles of piezoelectric accelerometer," in *SENSOR*, Advanstar Communications Inc., Cleveland, OH.

- G. T. A. Kovacs, 1998, *Micromachined transducers sourcebook*, McGraw-Hill, New York, NY.
- T. Kreis, 1996, *Holographic interferometry: Principles and Methods*, Akademie Verlag, Berlin.
- L-3 Communications Corporation, 2004, <http://www.l-3com.com>, New York, NY.
- LINX Technologies, Inc., 1999a, *HP Series-II Transmitter module design guide*, Grant Pass, OR.
- LINX Technologies, Inc., 1999b, *HP Series-II Receiver module design guide*, Grant Pass, OR.
- LINX Technologies, Inc., 2001, *Master development system user's guide*, Grant Pass, OR.
- LINX Technologies, Inc., 2003, *HP2-series*, http://www.linxtechnologies.com/interface.php?section=products&category=rf_modules&subcategory=hp-2_series, Grant Pass, OR.
- A. Lindsay, 2003a, *What's a microcontroller*, Parallax, Inc., Rocklin, CA.
- A. Lindsay, 2003b, *BASIC stamp programming manual*, Parallax, Inc., Rocklin, CA.
- A. Lindsay, 2003c *Basic analog and digital*, Parallax, Inc., Rocklin, CA.
- J. P. Lynch, 2004, "Overview of wireless sensors for real-time health monitoring of civil structures," *Proc. 4th International Workshop on Structural Control and Monitoring*, New York City, NY.
- J. P. Lynch, K. H. Law, E. G. Straser, A. S. Kiremidjian, and T. W. Kenny, 2000, "The development of a wireless modular health monitoring system for civil structures," *Proc. MCEER Mitigation of Earthquake Disaster by Advanced Technologies (MEDAT-2) Workshop*, Las Vegas, NV.
- S. E. Lyshevski, 2000, *Nano- and micro-electromechanical systems: Fundamentals of nano- and microengineering*, CRC Press, Boca Raton, FL.
- M. Madou, 1997, *Fundamentals of microfabrication*, CRC Press, Boca Raton, FL.
- MEMSIC, Inc, 2002, *Dual Axis Sensor Products*, <http://www.memsic.com/memsic/products/productinfo.html>, North Andover, MA.
- National Instruments, Inc., 1999a, *6052E user's manual*, Austin, TX.

- National Instruments, Inc., 1999b, *Data acquisition basic manual*, Austin, TX.
- National Instruments, Inc., 2000, *SCXI-1530/1531 user's menu*, Austin, TX.
- National Instruments, Inc., 2003a, Multifunction Data Acquisition (DAQ), <http://sine.ni.com/apps/we/nioc.vp?cid=1037&lang=US>, <http://www.ni.com>, Austin, TX.
- National Instruments, Inc., 2003b, *SCXI chassis*, Austin, TX.
- National Semiconductor, 2002, Application Note, "ADC0831/ADC0832/ADC0834/ADC0838 8-Bit Serial I/O A/D Converters with Multiplexer Options", National Semiconductor, Santa Clara, CA.
- Newport, 2004a, *SR50 series compact high-resolution rotation stages*, Irvine, CA.
- Newport, 2004b, *UNIDRIV6000 Universal motor driver for ESP6000*, Irvine, CA.
- P. V. O'Neil, 1991, *Advanced engineering mathematics*, 3rd ed., Wadsworth, Inc., Belmont, CA.
- Parallax, Inc., 2004, <http://www.parallax.com>, Rocklin, CA.
- Parallax, 2003a, "BASIC Stamp homework board," Parallax, Inc., Rocklin, CA.
- Parallax, 2003b, "433 MHz RF module," Parallax, Inc., Rocklin, CA, 2003e.
- M. Paz, 1991, *Structural dynamics: theory and computation*, Van Nostrand Reinhold, New York, NY.
- Polytec PI, 1994, *Vibrometer operator's manual for OSF-3000/OFV-502*, Auburn, MA.
- Pro/Engineer, 2001, *User's guide v. 2001*, Parametric Technology Corporation, Waltham, MA.
- R. J. Pryputniewicz, 1993a, "Electronic shearography and electronic holography working side by side," *Proc. SPIE*, 1821:27-37.
- R. J. Pryputniewicz, 1993b, *Engineering experimentation*, Worcester Polytechnic Institute, Worcester, MA.
- R. J. Pryputniewicz, *Holographic numerical analysis*, Worcester Polytechnic Institute, Worcester, MA, 2003.

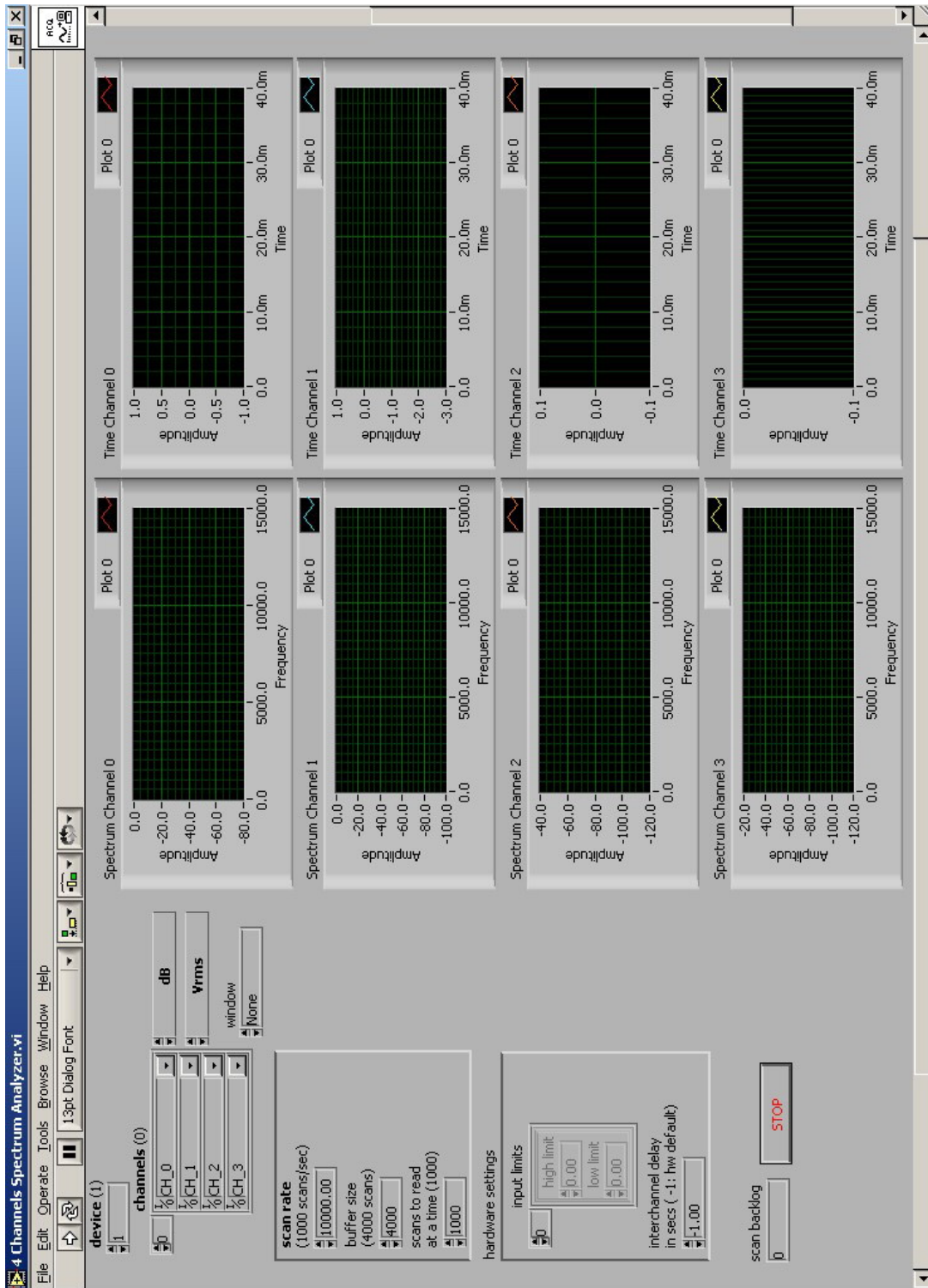
- R. J. Pryputniewicz and K. A. Stetson, 1989, "Measurement of vibration patterns using electro-optic holography," *Proc. SPIE*, 1162:456-467.
- S. S. Rao, 1995, *Mechanical vibrations*, 3rd ed., Addison-Wesley, New York, NY.
- B. J. Schwarz and M. H. Richardson, 1999, "Experimental modal analysis," in *CSI Reliability Week*, Orlando, FL.
- Segway LLC, 2004, <http://www.segway.com>, Bedford, NH.
- SelmaWare Solutions, 2003, www.selmaware.com, Carbondale, IL.
- R. Shear, 1999, "Piezoelectric sensors for OEM applications," in *SENSOR*, Advanstar Communications Inc., Cleveland, OH.
- StampPlot Pro, 2003, *StampPlot Help*, SelmaWare Solutions, Carbondale, IL.
- N. A. Tanner, J. R. Wait, C. R. Farrar, and H. Sohn, 2003, "Structural health monitoring using modular wireless sensors," in *Journal of Intelligent Material Systems and Structures*.
- K. A. Stetson and W. R. Brohinsky, 1985, "Electrooptic holography and its application to hologram interferometry," *Appl. Opt.*, 24(21):3631-3637.
- K. A. Stetson and W. R. Brohinsky, 1987, "Electro-optic holography system for vibration analysis and nondestructive testing," *Opt. Eng.*, 26(12):1234-1239.
- K. A. Stetson and W. R. Brohinsky, 1988, "Fringe-shifting technique for numerical analysis of time-average holograms of vibrating objects," *J. Opt. Soc. Am. A*, 5(9):1472-1476.
- K. A. Stetson, W. R. Brohinsky, J. Wahid, and T. Bushman, 1989, "An electro-optic holography system with real-time arithmetic processing," *J. Nondest. Eval.*, 8(2):69-76.
- W. T. Thomson and M. D. Dahleh, 1998, *Theory of vibration with applications*, 5th ed., Prentice Hall, Upper Saddle River, NJ.
- R. Toogood, 1998, *Pro/Engineer tutorial – Release 20*, SDC Publications, Mission, KS.
- R. Toogood, 2000, *Pro/Mechanical tutorial structure (Release 2000i² - Integrated Mode)*, SDC Publications, Mission, KS.
- E. Volterra and E. C. Zachmanoglou, 1965, *Dynamics of vibrations*, Chalres E. Merrill Books, Inc., Columbus, OH.

H. Weinberg, 2002, "Using the ADXL202 in pedometer and personal navigation applications," in *Analog Devices, Application Note AN-602*, Norwood, MA.

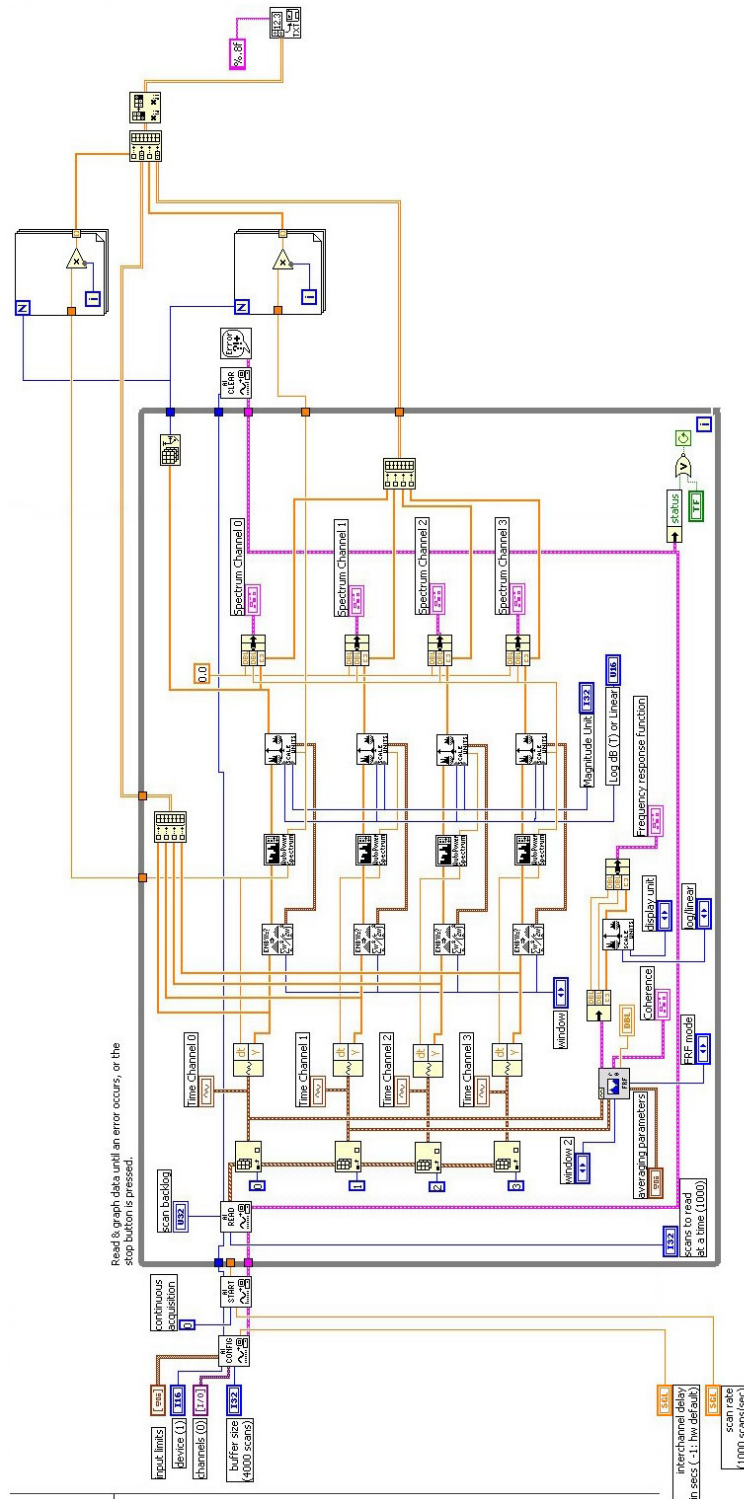
WPI, 2002, Class notes, ME 593M - MEMS and Micromechatronics, WPI-ME/CHSLT, Worcester, MA.

N. Yazdi, F. Ayazi, and K. Najafi, 1998, "Micromachined inertial sensors," *Proc. of the IEEE, Vol. 86, No. 8*, pp.1640-1659.

APPENDIX A. Front panel of the developed LabVIEW VI for a four channels spectrum analyzer



APPENDIX B. Block diagram of the developed LabVIEW VI for a four channels spectrum analyzer



APPENDIX C. Source codes of the microcontroller with a wireless transmitter

```
' {$STAMP BS2}
' {$PBASIC 2.5}

'-----
' I/O Definitions
'-----

Xin          PIN  8          ' X input from ADXL202
Yin          PIN  9          ' Y input from ADXL202

'-----
' Constants
'-----

HiPulse      CON  1          ' measure high-going pulse
LoPulse      CON  0

DegSym       CON  176       ' degrees symbol

'-----
' Variables
'-----

xRaw         VAR  Byte      ' pulse from ADXL202(x-axis)
xmG          VAR  Word      ' g force (1000ths)
xTilt        VAR  Byte      ' tilt angle

yRaw         VAR  Byte      ' pulse from ADXL202(y-axis)
ymG          VAR  Word
yTilt        VAR  Byte

disp         VAR  Byte      ' displacement (0.0 - 0.99)
angle        VAR  Byte      ' tilt angle

xRawH        VAR  Word      ' high pulse from ADXL202 (x-axis)
xRawL        VAR  Word      ' low pulse from ADXL202 (y-axis)
yRawH        VAR  Word      ' high pulse from ADXL202 (x-axis)
yRawL        VAR  Word      ' low pulse from ADXL202 (y-axis)
T2x          VAR  Word      ' period of x-axis
T2y          VAR  Word      ' period of y-axis
xRawscale    VAR  Byte      ' scaled high pulse from ADXL202 (x-axis)
yRawscale    VAR  Byte      ' scaled high pulse from ADXL202 (y-axis)
T2scale      VAR  Byte      ' scaled period of the signal
```

```

'-----
' Initialization
'-----

Setup:
PAUSE 250                                ' let DEBUG window open
DEBUG "Analog Devices ADXL202 Accelerometer", CR
DEBUG "-----"

'-----
' Program Code
'-----

Main:
DO
  GOSUB Read_Tilt                          ' reads G-force and Tilt

  DEBUG CR$RXY, 0, 3                       ' measurements of x-axis
  DEBUG "X Input... ",
    DEC (xRaw / 500), ".", DEC3 xRaw, " ms",
    CLREOL, CR,
    "G Force... ", (xmG.BIT15 * 13 + " "),
    DEC (ABS xmG / 1000), ".", DEC3 (ABS xmG), " g",
    CLREOL, CR,
    "X Tilt... ", (xTilt * 13 + " "),
    DEC ABS xTilt, DegSym, CLREOL

  DEBUG CR$RXY, 0, 7                       ' measurements of y-axis
  DEBUG "Y Input... ",
    DEC (yRaw / 500), ".", DEC3 yRaw, " ms",
    CLREOL, CR,
    "G Force... ", (ymG.BIT15 * 13 + " "),
    DEC (ABS ymG / 1000), ".", DEC3 (ABS ymG), " g",
    CLREOL, CR,
    "Y Tilt... ", (yTilt * 13 + " "),
    DEC ABS yTilt, DegSym, CLREOL, CR, CR

  xRawscale = xRawH / 20
  yRawscale = yRawH / 20
  T2scale = ((T2x + T2y)/2) / 20
  DEBUG DEC xRawH, ",", DEC xRawscale, ",", DEC yRawH, ",", DEC yRawscale, ",",
    DEC (T2x + T2y)/2, ",", DEC T2scale, CR

  SEROUT 13,16468,[xRawscale]              ' send scaled pulse to transmitter
  PAUSE 20                                 ' pause 8 milli-second
  SEROUT 13,16468,[yRawscale]              ' send scaled pulse to transmitter
  PAUSE 20                                 ' pause 8 milli-second
  SEROUT 13,16468,[T2scale]                ' send period to transmitter
  PAUSE 20                                 ' pause 8 milli-second

LOOP
END

```

' Subroutines

Read_G_Force:

```

PULSIN Xin, HiPulse, xRawH      ' read pulse output
PULSIN Xin, LoPulse, xRawL      ' read pulse output
T2x = xRawH + xRawL             ' signal period
xmG = ((xRawH / T2x) - 500) * 8  ' convert to 1/1000 g

```

```

PULSIN yin, HiPulse, yRawH
PULSIN yin, LoPulse, yRawL
T2y = yRawH + yRawL
ymG = ((yRawH / T2y) - 500) * 8
RETURN

```

Read_Tilt:

GOSUB Read_G_Force

```

disp = ABS xmG / 10 MAX 100      ' x displacement
GOSUB Arcsine
xTilt = angle * (-2 * xmG.BIT15 + 1) ' fix sign
disp = ABS ymG / 10 MAX 100      ' y displacement
GOSUB Arcsine
yTilt = angle * (-2 * ymG.BIT15 + 1) ' fix sign
RETURN

```

Arccosine:

```

disp = disp * / 983 / 3          ' normalize input to 127
angle = 63 - (disp / 2)          ' approximate angle
DO                                ' find angle
  IF (COS angle <= disp) THEN EXIT
  angle = angle + 1
LOOP
angle = angle * / 360            ' convert brads to degrees
RETURN

```

Arcsine:

```

GOSUB Arccosine
angle = 90 - angle
RETURN

```

APPENDIX D. Source codes of the microcontroller with a wireless receiver

```
' {$STAMP BS2}
' {$PBASIC 2.5}

'-----
' Constants
'-----

DegSym      CON    176          ' degrees symbol

'-----
' Variables
'-----

xRawH      VAR    Word        ' high pulse from ADXL202 (x-axis)
xRawL      VAR    Word        ' low pulse from ADXL202 (y-axis)
yRawH      VAR    Word        ' high pulse from ADXL202 (x-axis)
yRawL      VAR    Word        ' low pulse from ADXL202 (y-axis)
T2         VAR    Word        ' signal period
xRawscale  VAR    Byte        ' scaled high pulse from ADXL202 (x-axis)
yRawscale  VAR    Byte        ' scaled high pulse from ADXL202 (y-axis)
T2scale    VAR    Byte        ' scaled period of the signal

'-----
' Initialization
'-----

Setup:
PAUSE 250          ' let DEBUG window open
DEBUG "Wireless data from ADXL202 Accelerometer", CR
DEBUG "-----"

'-----
' Program Code
'-----

start:

SERIN 4,16624,[xRawscale]
PAUSE 15
SERIN 4,16624,[yRawscale]
PAUSE 15
SERIN 4,16624,[T2scale]
PAUSE 15

xRawH = xRawscale * 20
yRawH = yRawscale * 20
T2 = T2scale * 20
DEBUG DEC xRawH, ",", DEC yRawH, ",", DEC T2, CR
```

APPENDIX E. Source code of the analog-to-digital conversion circuit

```
' {$STAMP BS2}
' {$PBASIC 2.5}

adcBits    VAR  Byte
v          VAR  Byte
r          VAR  Byte
v2         VAR  Byte
v3         VAR  Byte

CS         PIN  0
CLK        PIN  1
DataOutput PIN  2

DO
  GOSUB ADC_DATA
  GOSUB Calc_Volts
  GOSUB Display
LOOP

ADC_Data:
  HIGH CS
  LOW CS
  LOW CLK
  PULSOUT CLK, 210
  SHIF TIN DataOutput, CLK, MSBPOST, [adcBits \8]
RETURN

Calc_Volts:
  v = 5 * adcBits / 255
  r = 5 * adcBits // 255
  v2 = 100 * r / 255
  v3 = 100 * r // 255
  IF (v3 >= 5) THEN v2 = v2 + 1
  IF (v2 >= 100) THEN
    v = v + 1
    v2 = 0
  ENDIF
RETURN

Display:
  DEBUG HOME
  DEBUG "8-bit binary value: ", BIN8 adcBits
  DEBUG CR, CR, "Decimal value: ", DEC3 adcBits
  DEBUG CR, CR, "DVM Reading: "
  DEBUG DEC1 v, ".", DEC2 v2, " Volts", CR, CR

  DEBUG DEC1 v, ".", DEC2 v2, CR

RETURN
```